SYNTHESIS AND CHARACTERIZATION OF NOVEL ELECTRODE MATERIALS FOR HIGH-PERFORMANCE SUPERCAPACITORS

WANG MAN

PhD

The Hong Kong Polytechnic University

This programme is jointly offered by The Hong Kong Polytechnic University and Xi'an Jiaotong University

2023

The Hong Kong Polytechnic University

Department of Mechanical Engineering

Xi'an Jiaotong University

School of Chemical Engineering and Technology

Synthesis and Characterization of Novel Electrode Materials for High-Performance Supercapacitors

Wang Man

A thesis submitted in partial fulfillment of the requirements for the degree of Doctor of Philosophy

August 2022

CERTIFICATE OF ORIGINALITY

I hereby declare that this thesis is my own work and that, to the best of my knowledge and belief, it reproduces no material previously published or written, nor material that has been accepted for the award of any other degree or diploma, except where due acknowledgement has been made in the text.

Wang Man

ABSTRACT

Supercapacitors (SCs), as emerging advanced high-efficiency energy-storage devices, have been extensively investigated in recent years because of their high rate capability and excellent cycling stability. However, the unsatisfactory energy density ($E<10$ Wh kg^{-1}) of SCs severely hinders their further applications. The optimization of composition and structure of electrode materials to match with various electrolytes has been regarded as an effective strategy to enhance the overall electrochemical performance of SCs. Among them, carbon-based electrode materials stand out by virtue ·of their excellent chemical and physical characteristics including large specific surface area, high electrical conductivity and excellent structural stability, and are potentially suitable for different kinds of aqueous/organic electrolytes. In the present study, three kinds of carbon-based electrode materials are designed and fabricated for SCs with increased energy density by using various electrolytes.

First of all, two-dimensional nitrogen-doped porous carbon nanosheets (denoted as NC-*x* with *x* being the carbonization temperature in Degree Celsius) were systematically synthesized by using general dual-crystals templating assisted strategy with pore structure and surface composition optimized. Employed as both positive and negative electrodes, the as-prepared NC-900 delivered an energy density of 22.4 Wh kg^{-1} with a working voltage up to 1.6 V and a capacitance retention of 95% after 30,000 cycles using redox electrolyte (2 M Na_2SO_4 and 0.05 M KI). The experimental and theoretical analyses reveal the contributions of nitrogen configurations on the carbon scaffolds to accelerate the redox chemistry of I^-/I_3^-. The enhanced redox performance of the porous carbon nanosheets is linearly proportional to the graphitic N content, which is consistent with the enlarged electron-donating area and the strong adsorption capacity towards iodine species (-0.69 eV for I* and -0.73 eV for I_2) at the graphitic N sites.

Then, nickel cobalt layer double hydroxide (NiCoLDH) was deposited onto carbon fiber through the electrodeposition process, followed by the introduction of poly(3,4-ethylenedioxythiophene) (PEDOT) skin onto the surface of NiCoLDH via oxidative chemical vapor deposition technique. By analyzing multiple experimental results and conducting COMSOL multiphysics simulation, it was found that such ionically permeable and electronically conductive PEDOT skin with optimized

thickness can facilitate the electrons transportation along the interface, inducing uniformly distributed potential and optimizing pathway of ions to active sites. Further DFT theoretical analysis indicated the presence of PEDOT layer can build an embedded electric field and induce lower desorption energy of hydrogen for electrochemical redox reaction. Thus, the resulting electrode material exhibited an improved rate capability from 55% to 79% and an enhanced cycling stability from 70% to 92% after 6000 cycles. As a proof-of-concept application, a supercapacitor was made of 10nm PEDOT coated LDH as positive electrode and activated carbon as negative electrode, LDH/PEDOT-*10*//AC. It can deliver a high energy density up to 58 Wh kg^{-1} with a working voltage of 1.6 V in 6 M KOH electrolyte. Besides, 80% capacitance retention can be achieved after 6,000 cycles.

Finally, boron-doped porous carbon nanosheet (BPCN) was prepared through a simple one-step calcination method. Experimental results and density functional theory simulations revealed that not only the sufficient porous structure (89% mesopore volume) can provide the efficient pathway for sodium-ions, *p*-type boron doping into the carbon matrix can also generate strong adsorption energy (-2.3 eV) toward sodium-ions, leading to double capacitive contribution in slope region compared to the undoped carbon material. As a result, the BPCN electrode delivered a high capacity of 357 mAh g^{-1} and 164 mAh g^{-1} at 0.1 A g^{-1} and 10 A g^{-1}, respectively. Additionally, the as-assembled sodium ion capacitors with a working voltage as high as 4 V exhibited a maximum energy density 64.8 Wh kg^{-1} and maintained 80% capacity after 1,500 cycles at 1.0 A g^{-1}.

List of Publications Out of This Thesis

M. Wang, Q. Liu, K. Jiang, S. Liu, J. Yang*, J. Qiu, G. Chen*, Ionically permeable polymer skin on nickel-cobalt hydroxide nanosheets enhances rate and cycling performance for aqueous hybrid supercapacitor, Under preparation.

M. Wang, J. Yang*, S. Liu, J. Qiu*, G. Chen*, Enhanced reversible sloping capacity enabled by boron-doped sites in porous carbon nanosheet for high-performance sodium ion capacitors, Under preparation.

M. Wang, J. Yang*, S. Liu, X. Che, S. He, G. Chen*, J. Qiu*, Nitrogen-doped porous carbon electrode for aqueous iodide redox supercapacitor, Chemical Engineering Journal, 451, 2023, 138501.

M. Wang, J. Yang*, S. Liu, C. Hu, J. Qiu*, Dual hybrid effect endowing nickel–cobalt sulfides with enhanced cycling stability for asymmetrical supercapacitors, ACS Applied Energy Materials, 3, 2020, 6977-6984.

M. Wang, J. Yang*, K. Jia, S. Liu, C. Hu, J. Qiu*, Boosting supercapacitor performance of graphene by coupling with nitrogen-doped hollow carbon frameworks, Chemistry-A European Journal, 26, 2020, 2897-2903.

M. Wang, J. Yang*, S. Liu, M. Li, C. Hu, J. Qiu*, Nitrogen-doped hierarchically porous carbon nanosheets derived from polymer/graphene oxide hydrogels for high-performance supercapacitors, Journal of Colloid and Interface Science, 560, 2020, 69-76.

M. Wang, J. Yang*, S. Liu, C. Hu, S. Li, J. Qiu*, Polyethyleneimine-mediated fabrication of two-dimensional cobalt sulfide/graphene hybrid nanosheets for high-performance supercapacitors, ACS Applied Materials & Interfaces, 11, 2019, 26235-26242.

Acknowledgements

There are many people I would like to express my appreciation. They have contributed to my work either from scientific support or the friendly study environment. Without these people, I would not be able to complete the joint PhD degree offered by the Hong Kong Polytechnic University and Xi'an Jiaotong University.

During the two years of study at Xi'an Jiaotong University as a PhD student before coming to Hong Kong, Dr. Juan Yang, and Mr. Lijun Gao have helped me a lot by giving me the training on basic experimental skills and designing experiments. They introduced me to various experimental measurements, such as electrochemical station, Raman, XRD, XPS, SEM, and supported me financially and technically. I also want to thank Mr. Siyu Liu for the DFT theoretical calculation results. I thank them for their guidance on my research, as well as all their help in this process.

Fortunately, I was admitted to the Joint PhD Program between the Hong Kong Polytechnic University and Xi'an Jiaotong University. Thus, I have the opportunity to continue my study in Hong Kong. I am very grateful to my chief supervisor, Prof. Guohua Chen, Chair Professor of Energy Conversion and Storage, for his valuable guidance, encouragement, and financial support during my study. He nurtures me for an independent research program with high impact for energy storage. This includes the research objectives to select, research results analysis, report writing and presentation. This is a valuable experience in the early stage of my scientific research.

In addition, I am very grateful to our group members: Mr. Liang Hu, Mr. Yinggang Zhu, Mr. Qingsong Weng, Mr. Binglong Zhao, Ms. Chuyi Xie, Ms. Yutong Liu, Ms. Zeqi Zhou, Dr. Xiaoliang Yu, Dr. Xusong Qin, Dr. Dongmei Lin, Dr. Kai Zhu, Dr. Yang Liu, Dr. Cong Lin, and Dr. Junxiong Wu. They gave me great help and encouragement during my research. I also want to thank Mr. Jiang Kai for electrical field simulation, and Dr. Qiang Liu, who helped me a lot for my PhD research, especially on the use of oCVD equipment he helped built.

Finally, I give my greatest appreciation to my family. They gave me power and encouraged me during my toughest time. Their care and love bring comforts to me during the special epidemic period.

Table of Contents

List of Figures

List of Tables

Chapter 1 Introduction

1.1. The overview of supercapacitors

In recent years, with the continuous development of human society, people's demand for energy has increased significantly. As a highly accessible resource, traditional fossil fuels provide indelible benefits for people's daily life and economic prosperity contribution.[1, 2] As of 2022, the world's total demand for oil alone will reach 99.4 million barrels per day, and this value will reach 104.1 million barrels per day by 2026.[3] The increasingly depleted and non-renewable resources have seriously affected all areas of society. In addition, the resulting serious pollution and destroyed ecological balance on earth have alarmed the society.[4] Therefore, the development of renewable green and clean energy has become the current top priority of research. Until now, the existing clean energy is mainly from hydraulic energy, geothermal energy, solar energy, wind energy and tidal energy.[5] However these types of clean energy have serious discontinuity and instability problems, which are difficult to be directly consumed as they are generated.[6] In order to efficiently use the above energy, it is necessary to convert and store it for convenient consumption at demand.

As to the multiple energy conversion devices mentioned above, the advancement of large mechanical devices, such as waterwheel, photovoltaics, solar water heater and thermoelectric generator, will largely influence the efficiency of energy conversion from other energy sources to electrical energy.[7-10] However, how to store and utilize the converted electrical energy in a suitable way is still a big problem. In this regard, energy storage system, as an intermediate system connecting clean energy and power equipment, has attracted more and more attention from researchers.[11-13] At present, numerous energy storage devices have been developed including compressed air, hydraulic dam, hydrogen storage, lithium/sodium ion batteries, and capacitors.[14-18] Among them, traditional capacitors using metal plates as electrode materials exhibit great characteristics of long-cycle stability and high power density, while batteries can deliver high energy density.

Supercapacitors are a new type of energy storage device between traditional capacitors and batteries as shown in **Figure 1.1**.[19] It has the advantages of fast charge and discharge performance (short discharge time: 1-10 s) and long cycle life (over

10,000 cycles), making it unique and brilliant by using electrode material with more active sites compared to the metal plates of traditional capacitor.[20]

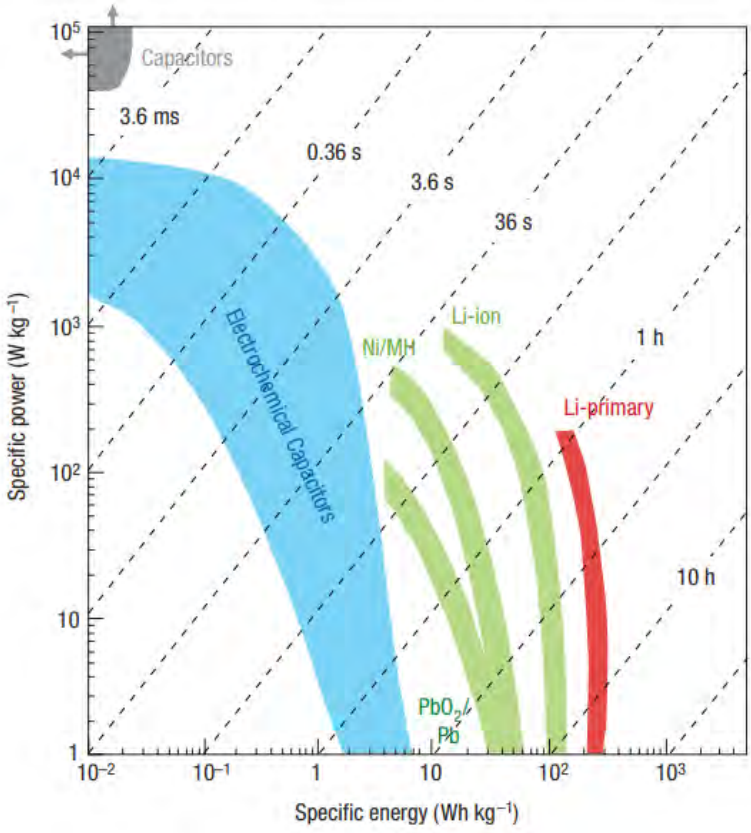

Figure 1.1 The comparison of supercapacitor, traditional capacitor and batteries.[19] (Reproduced with permission from Royal Society of Chemistry)

Further, **Figure 1.2** shows the current status of supercapacitor research in the past 10 years. It can be seen that the research on supercapacitors has been increasing annually. From 2019, the research publications even exceeded 5,000 items per year. Moreover, the investigated electrode materials spread from carbon, metal-organic framework materials (MOFs), metal oxides, and conductive polymers to their composites.[21-23] Despite the ultra-high power density and cycle stability of supercapacitors, their energy density is much lower than that of batteries, which greatly limits its wide application.[24] Therefore, the research and development of supercapacitors with high energy density maintaining high power density and ultra-high cycle stability are particularly important.

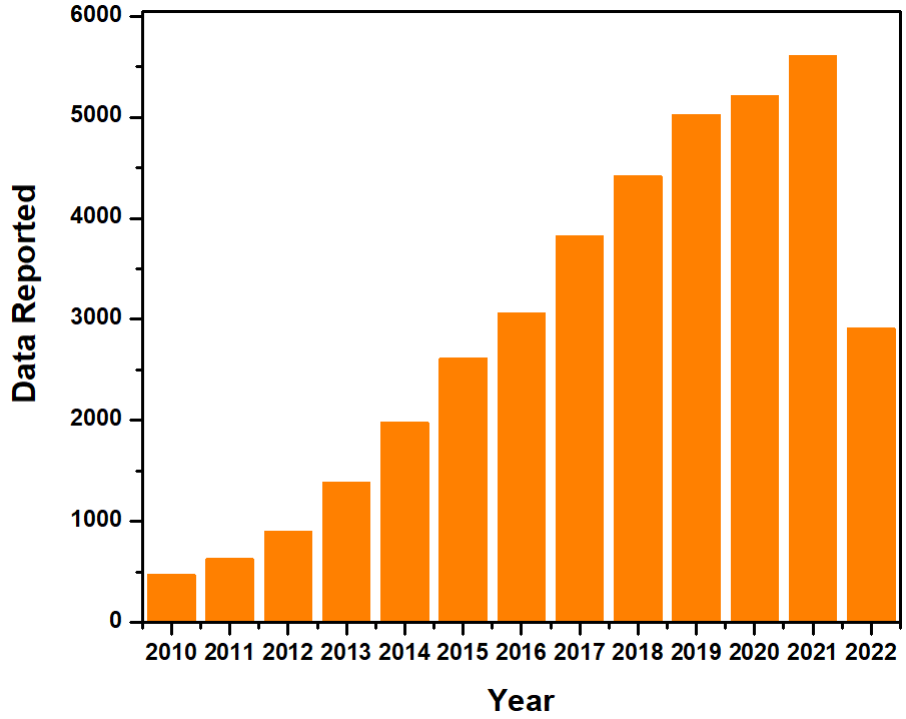

Figure 1.2 The number of supercapacitor research from 2010 to 2022.

1.2. The development of supercapacitors

The research on capacitors can be traced back to the invention of the "Leyden Bottle", which illustrated the charge separation and storage process of the two-electrode plates. It laid the foundation for the energy storage principle of capacitors, as shown in **Figure 1.3**.[11] Subsequently, in 1957, Becker invented the first capacitor with electrodes made of activated carbon and proposed the idea of using miniaturized electrochemical capacitors as energy storage devices.[25] Later on, SOHIO produced a non-aqueous activated carbon supercapacitor with a high operating voltage (3.4-4.0 V), which opened a new era of large-scale commercialization of carbon-based electrochemical capacitors.[26] In 1971, Trasatti *et al.* reported a new type of transition metal compound RuO_2 material, which exhibited excellent capacitance behavior, high Coulomb efficiency and long cycle life, creating the research heap on metal compound electrodes.[27] In 1997, Evans and Miller proposed the concept of hybrid capacitors, which provided a theoretical basis for the assembly of AC//$Li_4Ti_5O_{12}$ hybrid capacitors by Telcordia Technologies in the United States. Their work opened up a new direction for capacitor research.[28] With continuous increase in the demand for high power and high safety energy storage equipment continues to grow, research work on

supercapacitors has also increased significantly.[29] Additionally, benefited from the rapid development of nanotechnology and characterization methods, the energy storage mechanism of supercapacitors has become clearer, greatly promoting the development of such devices.

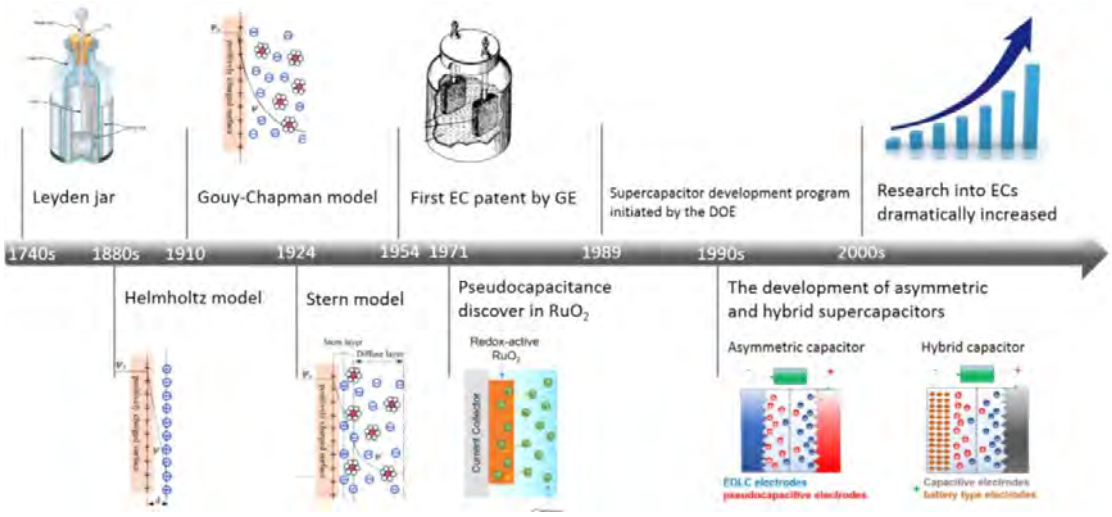

Figure 1.3 The development history of capacitor.[11] (Reproduced with permission from American Chemical Society)

1.3. The configuration of supercapacitors

The traditional capacitor is composed of electrode and dielectric material as shown in **Figure 1.4a**. Various types of supercapacitors (such as electric double-layer capacitor, pseudo capacitor and hybrid capacitor) have been reported. The device mainly includes the following parts: electrode material, current collector, separator and electrolyte (**Figures 1.4b-d**).[20] As one of the most important parts of the supercapacitors, the electrode materials can be divided into following three categories: carbon-based materials, transition metal-based compounds and conductive polymers.[30] Among them, carbon materials are mostly used in electric double layer and hybrid capacitor while transition metal-based compounds and conductive polymers are mostly used in pseudocapacitive capacitor and hybrid capacitor.[31-34] For the current collector, nickel foam, nickel mesh and titanium sheet are most frequently used owing to their high conductivity, high chemical and physical stability and industrialization capability.[31] As to the separator, non-woven fabrics can not only prevent contact

between the two electrodes but also possess high enough porosity to facilitate ions transfer between the two electrodes.[35]

For the electrolyte, it can be divided into water-based inorganic electrolytes (H_2SO_4, KOH or Na_2SO_4), organic electrolytes (solute salts are dissolved in organic solvents) and ionic liquids (IL).[36-39] Various types of electrolytes can not only determine the operating voltage of the supercapacitor, but also cause a non-negligible effect on the rate performance and cycle stability of the supercapacitor owing to their different ionic conductivities. In water-based electrolytes, because of the limitation of water electrolysis (~1.23V), the voltage range of supercapacitors is still relatively low.[40] However, they still perform well in large-scale energy storage applications because of their high power density, low cost and high safety. In non-aqueous electrolytes, the operating voltage is generally between 2.5-2.8 V (organic electrolyte) and 3.5-4.0 V (IL).[41, 42] The enlarged operating voltage of supercapacitors by using IL is conducive to improving the performance of the devices. However, the obvious problems, such as sluggish diffusion kinetics, high viscosity, high cost and severe toxicity for some ILs, greatly restrict the wide application.

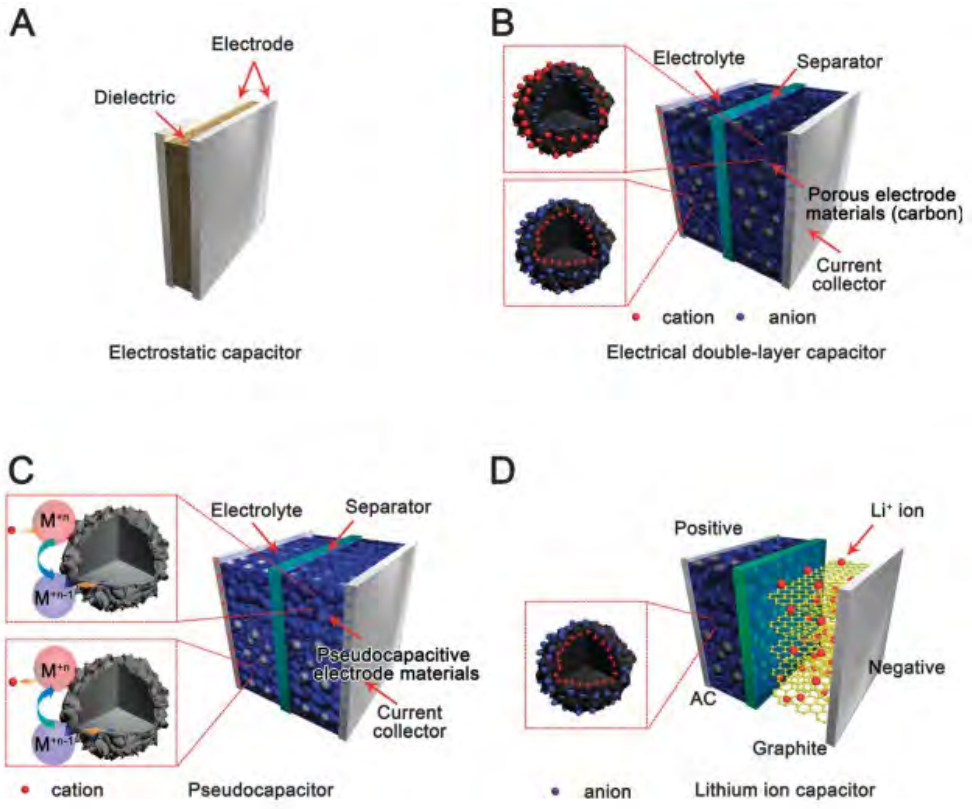

Figure 1.4 Schematic diagram of (a) an electrostatic capacitor, (b) an electric double-layer capacitor, (c) a pseudocapacitor, and (d) a hybrid-capacitor.[20] (Reproduced with permission from Royal Society of Chemistry)

1.4. The advantages of supercapacitors

As an energy storage device between traditional capacitor and battery, supercapacitors have the following advantages: high rate capability, high power density, long cycle life, and environmental friendliness.[31, 43, 44] A comparison of the key indicators of the devices mentioned above are presented in **Table 1.1.** It can be seen that the energy density of supercapacitor is largely enhanced compared to the traditional capacitor, although this value is still much lower than battery. Moreover, supercapacitors retain the advantages of high power density of capacitors, up to 10,000 W kg^{-1}, indicating that they can be used in the devices required high output power density. Besides, the columbic efficiency is another important parameter for energy storage devices. Benefited from the near surface reaction mechanism of supercapacitor, the high columbic efficiency (CE, >99%) can be easily achieved, meaning that fully reversible reaction happens, further achieving high cycling stability. Thus, the goal for supercapacitor is to enhance the energy density while maintain high power density and long cycling stability characteristics.[24]

Table 1.1 The comparison between different energy storage devices.[24]

Characteristic	**Capacitor**	**Supercapacitor**	**Battery**
Specific Energy Density, Wh kg^{-1}	<0.1	1-10	100-500
Specific Power Density, W kg^{-1}	>10,000	>10,000	<1,000
Charging Time	10^{-6}-10^{-3} s	s to mins	several hours
Discharging Time	10^{-6}-10^{-3} s	s to mins	several hours
Columbic Efficiency, %	~100	>99	70-85
Cycling Stability	Nearly Infinite	>5,000	<1,000
Charge Storage Determinants	Specific surface area and Electrolyte	Microstructure of electrode and electrolyte	Thermodynamics and active mass

1.5. Different storage mechanisms of supercapacitors

1.5.1. Electric double layer capacitor

As shown in **Figure 1.5a,** under the applied electric field, the ions in the electrolyte will migrate to the specific electrode in a directional manner, forming a double-layer structure at the electrode/electrolyte interface.[23] After the remove of electric field, the positive and negative ions return to the electrolyte to complete a charge and discharge loop.[11] Electric double-layer capacitors are the simplest commercial capacitors, which can store energy through electrostatic adsorption between the charge and the electrode interface without significant charge transfer. This physical adsorption process enables the charge and discharge process of the electric double layer capacitor to be completed in a very short time (~10^{-8} s), exhibiting ultra-high power density. Even after 10,000 charge and discharge cycles, the electric double layer capacitor still possesses very stable electrochemical performance, which is far superior to a battery. Typically, the electrode materials of electric double layer capacitors are mainly carbon-based materials, including commercial activated carbon, carbon aerogel, carbon nanotubes, carbon nanofibers and graphene, exhibiting obvious advantages of large specific surface area, high conductivity and good electrochemical stability.[45-49] However, the capacity of a pure carbon-based electric double layer capacitor is still low with a value being about 100~300 F g^{-1}. Due to the limited active sites of carbon-based electrode material, the resulting energy density range is 3-10 Wh kg^{-1}, which is also much lower than that of a typical lithium ion battery based on lithium ferrous phosphate/graphite system (>100 Wh kg^{-1}).[50, 51] Therefore, to increase the capacity of carbon-based materials is the goal that many researchers are striving for.

1.5.2. Pseudocapacitor

Compared with electric double layer capacitors, the energy storage mechanism of pseudocapacitor capacitors includes the following two parts: the similar physical absorption/desorption mechanism of the electric double layer capacitance on the surface of the electrode material, and the pseudocapacitive mechanism derived from the rapid and reversible redox process and electron transfer near the electrode surface.[52] The capacitance can be calculated as:

$$C=\frac{\Delta Q}{\Delta U} \quad (1\text{-}1)$$

Where capacitance (C) has a linear relationship with the charge (ΔQ) and the voltage range (ΔU).

Therefore, the storage process of pseudocapacitor is totally different from the insertion/extraction reaction in lithium/sodium-ion batteries. According to various electrochemical reaction processes, different pseudocapacitive mechanisms in pseudocapacitor are shown in **Figures 1.5b-d**.

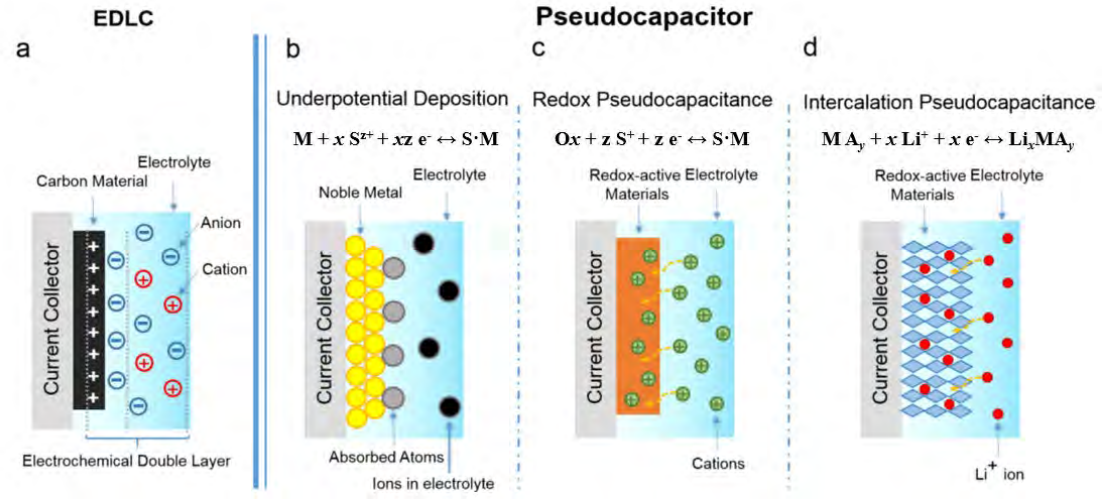

Figure 1.5 Schematics of charge-storage mechanisms for (a) an EDLC and (b–d) different types of pseudocapacitive electrodes: (b) underpotential deposition, (c) redox pseudocapacitor, and (d) ion intercalation pseudocapacitor.[11] (Reproduced with permission from American Chemical Society)

1.5.2.1. Underpotential deposition

Underpotential deposition allows the metal cations in the electrolyte to be electrodeposited at places where the potential is lower than the equilibrium potential, thus realizing the reduction of cations.[53, 54] The whole process is shown in the following reaction (**Figure 1.5b**):

$$M + x\ S^{z+} + xz\ e^- \leftrightarrow S{\cdot}M \quad (1\text{-}2)$$

Where, S is the adsorbed atom, M is the noble metal, x is the number of adsorbed atoms, z is the valence of the adsorbed atoms, and xz is the number of electron transfers. However, the operating voltage range under this reaction is relatively small, only 0.3-0.6 V. Therefore, the energy density of this pseudocapacitor is extremely limited.

1.5.2.2. Redox reaction

The redox pseudocapacitance is based on the redox process between the electrode and ions in the electrolyte through continuously oxidizing and reducing electrode material at various charge and discharge processes. Specifically, metal oxides, sulfides, phosphatides and polymers can be used as potential electrode materials.[55] The reaction process is simplified as follows (**Figure 1.5c**):

$$O_x + z\ S^+ + z\ e^- \leftrightarrow RedS_z \quad (1\text{-}3)$$

Where, O_x represents the oxidized species (e.g., RuO_2) of the electrode material, S is the electrolyte ions adsorbed on the surface, z is the number of electrons transferred in the reaction, and $RedS_z$ represents the reduced species (e.g., $RuO_{2-z}(OH)_z$) of the electrode material. By utilizing different reactive ions and the electrode materials, the specific capacitance of this type of pseudocapacitor can be as high as about 1,000 F g^{-1}, which is 4-10 times of the EDLC-type electrode material.

1.5.2.3. Ion deintercalation reaction

This type of pseudocapacitance capacitor uses the intercalation and deintercalation reactions of electrolyte ions to transport through the layered crystal material such as molybdenum disulfide (MoS_2) and titanium disulfide (TiS_2) in the aqueous solution for charge storage.[56, 57] The reaction below takes lithium ion based electrolyte as a demo (**Figure 1.5d**):

$$MA_y + x\ Li^+ + x\ e^- \leftrightarrow Li_xMA_y \quad (1\text{-}4)$$

Where, MA_y is an embedded material, and x is the number of charge transfer. When electrolyte ions are inserted into the active electrode material, the valence of the active electrode material changes. This cation-embedded pseudocapacitor is a transitional behavior between the battery and the capacitor. This type of material combines both high energy density of battery and high-power density of capacitor, gradually becoming a hot research area.

1.5.3. Hybrid capacitor

Hybrid supercapacitors, also known as metal ion supercapacitors, include a high-energy battery-type negative electrode and a supercapacitor-type positive electrode. The electrolyte is an organic electrolyte containing metal ion salts. The energy storage mechanism is briefly illustrated as seen in **Figure 1.6**.[58] During the charging process, the anions move to the positive electrode, adsorb to the surface of the positive electrode to achieve a capacitive reaction, while cations migrate to the negative electrode, adsorb to the surface of the negative electrode to conduct a battery-type reaction. The discharge process is opposite to the charging process. It should be noted that the introduction of battery-type reactions shows much potential on overcoming the low energy density of supercapacitors, while maintaining the excellent rate and cycling performance.

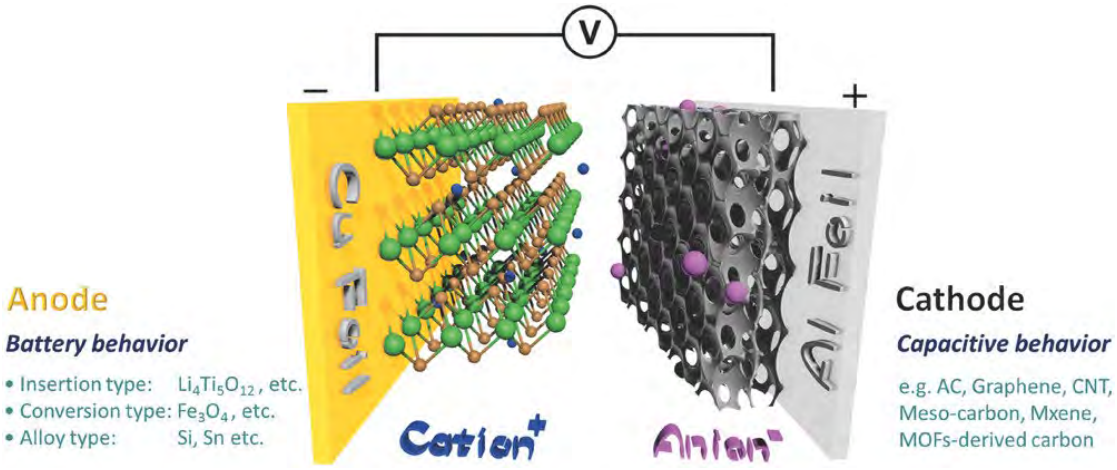

Figure 1.6 Typical cell structure and electrode materials of a metal-ion capacitor.[58] (Reproduced with permission from John Wiley and Sons and Copyright Clearance Center)

In summary, compared with different energy storage devices, supercapacitors successfully combine the advantages of secondary batteries and traditional capacitors, showing satisfactory energy density and high power density output, as shown in **Figure 1.7**.[59] However, there is still a gap of energy density between battery and supercapacitor, derived from the differences of both electrolyte and electrode material used. Thus, how to increase the energy density while maintaining the power density of supercapacitor is a great challenge. To meet this challenge, one is to optimize the structure and composition of electrode material and match them with the appropriate electrolyte. The other one is to develop hybrid energy storage device (HESD)

combining the energy storage behavior of both supercapacitors and secondary batteries, which presents multifold advantages such as high energy density, high power density and long cycle stability.

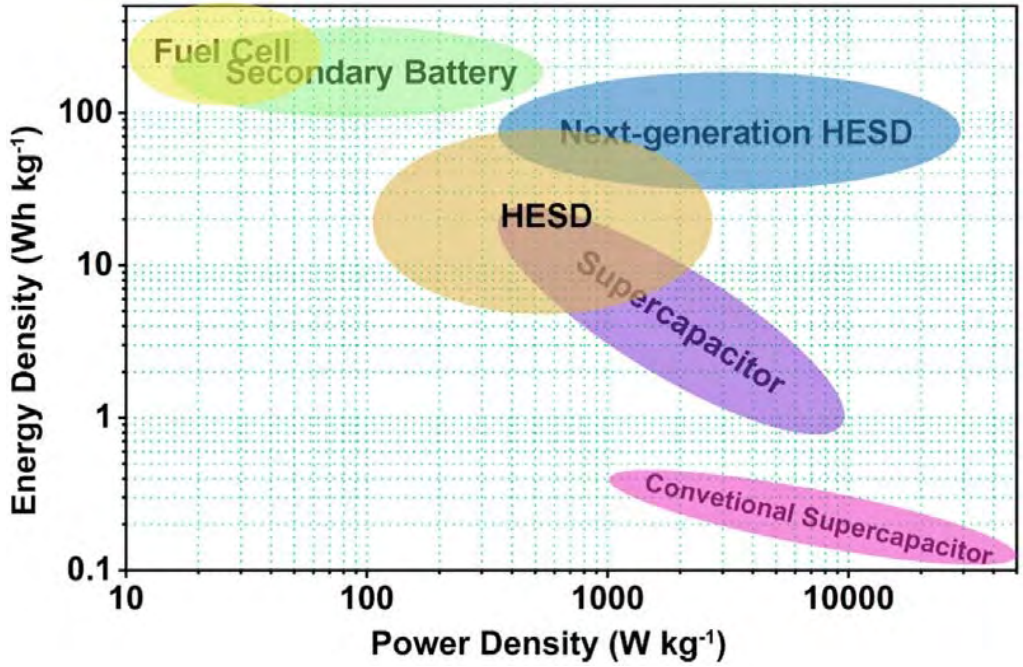

Figure 1.7 Energy-power comparison chart of various energy storage devices.[59] (Reproduced with permission from Elsevier and Copyright Clearance Center)

1.6. Classification of electrode material for supercapacitor

1.6.1. Carbon-based electrode material

Carbon materials have become one of the most important electrode materials for supercapacitors by virtue of their excellent chemical and physical characteristics, including low cost, high thermal/chemical stability and excellent electrical conductivity.[60] However, the corresponding electrochemical performance is restricted by the limited active sites, resulting in low capacity. Aiming to solve the problem mentioned above, the structure optimization and composition modification are employed to boost the capacitance of carbon-based electrode material. Many studies have proven that a large specific surface area can expose more reactive sites, a porous structure can shorten the ion/electron transmission path, and heteroatom-doping can improve the contact between the electrode and electrolyte combined with additional pseudocapacitive Faraday reaction.[61] At present, according to the various structures of

carbon material, the normally used carbon-based electrode materials can be divided into activated carbon, carbon nanotubes and graphene, which will be discussed in details subsequently.

1.6.1.1. Activated carbon

Activated carbon acts as a mostly used electrode material for supercapacitors. It can be prepared from various carbon-containing materials (such as biological waste, nut shells, and wooden materials) through physical or chemical activation procedures to introduce multiple porous structure insides the carbon framework.[62, 63] The resulted activated carbon can exhibit a porous structure combined with macropores, mesopores and micropores channels, realizing high electrochemical performance for supercapacitors benefited from its intrinsic high specific surface area and uniform pore size distribution.[64] Furthermore, the high conductivity of activated carbon can also have a great influence on the supercapacitor performance. For example, Elaiyappillai *et al.* reported various activated carbon materials prepared from multiple sources (including Cucumis melon/fruit peel), and tested as electrode materials for supercapacitor applications (**Figure 1.8**).[65] The cucumis melon-derived activated carbon electrode (named as Cm-900) with optimized surface composition and porous structure exhibits an excellent specific capacitance up to 404 F g^{-1} at a current density of 1 A g^{-1} in 1 M KOH solution. Besides, it also shows good cycle performance, which can still maintain 91% capacitance even after 8,000 charge and discharge cycles. Furthermore, the fabricated symmetric capacitor using Cm-900 as electrode material can also possess a high energy density 29.30 Wh kg^{-1} at a power density of 279.78 W kg^{-1}. Thus, the highly porous Cm-900 electrode is a promising electrode material for high-performance supercapacitors.

By constructing activated carbon with other carbon nanomaterials to induce a 3D network structure, the conductivity and active sites of the obtained electrode material can be also increased, resulting in a high supercapacitor performance. For example, Cheng *et al.* combined conventional activated carbon and carbon black with additional carbon nanomaterials (i.e., carbon nanotubes and carbon nanofibers) to develop a new class of nanocomposite electrodes for high-performance supercapacitors, as shown in **Figure 1.9**.[66] With the synergistic effects from these multiple components, the resultant nanocomposite electrodes exhibit superior performances in 1 M L^{-1}

tetraethylammonium tetrafluoroborate (TEA-BF_4)/acetonitrile (ACN) electrolyte. The optimized quaternary nanocomposite electrode shows a high packing density (0.63 g cm^{-3}), a high rate capability (capacitance retains 77.5% at 80 A g^{-1} vs. 0.5 A g^{-1}), a long cycle life (capacitance retains 91.4% after charging/discharging at 10 A g^{-1} for 30,000 cycles), and high volumetric performances (capacitance: 66.1 F cm^{-3}, energy density: 29.6 Wh L^{-1}, power density: 101.7 kW L^{-1}), significantly exceeding those of then supercapacitor performance. The nano-compositing approach developed in their work can be readily transferred into the industrial slurry process, utilizing commercially available materials to produce highly capacitive nanocomposite electrodes for manufacturing high-performance supercapacitor products at low costs.

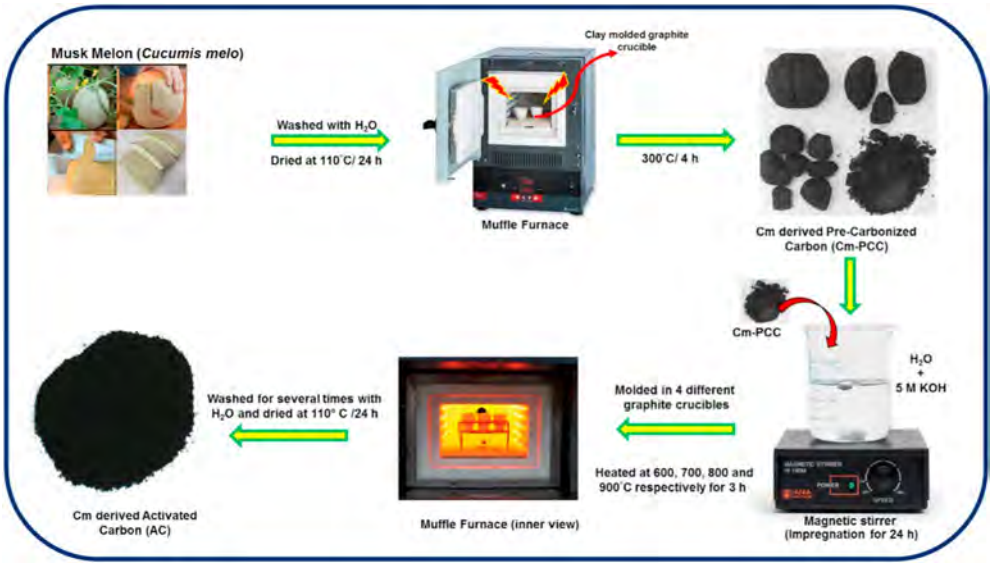

Figure 1.8 Schematic synthetic route of activated carbon samples from Cucumis melo/fruit peel.[65] (Reproduced with permission from Elsevier and Copyright Clearance Center)

Additionally, introducing heteroatom into the activated carbon structure can increase the overall electrochemical performance benefited from the generated pseudocapacitive active sites. For example, Zhang *et al.* reported the fabrication of nitrogen-doped activated carbon (NAC) materials via a convenient and low-cost method from polyethyleneimine (PEI) modified commercial activated carbon (AC), as shown in **Figure 1.10**.[67] After high-temperature treatment, nitrogen atoms were successfully introduced into the resulting AC matrix simultaneously the open porous structure of AC was well preserved. With the unique structure and heteroatom doping, the NAC material achieved a high capacitance value of 268 F g^{-1} from a symmetric supercapacitor in 1 M H_2SO_4 aqueous solution, as well as 226 F g^{-1} in 1 M 1-Ethyl-3-

methylimidazolium tetrafluoroborate in propylene carbonate (EMIM BF_4/PC) electrolyte with 3 V voltage window.

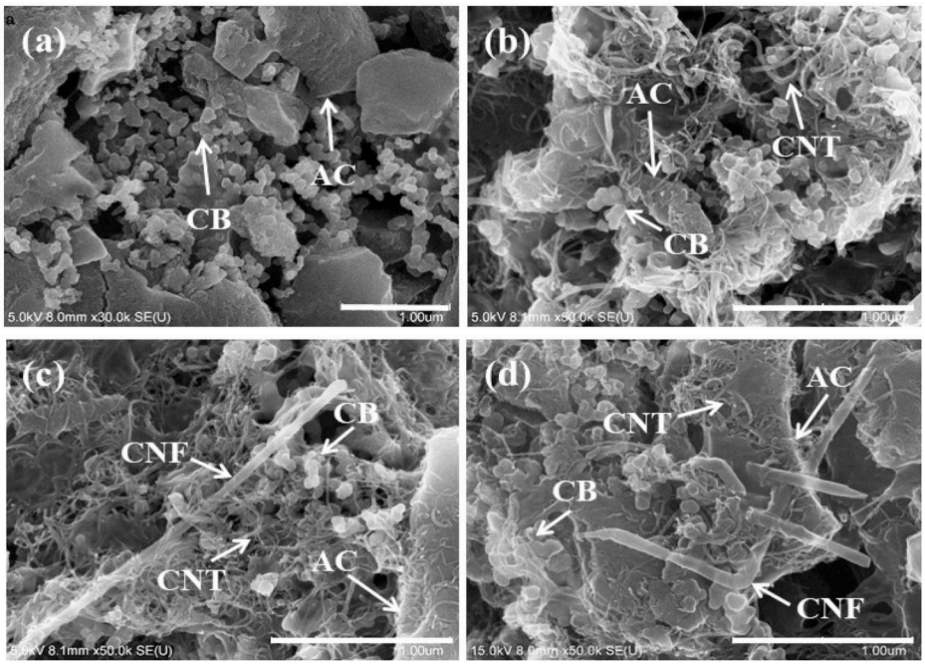

Figure 1.9 SEM images of (a) ACE, (b) NCE-1, (c) NCE-2, and (d) NCE-3 composite electrodes.[66] (Reproduced with permission from Elsevier and Copyright Clearance Center)

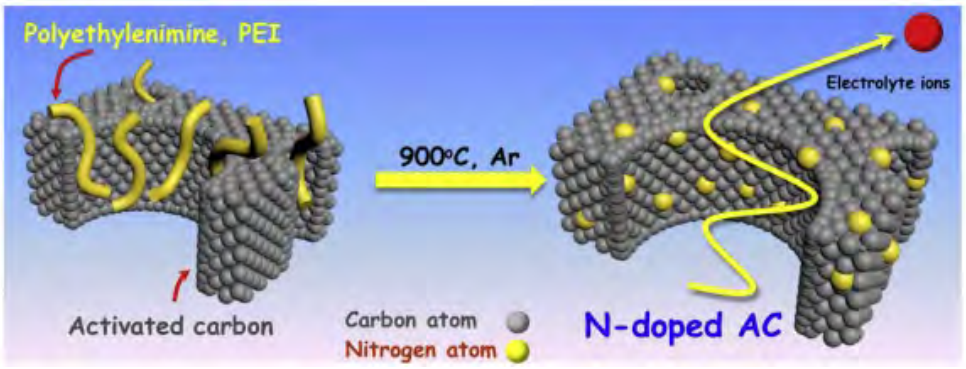

Figure 1.10 Schematic of the fabrication process of the NACs.[67] (Reproduced with permission from Elsevier and Copyright Clearance Center)

1.6.1.2. Carbon nanotubes

Normally, carbon nanotubes can be mainly divided into two categories: single-walled carbon nanotubes and multi-walled carbon nanotubes. Due to their unique one dimension structure, high conductivity, and chemical and mechanical stability, carbon nanotubes have become a very promising electrode material for supercapacitor.[68]

Single-walled carbon nanotubes are composed of a single graphene sheet, for example, Kanninen *et al.* fabricated single-walled carbon nanotube films by aerosol chemical vapor deposition method, exhibiting a high capacitance of 178 F g^{-1} at a current density of 0.53 A g^{-1} for flexible supercapacitors.[69] Multi-walled carbon nanotubes are composed of coaxial single-walled carbon with different sizes, for example, Wang *et al.* reported the synthesis of multi-walled carbon nanotubes as supercapacitor electrode material via chemical exfoliation process, showing a capacitance of 165 F g^{-1} at a current density of 0.5 A g^{-1}.[70] However, owing to the influence of the limited pore structure and intrinsic resistance between nanotubes, its capacitance for supercapacitor is still lower than the theoretical value of carbon material (550 F g^{-1}).[71] Therefore, nano composition and structure optimization strategies can be applied to improve the electrochemical performance of the composite material through the synergistic effect of the various carbon materials. For example, Zhang *et al.* prepared hierarchically porous carbon nanotube arrays on flexible carbon fibers (PCNTAs@CF, **Figure 1.11**), and showed high specific capacitance of 188 F g^{-1} at a high current density of 20 A g^{-1} using 6 M KOH as electrolyte within the voltage from -0.9 to 0 V. Moreover, during the 10,000 charge and discharge cycles, the capacitance loss was only 0.0016% per cycle, showing its excellent redox cycling stability.[72] This superior electrochemical performance is attributed to the unique structure of the hierarchical porous carbon nanotube array material, which provides a suitable channel for enhanced electron and ion transmission, increases the specific surface area of the electrode material, and expands the contact area between the material and electrolyte, which is conducive to the transport of a large number of electrolyte ions.

1.6.1.3. Graphene

Graphene is a two-dimensional planar structure formed by periodic interconnection of carbon atoms through six-membered rings, and the thickness is only the size of a single carbon atom (0.335 nm).[73] The unique atomic arrangement of graphene gives it many impressive properties, including a large specific surface area (theoretical value can reach 2,630 m^2 g^{-1})[74], excellent electronic conductivity (electron mobility can reach 200,000 cm^2 Vs^{-1})[75], thermal conductivity (thermal conductivity can reach about 5,000 W mK^{-1})[76], high mechanical strength (Young's modulus reaches about 1,100 GPa in comparison with the value of steel at about 200 GPa).[77, 78]

Therefore, graphene used as electrode material shows much potential on obtaining a high performance supercapacitor with high capacity and long cycle life.[79] However,

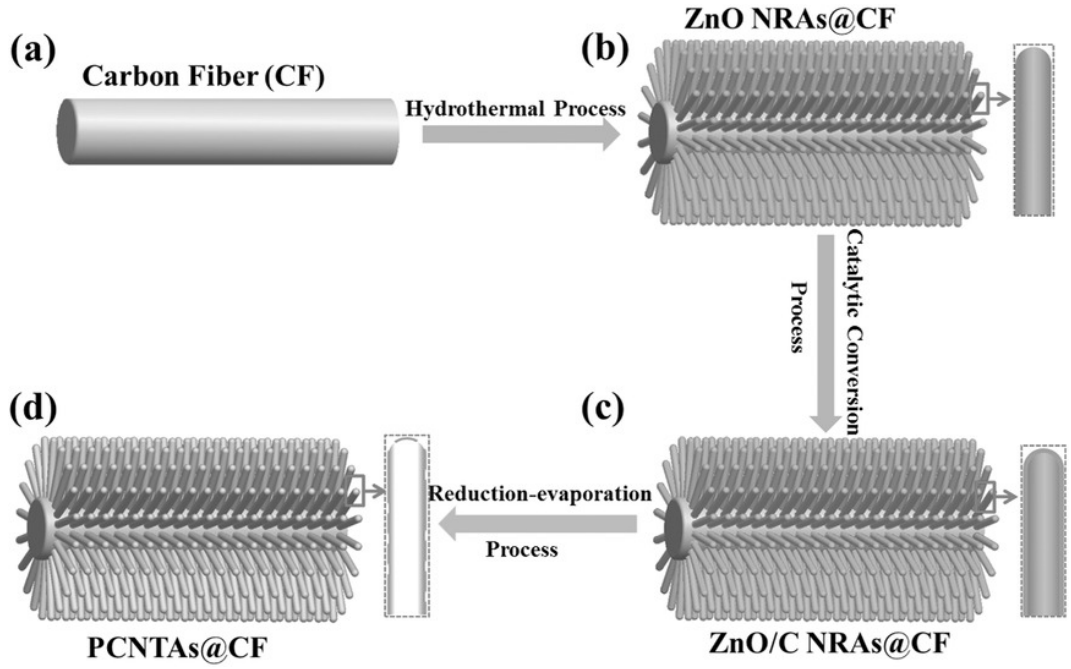

Figure 1.11 Schematic illustration of the fabrication processes of PCNTAs@CF: (a) Blank carbon fiber, (b) hydrothermal synthesis of ZnO NRAs on carbon fiber, (c) formation of ZnO/C core–shell NRAs on carbon fiber by ethanol decomposition, (d) hydrogen reduction-evaporation process to remove ZnO template, resulting in PCNTAs on carbon fiber.[72] (Reproduced with permission from John Wiley and Sons and Copyright Clearance Center)

the inevitable agglomeration and limited active sites are still the main problems for its wide application. At present, the optimization of graphene can be categorized into two methods. One is heat treatment, which reduces the oxygen-containing functional groups on the surface of graphene through high temperature treatment, thereby improving the conductivity and cycle stability of graphene. The other is heteroatom doping, which can increase the electronegativity of graphene and further improve the electronic structure of graphene, provide a large number of additional Faradic reaction active sites.

For example, Zhang *et al.* designed a nitrogen-doped 3D graphene network structure (named as GF-NG) by utilizing three-step annealing processes, as illustrated in **Figure 1.12**.[80] After synthesizing graphene aerogel network into the surface pf graphene foam (GF), the presence of XeF_2 can largely introduce ample defects into the graphene during the second annealing process, which is benefit for introducing nitrogen

species into the carbon framework in the third annealing step. The as-obtained GF-NG electrode shows excellent capacitances can be up to 380, 332, and 245 F g^{-1} in 6 M KOH, 1 M H_2SO_4, and 1 M KCl aqueous solutions, respectively. Additionally, the two-electrode system exhibits good redox cycling stability with 93.5% of the capacitance retention after 4,600 cycles. The excellent electrochemical performance can be attributed to the enhanced wettability, high N concentration (15.8 at%), and the large surface areas (583 m^2 g^{-1}) of GF-NG, resulting in more active sites exposed and pseudocapacitive contribution derived from the nitrogen species.

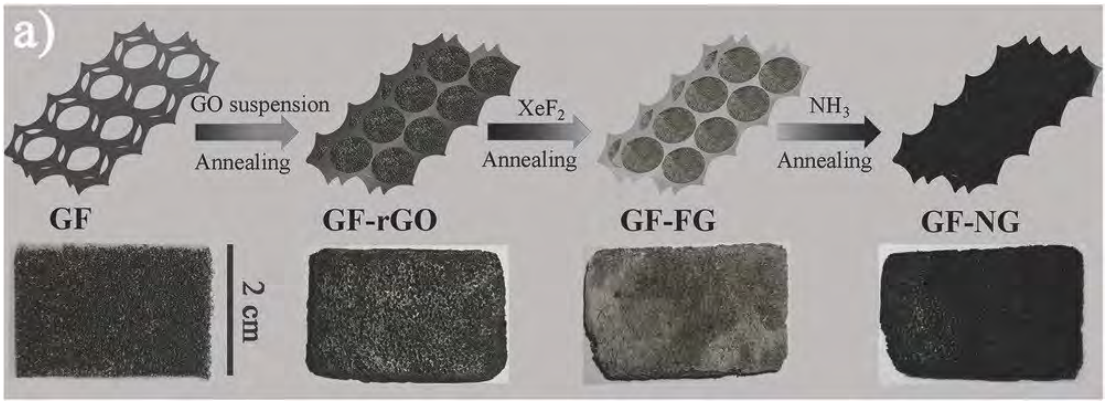

Figure 1.12 Schematic of the procedure for fabricating 3D GF-NG network macrostructure.[80] (Reproduced with permission from John Wiley and Sons and Copyright Clearance Center)

1.6.2. Pseudocapacitance electrode material

1.6.2.1. Transition metal-based electrode material

Most of the transition metal-based compounds (such as transition metal-based oxides, sulfides, phosphides) gradually become popular as electrode materials for supercapacitor because their peripheral electronic arrangements make them have multiple variable valences, showing high promise on obtaining electrode materials with rich redox active sites.[81] Notably, the ions from electrolyte will be rapidly transported at the interface of transition metal-based compounds and the electrolyte to induce redox reaction, giving the transition metal-based compounds high specific capacitances.[82] For example, RuO_2 is a very promising transition metal compound with a high specific capacity of 1,500-2,000 F g^{-1}.[83-85] However, the high cost of this noble metal makes it

difficult to commercialize. Therefore, many other low-cost transition metal-based compounds (such as NiO, Co_3O_4, Co_9S_8) have been investigated as electrode materials for supercapacitor.[86-88] However, the intrinsic low conductivity of this kind of material leads to a low rate performance and unsatisfied cycling stability, which is not conducive to the assembly of high-performance supercapacitors. Thus, the adjustment and optimization of the structure of such transition metal-based compounds can be treated as an effective strategy to reduce the resistance, expose more active sites, further improve the performance of the electrode material.

For example, Zhang *et al.* selected cobalt oxide as an example to demonstrate that the lithiation-induced vacancy engineering strategy can be used to enhance its electrochemical performance for supercapacitor. Detailed characterization reveals that electrochemical lithiation of Co_3O_4 crystal reduces the coordination of the Co-O bond, leading to substantially increased oxygen vacancies (octahedral Co^{2+} sites) as shown in **Figure 1.13**.[89] These vacancies further trigger the formation of a new electronic state in the bandgap, resulting in remarkably improved electrical conductivity and accelerated Faradic reactions. The lithiated Co_3O_4 exhibits a noticeably enhanced specific capacity of 260 mAh g^{-1} at 1 A g^{-1}, approximately fourfold enhancement compared to that of pristine Co_3O_4 (66 mAh g^{-1}). The hybrid supercapacitor assembled with lithiated Co_3O_4 // N-doped activated carbon tested in 6 M KOH with voltage from 0-1.5 V can achieve high energy densities in a broad range of power densities, e.g. 76.7 Wh kg^{-1} at 0.29 kW kg^{-1}, 46.9 Wh kg^{-1} at 18.7 kW kg^{-1}, outperforming most of the reported asymmetric supercapacitors.

Rafai *et al.* reported a gram-scale synthesis of non-layered ultrathin $CoNi_2S_4$ nanosheets via microwave-assisted liquid-phase growth of layered double hydroxide precursor post-sulfurized at room temperature. The method is time-saving and scalable for mass production. The fabricated $CoNi_2S_4$ nanosheets exhibit a micron-sized planar area, ultrathin thickness and mesoporous feature, as shown in **Figure 1.14**.[90] When loaded on flexible carbon cloth for electrochemical capacitor, the $CoNi_2S_4$ nanosheets deliver a high specific capacitance of 247 mAh g^{-1} at 8 A g^{-1} in 2 M KOH electrolyte within 0-0.55V, also achieving an excellent rate capability of 91% from 1 to 20 A g^{-1}. Remarkably, as a positive electrode material for asymmetric supercapacitor within voltage from 0-1.6 V, $CoNi_2S_4$ nanosheets demonstrate excellent electrochemical performances with a high energy density of 67.7 Wh kg^{-1} at a power density of 0.8 kW kg^{-1} and a robust long-term cycling stability up to 10,000 cycles.

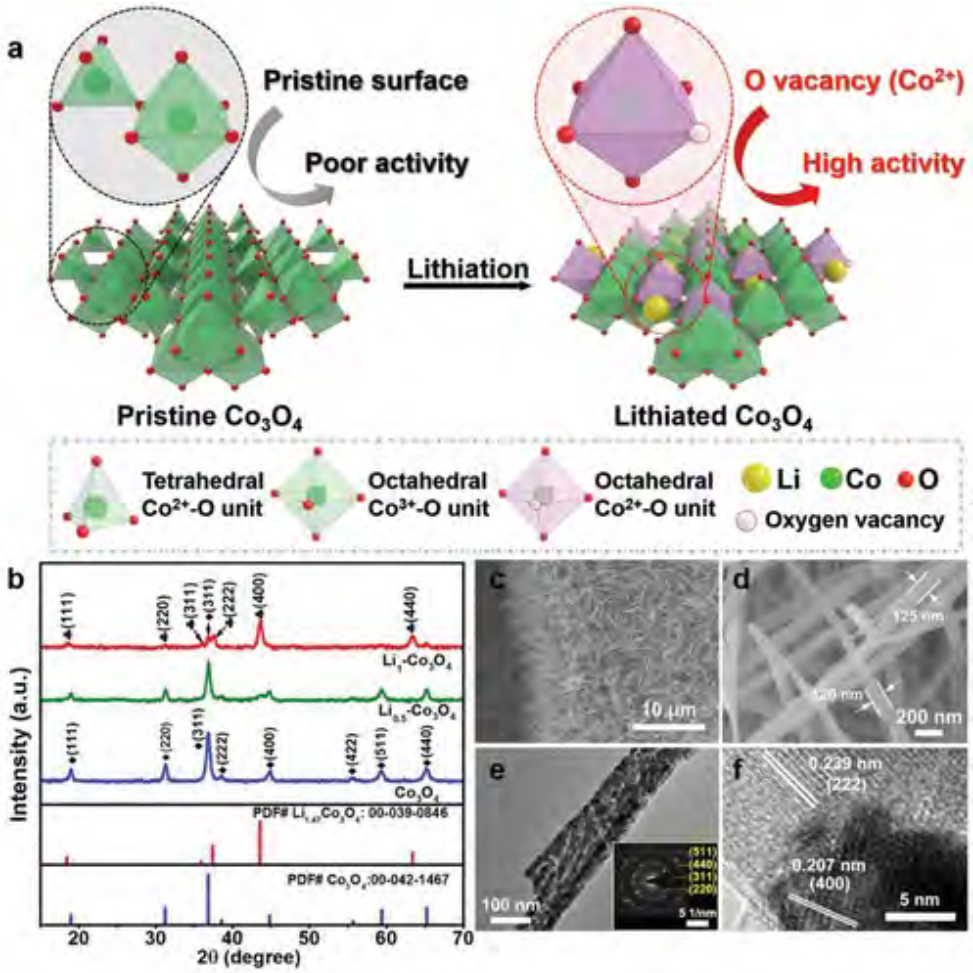

Figure 1.13 (a) Schematic illustration of the fabrication of lithiated Co_3O_4 via lithiation treatment, (b) Ex-situ XRD patterns of pristine Co_3O_4 and lithiated Co_3O_4 with different lithiation degree. The bottom vertical lines represent the standard PDF card of Co_3O_4 (blue lines) and $Li_{1.47}$-Co_3O_4 (red lines), (c,d) SEM images of Co_3O_4 NNs grown on Ni foam, (e) TEM image with SAED spectra inset and (f) HRTEM image of Li_1-Co_3O_4.[89] (Reproduced with permission from John Wiley and Sons and Copyright Clearance Center)

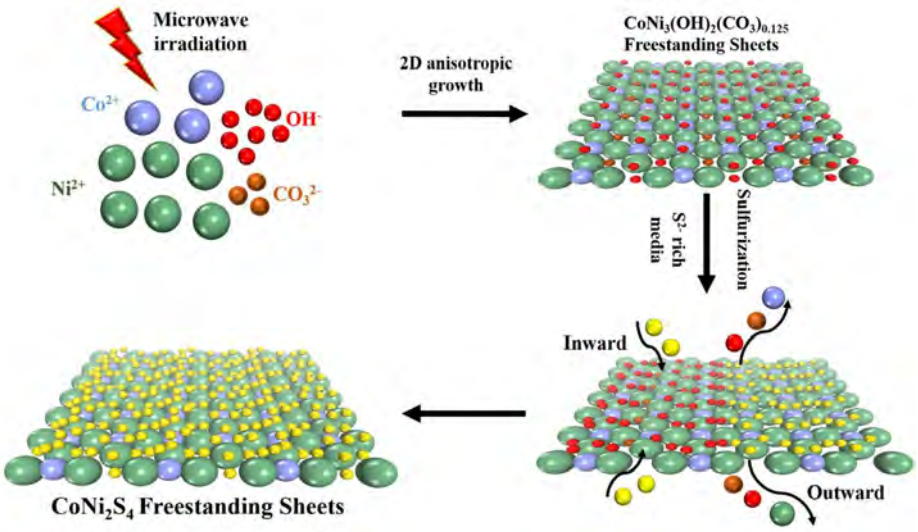

Figure 1.14 Schematic illustration of the preparation procedure of $CoNi_2S_4$ freestanding sheets.[90] (Reproduced with permission from Elsevier and Copyright Clearance Center)

Moreover, the structural stability of most transition metal-based compounds is another tough issue needed to be solved, because the redox reaction that occurs during the charge and discharge process is prone to cause structural collapse of the electrode material and further affect its electrochemical stability. Therefore, from the perspective of composite modification, high conductive substrate (such as carbon-based materials, nickel foam) with high conductivity and stability are normally used to alleviate the structural changes through decreasing the crystal size from micro to nano to relieve the structural strain. Besides, the large specific surface area of substrate is also beneficial for the exposure of active sites of transition metal compounds, leading to high electrochemical performance.

For example, Deng *et al.* first used electrodeposition to vertically deposit oriented $Cu(OH)_2$ on carbon fiber paper, and then further reversed self-assembly to form CoNi-MOF (**Figure 1.15**).[91] After being assembled with activated carbon to form an asymmetric supercapacitor and tested in 1 M KOH with voltage ranging from 0-1.5 V, its energy density can reach 28.5 Wh kg^{-1} while the power density is 1,500 W kg^{-1}, showing excellent energy and power density. This method can not only successfully prepare MOF electrodes for practical applications, but also broaden the application of transition metal compound materials in supercapacitors.

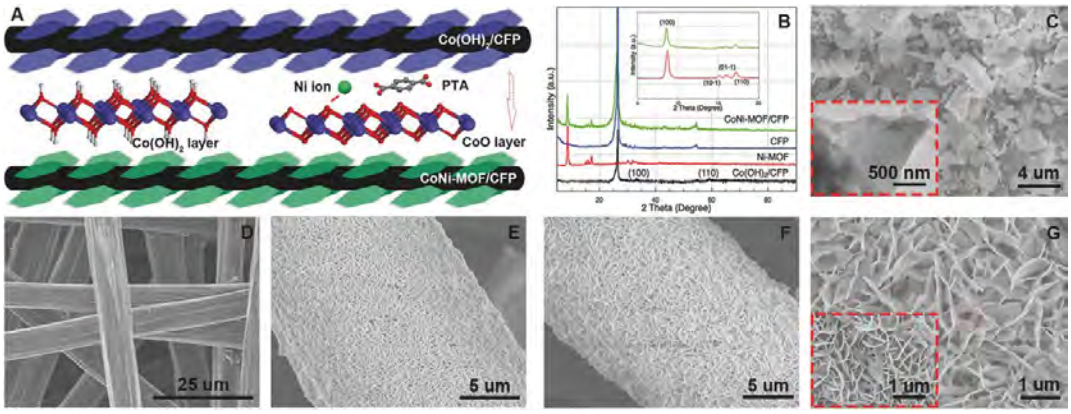

Figure 1.15 The schematic illustration of the strategy to synthesize CoNi-MOF and characterizations of Ni-MOF, CFP, $Co(OH)_2$, and CoNi-MOF, (A) $Co(OH)_2$ is used as both the template and precursor for in situ synthesis of CoNi-MOF, (B) XRD patterns of Ni-MOF, CFP, $Co(OH)_2$, and CoNi-MOF, (C–G) SEM images of Ni-MOF, CFP, $Co(OH)_2$, and CoNi-MOF. The inset of (C) is the TEM image of Ni-MOF. The inset of (G) is the SEM image of $Co(OH)_2$.[91] (Reproduced with permission from John Wiley and Sons and Copyright Clearance Center)

In summary, transition metal-based compounds (such as transition metal-based oxides, sulfides, phosphides) can be directly used not only as electrode materials, but also precursors to design and synthesize other composites electrode materials for supercapacitor. Through structural design and interface modification, the electrochemical activity of transition metal-based compounds can be effectively improved, showing excellent supercapacitor performance. The problems of structure pulverization and electrochemical instability during the cycling process may be solved by using composite modification strategy, making this type of electrode material have more opportunity in the application of supercapacitor.

1.6.2.2. Conductive polymer-based electrode material

Conductive polymer is a kind of organic polymer that uses conjugated double bond functional groups and large π bonds to conduct electricity, using chemical doping and stripping process to realize electrical energy storage.[92] In the past two decades, conductive polymers have been widely used in various supercapacitor energy storage devices due to their high conductivity and reversible redox characteristics.[93] Common conductive polymer electrodes include polypyrrole, polyaniline, and polythiophene

derivatives.[94] However, the conjugated structure of the conductive polymer will be destroyed during the chemical doping/stripping process, which can influence the cycling performance of this type of electrode material. In order to solve such a problem, structure optimization of the conductive polymer can be explored as one of the effective strategies, the resulting nano-structural conductive polymers (nanorods and nanosheets, etc.) show a large specific surface area and high porosity, coupled with high inherent conductivity. Furthermore, benefiting from the high surface area to volume ratio and nano-level surface effect, this type of electrode material can expose more reactive sites, exhibiting good electrochemical performance. For example, Zhou *et al.* prepared a pure polyaniline hydrogel (**Figure 1.16**) successfully by an in-situ polymerization method using vanadium pentoxide hydrate nanowires as oxidants and templates.[95] The obtained hydrogel is composed of ultra-thin polyaniline nanofibers. When it was tested as a supercapacitor electrode material using 1 M H_2SO_4 as electrolyte, it shows a specific capacitance of 636 F g^{-1} at a current density of 1 A g^{-1} within the voltage from 0-0.8 V. When the current density rises from 2 A g^{-1} to 25 A g^{-1}, its capacity retention rate is 98%, showing good rate performance. The capacity retention rate after 10,000 charge-discharge cycles is 83%, showing excellent cycle stability.

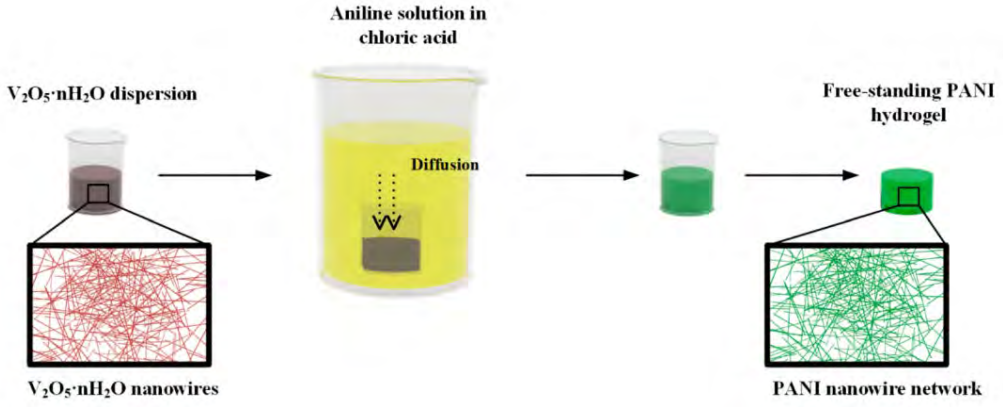

Figure 1.16 Schematic illustration of the fabrication route to a pure PANI hydrogel.[95] (Reproduced with permission from American Chemical Society)

In addition, by combining with carbon-based materials with good conductivity, the structural damage of the conductive polymer composite material during the electrochemical energy storage process can be also effectively alleviated. For example, Zhuo *et al.* used cellulose as a carbon precursor in the preparation of a hierarchical porous carbon aerogel as a support for polypyrrole (PPy). The hierarchical porous architecture not only enables the efficient penetration and uniform loading of PPy

throughout the carbon network, but also ensures a rapid transfer of electrolytes (1 M H_2SO_4) and the high accessibility of PPy (**Figure 1.17**).[96] The as-prepared hybrid material shows a high specific capacitance of 387.6 F g^{-1} (0.5 A g^{-1} in 1.0 M H_2SO_4) and excellent cycling stability (92.6% capacitance retention after 10,000 cycles). This work provides an effective method to sustainably fabricate porous composite electrodes from renewable cellulose for supercapacitor.

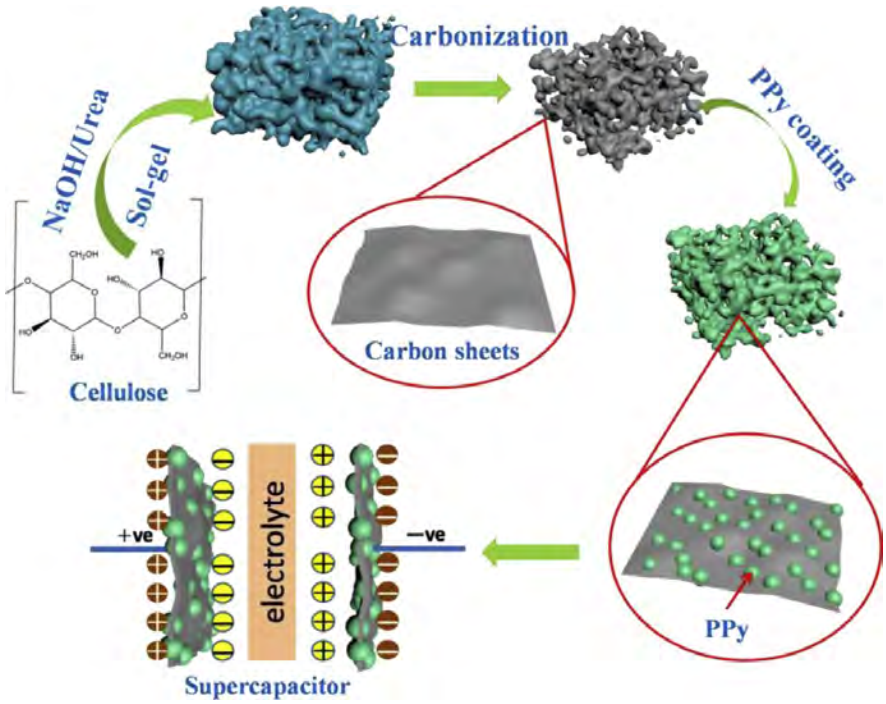

Figure 1.17 The fabrication of 3D hierarchical porous carbon aerogel/PPy composite for supercapacitor.[96] (Reproduced with permission from Elsevier and Copyright Clearance Center)

Therefore, towards the application of supercapacitors, the adjustable nanostructure of conductive polymer can increase the active sites on the surface of the electrode material, and the composite modification of conductive polymer with carbon-based material can improve the stability of the composite material, further enhancing its electrochemical performance. The improved structural stability and exposed active sites are two key parameters to boost the electrochemical activity of conductive polymers for the supercapacitor application.

1.7. Classification of electrolyte for supercapacitor

1.7.1. Aqueous electrolytes

Aqueous electrolytes can generally be divided into acidic (such as H_2SO_4), alkaline (such as KOH) and neutral electrolytes (such as Na_2SO_4). In recent years, aqueous electrolytes have been widely studied and applied in the laboratory, and most of the literature on supercapacitors is based on aqueous electrolytes.[20, 39, 97] This is mainly because aqueous electrolytes have higher ionic conductivity, higher ion concentration, and smaller solvated ions than organic electrolytes. Most importantly, the aqueous electrolyte has the advantages of low cost, easy preparation under ambient conditions, and environmental friendliness, which greatly simplify the assembly and manufacturing process.

Table 1.2 summarizes the hydrated ion size and ionic conductivity values for different species of cations and anions in aqueous electrolytes. It is worth noting that the choice of aqueous electrolyte not only affects the ionic conductivity but also influence the working voltage of the device. In general, the ionic conductivity of aqueous electrolytes is at least an order of magnitude higher than that of organic electrolytes and ionic liquids. Therefore, the aqueous electrolyte exhibits lower equivalent series resistance, which is beneficial to obtain higher power density. However, the major limitation is relatively low working voltage due to the decomposition voltage (1.23 V) of water.

Table 1.2 The sizes of hydrated ions and ionic conductivity values of different kinds of cations and anions in aqueous electrolytes.[20]

Ions	Hydrated Ion Sizes (Å)	Ionic Conductivity (S cm^2 mol^{-1})	Ions	Hydrated Ion Sizes (Å)	Ionic Conductivity (S cm^2 mol^{-1})
H^+	2.80	350.10	OH^-	3.00	198.00
Li^+	3.82	38.69	Cl^-	3.32	76.31
Na^+	3.58	50.11	SO_4^{2-}	3.79	160.00
K^+	3.31	73.50	NO_3^-	3.35	71.42
NH_4^+	3.31	73.70	PO_4^{3-}	3.39	207.00
Mg^{2+}	4.28	106.12	CO_3^{2-}	3.94	138.60
Ca^{2+}	4.12	119.00	ClO_4^-	3.38	67.30
Ba^{2+}	4.04	127.80			

1.7.2. Organic electrolytes

Organic electrolyte-based supercapacitors gradually dominate the commercial market owing to its large operating voltage window between 2.5 and 2.8 V.[20] Typical organic electrolytes for commercial EDLCs consist of the salts (e.g., tetraethylammonium tetrafluoroborate ($TEABF_4$) dissolved in the organic solvent (e.g., acetonitrile (ACN) solvent). Similar to aqueous electrolytes, the properties of salts and solvents, such as ion size, ion-solvent interaction, electrical conductivity, viscosity, etc., can affect the properties of organic electrolytes.[98] **Table 1.3** shows some commonly used salts and solvents, respectively.

Table 1.3 Summary of physical properties, limiting electrochemical reduction and oxidation potentials of commonly used organic solvents.[99]

Solvent	ε_r	**η (cp)**	**bp (°C)**	**mp (°C)**	**MW**
Propylene carbonate (PC)	65	2.5	242	-49	102
Butylene carbonate (BC)	53	3.2	240	-53	116
Acetonitrile (ACN)	36	0.3	82	-49	41
Dimethyl sulfoxide (DMSO)	49	2.0	189	19	78
Dimethyl carbonate (DMC)	3.1	0.6	90	4.6	90
Diethyl carbonate (DEC)	2.8	0.7	127	-43	118
Ethyl methyl carbonate (EMC)	2.9	0.65	109	-55	104
(DME)	2.3	0.45	-29.5	-141	46
Tetra ethylene glycol dimethyl ether (TEGDME)	12	4.01	275	-30	222

Abbreviations: ε_r, relative permittivity; η, viscosity; bp, boiling point; mp, melting point; MW, molecular weight.

However, organic electrolytes generally have higher cost, lower electrical conductivity, and safety concerns related to flammability, volatility, and toxicity compared with aqueous electrolytes. In addition, organic electrolytes have higher requirements on the environment, and the device assembly process needs to be carried out in a strict environment to avoid introducing impurities into the air to affect their performance.

1.7.3. Ionic liquid electrolytes

Ionic Liquids (ILs) are generally defined as room temperature molten salts consisting of only organic cations and organic/inorganic anions. Generally, ILs are characterized by high thermal, chemical and electrochemical stability, negligible volatility and non-flammability.[100] Since most ILs are liquids, they can be directly used as electrolytes without adding additional solvents. However, compared with aqueous electrolytes and organic electrolytes, the lower ionic conductivity makes its performance unsatisfactory at high power output. Even for the mostly used ILs, $EmimBF_4$ (~14 mS cm^{-1}), the ionic conductivity is far from being able to meet the needs of high power.[101] In addition, a small amount of water will have a great impact on the electrochemical performance of ILs in practical applications, which means that the preparation and use conditions of ILs are more severe.

The common anions in ILs are BF_4^-, PF_6^-, $TFSI^-$, FSI^- and DCA^-, while the cations are mainly imidazole, pyrrole, ammonium and phosphonium salts.[102, 103] Each type of anion or cation has different properties, thus ILs with targeted properties can be obtained by designing the structure of the anion/cation or by combining different anions/cations. The high-temperature resistance of ILs also makes them beneficial for high-temperature applications. In addition, in order to reduce the viscosity of ILs and improve the conductivity of ILs (especially at low temperature), a mixed solution of ILs and organic solvents can be used as electrolytes for supercapacitors.[104]

1.8. Research objectives

As mentioned above, selecting the electrode materials to match suitable electrolytes is very critical for designing supercapacitors with high energy density. The carbon-based electrode materials have shown much potential on obtaining high-performance supercapacitor, owing to its outstanding properties such as high conductivity, easily modified surface area, potentially high specific area, high chemical and physical stability. However, the main challenge is still obvious and restrains the realization of high-performance carbon-based electrode material, that is the suitable design and synthesis of novel electrode materials to achieve high adaptability with specific electrolyte condition under the consideration of unique interface environment and reaction among the electrode/electrolyte. Therefore, novel carbon-based electrode materials with optimized sizes and structures will be fabricated in the present study through controllable synthesis strategy, aiming to synergize with specific electrolyte condition for achievement of high-performance supercapacitors. On this basis, the objectives are to explore the electrochemical processes, analyze the relationship between structure and effect, optimize the interfacial processing environment of the carbon-based electrode materials in the configuration process, and finally achieve the goal of high energy density, high power and long cycle life of supercapacitors.

The specific research approaches are presented as follow:

Firstly, aiming to boost the electrochemical performance of SCs using carbon material as both positive and negative electrodes, it is widely accepted that the introduction of redox species in the neutral electrolyte can contribute additional capacitance via fast faradic/redox reaction at the carbon electrode/electrolyte interface. Herein, a serious of nitrogen-doped porous carbon materials with optimized structure and composition will be developed for accelerating the redox reaction of iodide species to enhance the resulted energy density.

Secondly, the hybrid design of SCs using carbon material as negative electrode and redox active material as positive electrode can largely broaden the working voltage in alkaline electrolyte, thus potentially leading to high energy density of SCs. Herein, carbon fiber is chosen as conductive substrate to provide deposition sites for nickel cobalt layer double hydroxides, followed by conformal coating of conductive PEDOT skin onto the obtained positive electrode to enhance overall electrochemical performance of SCs.

Thirdly, organic electrolyte with sodium salt is further applied to replace aqueous electrolyte to offer a wider operation voltage. The boron-doped porous carbon material will be developed through facile one-step synthesis strategy. The introduced hierarchically porous structure coupled with boron-doped active sites of as-made anode material are considered to be employed as high-rate anode electrode material by increasing the slope contribution to match the capacitive carbon cathode, leading to a high-performance sodium ion capacitor.

Chapter 2 Experimental Section

2.1. Chemical list

In this research, the major chemicals used are summarized in **Table 2.1** below.

Table 2.1 The chemical list

Chemical Name	Key Parameter	Supplier
3,4-Ethylenedioxythiophene	⩾97.00 wt. %	Sigma Aldrich
Activated carbon	⩾99.99 wt. %	Kurary
Boric acid	⩾99.00 wt. %	Sigma-Aldrich
Carbon black	⩾99.99 wt. %	Kurary
Carbon fiber	⩾99.00 wt. %	TORAY
Chitosan	⩾95.00 wt. %	Sigma-Aldrich
Citric acid monohydrate	⩾99.00 wt. %	Sigma-Aldrich
Cobalt sulfate heptahydrate	⩾99.00 wt. %	Sigma-Aldrich
Deionized water	~18 MΩ*cm	Synergy
Ethyl alcohol	⩾95.00 wt. %	Anaqua (Hong Kong)
Glass fiber	25 um	Whatman
Hydrochloric acid	35~37 wt. %	DUKSAN
Methyl alcohol	⩾99.90 wt. %	Anaqua (Hong Kong)
$NaPF_6$ electrolyte	1 mol L^{-1} in Diglyme	DoDoChem
Nickel foam	1.5 mm	Cyber Electrochemical Materials Company
Nickel sulfate hexahydrate	⩾99.00 wt. %	Sigma-Aldrich
N-methyl-2-pyrrolidone	⩾95.00 wt. %	Sigma Aldrich
Non-woven fabrics	100 um	NKK Switches
Polytetrafluoroethylene aqueous solution	~60wt. %	DAIKIN
Polyvinylidene fluoride	⩾99.50 wt. %	MTI Corporation
Potassium hydroxide	⩾85.00 wt. %	Sigma-Aldrich

Potassium iodide	⩾99.00 wt. %	Sigma Aldrich
Sodium	⩾99.90 wt. %	Sigma Aldrich
Sodium sulfate	⩾99.00 wt. %	Sigma Aldrich
Thiourea	⩾99.00 wt. %	Sigma-Aldrich
Vanadium trichloride oxide	⩾99.00 wt. %	Sigma Aldrich
YP-50	⩾99.99 wt. %	Canrd Kukdo Chemical
Zinc nitrate hexahydrate	⩾99.00 wt. %	Sigma-Aldrich

2.2. Materials characterization

2.2.1. Transmission electron microscopy (TEM)

Transmission electron microscopy (TEM) projects an accelerated and concentrated electron beam onto a very thin sample. The electrons collide with atoms in the sample to change direction, resulting in solid angle scattering. The size of the scattering angle is related to the density and thickness of the sample, so an image with different brightness can be obtained.[105, 106]

The instrument used in this experiment is Jeol JEM-2100F. The testing samples will be prepared as follows: Disperse 1 mg samples in 2 mL anhydrous ethanol solution under ultrasonic mixing; then use a pipette to suck as-prepared solution on the copper micro grid (300 mesh). Finally, the copper micro grid is dried under ambient conditions and stored in plastic pipe before testing.

2.2.2. Scanning electron microscope (SEM)

Field emission scanning electron microscope (FESEM) generates a finely focused electron beam that bombards the surface of the sample, where secondary electrons, backscattered electrons, X-rays, and visible fluorescence are present on the surface of the sample.[107] Thus, it is possible to observe and analyze the surface morphology of the sample. Besides, the combination of FESEM and energy spectroscopy (EDS) can reveal the composition of the sample.

Sample preparation and testing: Stick the conductive tape on the circular stage and use it to stick 1 mg sample on the glass slide (the sample with poor conductivity needs to be sprayed with gold on the surface), followed by loading it into the microscope for testing. The instrument employed in this experiment is TESCAN MAIA3 field emission scanning electron microscopes.

2.2.3. Chemical composition and structural analysis

X-ray diffraction (XRD): X-ray diffraction is used to analyze the composition and crystal structure of materials by analyzing the diffraction results of X-ray interaction with the materials. The phase composition of the material can be analyzed by the position and intensity of the diffraction peak using Cu-Kα radiation (λ = 1.5406 Å) (D/max 2500PC, Rigaku, Japan). For a typical testing, the sample powder is first placed into the glass slide tank (2 cm x 2 cm) and flattened with a clean glass slide into the X-ray diffractometer. The scanning range of the test sample is 10-80° and the scanning speed is 10° min^{-1}, which has been widely accepted in determining crystal structures of inorganic materials.[108] The obtained spectra are processed with JADE6 software and compared with standard cards inside the software to analyze the substances.

Raman spectroscopy: Raman spectroscopy uses the frequency difference between Raman scattered light and incident light to characterize molecular vibrational rotation energy levels. The interaction of photons with molecules causes the electron cloud to deform, which is called polarization change. Molecular bonds have specific energy transitions and changes in polarization during this process lead to Raman activity. The model of the Raman spectrometer used in this experiment is WITEC Confocal Raman system. The excitation wavelength of the argon ion laser is 532nm.

X-ray photoelectron spectroscopy (XPS): X-ray Photoelectron Spectroscopy (X-ray Photoelectron Spectroscopy) tests reflect the energy, intensity, angular distribution and other information of electrons emitted by atoms under the action of X-rays. 1 mg of sample is dispersed onto conductive tape for XPS testing. The XPS test instrument model in this experiment is Thermo Fisher Neasa.

Brunauer–Emmett–Teller (BET): The BET test is to determine the specific surface area, pore volume and pore size distribution of the material by performing nitrogen isothermal adsorption and desorption analysis on the material using

Micromeritics ASAP 2020. The results are based on the BET multilayer adsorption theory and BJH pore size theory.[109]

2.3. Electrochemical characterization

2.3.1. Cyclic voltammetry (CV)

One of the preferred research methods in electrochemistry is cyclic voltammetry (CV) testing. By controlling the electrode potential at different scan rates, one or more repeated scans in triangular waveforms over time complete the cycle of reduction and oxidation processes.[110] In this way, the relationship between the current change and the electric potential is obtained. According to the shape of the curve, the degree of reversibility of the electrochemical reaction, the possibility of intermediates, phase boundary adsorption or new phase formation, and the nature of the coupling chemical reaction can be observed. It is commonly used to measure electrode reaction parameters, determine its control steps and reaction mechanism, and observe which reactions can occur within the entire potential scanning range.

In this experiment, the electrochemical workstation Metrohm Autolab (NOVA) will be used to measure the electrode material at different scanning rates. The mass specific capacitance of the electrode material can be calculated for the supercapacitor according to formula (2-1).

$$C = \frac{\int IdV}{mv\Delta V} \tag{2-1}$$

Where:

C: specific capacitance (F g^{-1}); I: current density (A g^{-1});

m: mass of active material (g); ΔV: voltage range of scanning (V);

υ: Scanning speed (V s^{-1}).

2.3.2. Charge and discharge test

The constant galvanostatic charge/discharge (GCD) test is to apply a constant current to the electrode material to perform a charge and discharge test.[111] The specific capacity, rate performance, cycle stability, power density and energy density of electrode materials are studied by recording the changing curves of electric potential over time.

The specific capacity of supercapacitor electrode materials can be calculated according to formula (2-2):

$$\mathrm{C} = \frac{I}{m\frac{dV}{dt}} \tag{2-2}$$

Where:

C: specific capacitance (F g^{-1}); I: current density (A g^{-1});

m: the mass of electrode active material (g); t: discharge time (s).

2.3.3. The calculation of energy density and power density

Energy density and power density are calculated according to formula (2-3) and (2-4), respectively.

$$\mathrm{E} = \frac{C(\Delta V)^2}{2 \times 3.6} \tag{2-3}$$

$$\mathrm{P} = \frac{E}{t} \times 3600 \tag{2-4}$$

Where:

C: the specific capacitance, F g^{-1} ΔV: the potential window, V

t: the discharge time, s.

2.3.4. Electrochemical impedance spectroscopy (EIS)

When the electrode system is disturbed by a sinusoidal voltage (current) AC signal, a corresponding current (voltage) response signal will be generated, from which the impedance or admittance of the electrode can be obtained. The impedance spectrum

generated by a series of frequency sine wave signals is called electrochemical impedance spectrum.[112]

Under the action of a small amplitude disturbance signal, an electrode system has a linear relationship between the response of various dynamic processes and the disturbance signal. Each dynamic process can be electrically connected to a linear element or a combination of several linear elements. For example, the charge transfer process can be represented by a resistor, and the charge and discharge process of an electric double layer can be represented by the charge and discharge process of a capacitor. In this way, the electrochemical dynamics process is described by an equivalent circuit, and the value of each element of the equivalent circuit is obtained through the disturbance response of the electrode system, thereby inferring the reaction mechanism of the electrode system. At the same time, the electrochemical impedance spectroscopy method is a frequency domain measurement method. It uses the measured impedance spectrum with a wide frequency range to study the electrode system, so it can obtain more kinetic information than other conventional electrochemical methods.[113, 114]

2.3.5. The calculation of diffusion coefficient

The ion diffusion coefficient of supercapacitor electrode materials can be calculated according to formula (2-5):

$$\mathrm{D} = \frac{4}{\pi\tau}\left(\frac{m_B V_B}{M_B S}\right)^2\left(\frac{\Delta Es}{\Delta E\tau}\right)^2 \qquad (2\text{-}5)$$

Where:

D: ion diffusion coefficient ($cm^2\ s^{-1}$);

M_B: molar mass ($g\ mol^{-1}$);

τ: current pulse time (s)

S: active surface area (cm^2);

m_B: active material weight (g);

ΔEs: potential change of discharging process (V);

V_B: molar volume ($cm^3\ mol^{-1}$);

$\Delta E\tau$: potential change of pulse-relaxation (V).

Chapter 3 Nitrogen-Doped Porous Carbon Electrode for Aqueous Iodide Redox Supercapacitor

3.1. Introduction

Supercapacitors (SCs) have drawn considerable attention from academia and industry because of their promising high-power capability and long service life.[115-117] This kind of device usually stores charge by reversible physisorption and accumulation of charge carriers on the surface of the polarized electrodes.[118] Hence, most of the previous studies on SCs have focused on the development and fabrication of porous carbon electrodes with a large specific surface area (SSA) and a well-fitted pore structure.[119-121] Nevertheless, the main drawback of the relatively low charge capacity for the porous carbon electrodes still limits the practical application of SCs, especially for aqueous systems.[122] It is known that the introduction of redox species, such as iodide (I^-/I_3^-), bromide (Br^-/Br^{3-}), molybdate (MoO_4^{2-}), and hydroquinone (HQ) into the aqueous electrolytes can boost the electrochemical performance of SCs via fast faradic/redox reaction at the carbon electrode/electrolyte interface.[123-126] For example, Hwang *et al.* reported a high energy density of 19.8 Wh kg^{-1} by adding 0.1 M ferricyanide/ferrocyanide redox species into the aqueous Na_2SO_4 electrolytes using the laser-scribed activated carbon electrode.[127] Tang *et al.* achieved high capacity retention over 86% after 10,000 cycles in 1 M Na_2SO_4 electrolyte with addition of bromide as redox-active species using the functionalized carbon nanotube.[125] Despite these advances in the aqueous redox electrolytes of carbon-based supercapacitors, insights regarding the relationship between the redox chemistry of electrolyte and carbon surfaces remain extremely inadequate. Moreover, the most reported aqueous redox systems with common or unmodified carbon still show unsatisfactory electrochemical performance. How to optimize the microstructures and surface properties of carbon electrodes to accelerate the faradaic reactions of redox species in the aqueous electrolyte remain a tough challenge for high-performance SCs.

Two-dimensional (2D) porous carbon nanosheets with a high aspect ratio have been shown recently as the promising electrode materials because of the large SSA and short ion/electron transport pathway.[117, 128-130] Their surface electronic structure and additional active sites derived from the 2D carbon nanosheets can be tuned by doping

various heteroatoms (boron, nitrogen or phosphorus) within the lattice of carbon scaffolds.[131-133] The target carbon materials can also be obtained easily through the ingredient control of precursors including fossil fuel, biomass, and polymers.[134-136] Thus, a series of heteroatom-doped, especially nitrogen-doped porous carbon nanosheets have been prepared to understand the performance of electrochemical catalysts involving redox chemistry.[137] However, the performance of the heteroatom-doped carbon electrode has rarely been explored for the aqueous redox supercapacitors. Consequently, a systematic study is required to gain an in-depth understanding of the heteroatom-doped strategy for tuning surface properties of porous carbon nanosheets and of the fundamental energy storage mechanism of such materials in supercapacitors with aqueous redox electrolytes.

In this part of the study, a facile strategy is presented for scalable synthesis of 2D N-doped porous carbon nanosheets from dual-crystals (ice and zinc nitrate) templating assisted carbonization of various precursors including chitosan (CS), polyvinylpyrrolidone (PVP), and polyvinyl alcohol (PVA). It also deserved be noted that the strategy proposed is the first time to utilize water and zinc nitrate as template to fabricate carbon-based material for supercapacitor in redox electrolyte. Interestingly, the SSA and nitrogen configurations of the as-prepared 2D porous carbon nanosheets can be tuned by controlling the carbonization temperature. Thus, the optimal electrochemical performance of supercapacitors can be obtained by varying the carbonization temperature. The relationship can also be investigated between the properties of carbon surfaces and redox chemistry of the electrolytes. Specifically, the CS-derived 2D N-doped carbon nanosheets was employed as the electrodes for supercapacitors with the aqueous iodide (I^-/I_3^-) redox electrolytes. It delivered the highest energy and power densities of 22.4 Wh kg^{-1} and 15.2 kW kg^{-1}, respectively, as well as the excellent stability of 96.5% capacitance retention after 30,000 charging/discharging cycles. The capacity fade is due to the reason that the micropore is trapped by ions or slight collapse of carbon structure. Besides, the relationship between the redox chemistry of electrolytes and carbon surfaces from different nitrogen configurations is further explored systematically based on the experimental results and theoretical analysis. The graphitic N content is found to be a vital factor that greatly determines the electrochemical performance of redox supercapacitors.

3.2. Experimental section

3.2.1. Fabrication of two-dimensional porous carbon nanosheet derived from biomass or polymer

Figure 3.1a schematically illustrates the facile strategy for the fabrication of nitrogen-doped porous carbon nanosheets assisted by a general dual crystal-template.[138, 139] The typical procedure is as follows: 1 g of chitosan (CS) was dissolved in 30 mL deionized water with a stirring process for 20 minutes, forming a sticky and clear solution of 0.033 g mL^{-1} in room temperature. After that, 1 g zinc nitrate hexahydrate ($ZnNO_3 \cdot 6H_2O$) was added into the 30 mL solution obtained above, followed by heating to 70 ^oC and kept stirring for another 20 minutes to uniformly dissolve $ZnNO_3 \cdot 6H_2O$ into the solution. The obtained transparent solution was frozen at -20 ^oC for 12 hours and then lyophilized at -20 ^oC and an intensity of pressure around 10 Pa, respectively. It is noted that the $ZnNO_3$ nanocrystals grow with the 2D ice crystals in parallel under a low-temperature condition, leading to abundant sheet-like scaffolds filled in the nano-space of the carbonaceous precursors.[140, 141] The $ZnNO_3$ crystals here are not only utilized as the support template but also as pore-creating agents for the activation of CS precursors undergoing the lyophilization and carbonization processes, aiming to provide ample porous pathway for electron/ion transportation.[134] Then, the fluffy precursor was annealed and carbonized at various temperatures from 600 to 1000 ^oC. The carbonized samples were further immersed into 1 M HCl solution to wash out the impurities. The two-dimensional nitrogen-doped porous carbon nanosheet can be prepared finally after drying overnight at 70 ^oC in a normal drying oven. The corresponding samples were named as NC-*x*, with *x* being the carbonization temperature in degree Celsius, e.g. NC-600, NC-700, NC-800 NC-900, and NC-1000 respectively. As to the preparation of other polymer precursors, the PVA or PVP is chosen and treated by following the same procedures as NC-*x* above. The as-obtained two precursors were annealed at a certain temperature to synthesize two-dimensional porous carbon nanosheets, respectively.

The as-prepared NC-*x* samples can be regarded as configuration demos to investigate the factors affecting the redox chemistry of I^-/I_3^- couples in the aqueous

electrolytes, as shown in **Figure 3.1b**. Importantly, this strategy offers many possibilities in the fabrication of the NC-*x* samples on a large scale (**Figure 3.2**).

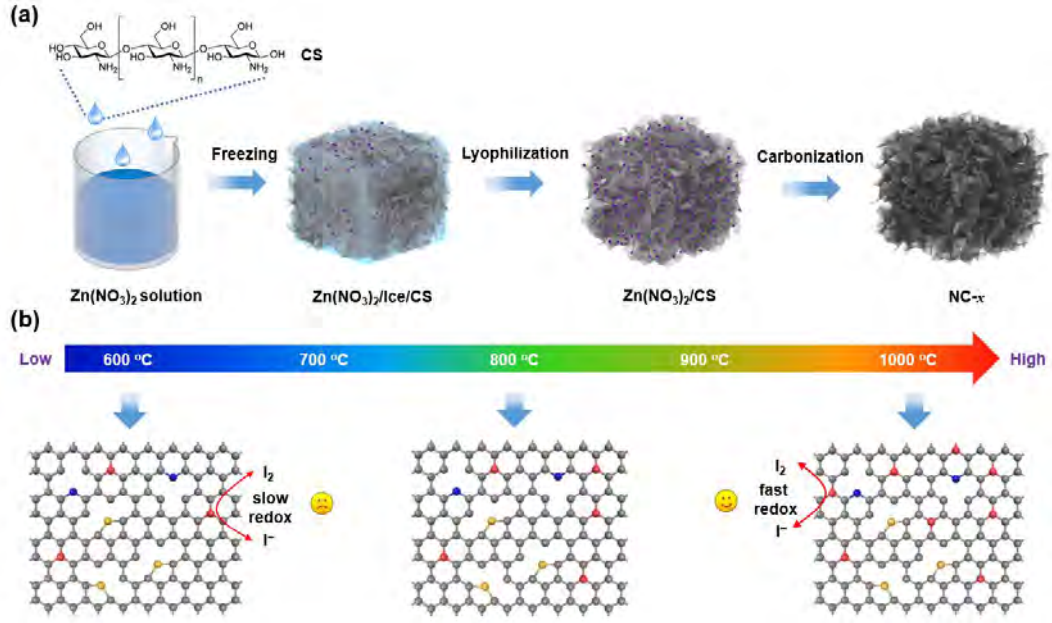

Figure 3.1 (a) The schematic illustration of the fabrication of NC-*x* samples represented by chitosan. (b) The structural configuration evolution of NC-*x* at various temperatures from 600 to 1000 °C.

Figure 3.2 The digital photograph of as-made carbon-based precursor.

3.2.2. Material characterization

The microstructure information and electrochemical performance of the as-made samples were detected by a series of characterization equipment and testing technologies. X-ray diffraction (XRD6100) and Raman spectroscopy patterns (Laser Raman Spectrometer, laser excitation at 532 nm) were carried out to test the

microstructure information of the as-prepared samples. The corresponding surface chemical states were measured and recorded by X-ray photoelectron spectroscopy (Thermo Fisher ESCALAB Xi+). The surface structures and morphologies of the as-made samples were observed by field-emission scanning electron microscopy (FE-SEM) and transmission electron microscopy (TEM) taken on MAIA3 LMH and JEOL JEM-F200. Additionally, the detailed Brunauer-Emmett-Teller (BET) surface area and the pore size distributions were investigated by employing Micromeritics ASAP 2460 as a nitrogen adsorption/desorption isotherms analyzer.

3.2.3. Electrochemical characterization

For the assembly and test of the supercapacitor, the working electrode was made of the composite film derived from the mixture of 80 wt% of as-made carbon materials, 15 wt% of acetylene black, and 5 wt% of polytetrafluoroethylene (PTFE). The resulting film electrodes with areal densities of 2~3 mg cm^{-2} are further coated onto the metal current collector. Electrochemical tests were firstly carried out using a two-electrode system. The two same working electrodes were separated by a piece of non-woven fabric as the separator to assemble in the symmetrical device. The obtained symmetrical devices were tested in 2 M Na_2SO_4 electrolytes with or without 0.05 M KI species. The low concentration of KI species used can solve the problem of iodine crossover in high concentration. The cyclic voltammetry (CV) and galvanostatic charge-discharge (GCD) were performed on a Biologic VMP3 workstation at room temperature of 25 ^{o}C. Furthermore, the LANHE CT3001A was employed to test the cycling performance.

3.2.4. Theoretical calculation

The spin-polarized Perdew-Burke-Ernzerhof (PBE) version of the generalized gradient approximation (GGA) was treated as the exchange-correlation functional meanwhile associated with the projector-augmented wave pseudopotential for electron-ion interaction.[142-145] Grimme's zero damping DFT-D3 method was further considered because of the weak van der Waals dispersion forces between the adsorbates and the surfaces.[146] The Monkhorst-Pack k-point sampling of 1 × 1 × 1 and 2 × 2 × 2 was selected for adsorption thermodynamics and charge density calculations,

respectively.[147] For the calculations of total energy, plane-wave kinetic cutoff energy of 400 eV was set to expand the valence electronic states. All atoms were optimized until the Hellman-Feynman force of each atom was lower than 0.05 eV $Å^{-1}$.

To simulate the graphene nanosheets with or without various nitrogen-doped structures, four substrate models were built, containing graphene model, pyridinic N/ pyrrolic N/graphite N species-doped graphene models, respectively. To study the interactions between the above four surfaces and the I_2/I*, the 25 Å × 25 Å conditions in the x-y plane coupled with the vacuum space of 20 Å in the z-direction is set to avoid the interactions of adjacent slabs.

The adsorption energy of I_2 molecule ($E_{ads}^{I_2}$) is defined as[148]:

$$E_{ads}^{I_2} = E_{total}^{I_2} - (E_{substrate}^{I_2} + E^{I_2}) \quad (3\text{-}1)$$

Where $E_{total}^{I_2}$, $E_{substrate}^{I_2}$ and E^{I_2} represent the total energies of adsorbate-substrate, substrate and isolated adsorbate, respectively.

The adsorption energy of I* ($E_{ads}^{I^*}$) is defined as:

$$E_{ads}^{I^*} = E_{total}^{*} - (E_{substrate}^{*} + 1/2E^{I_2}) \quad (3\text{-}2)$$

Where E_{total}^{*}, $E_{substrate}^{*}$ and E^{I_2} represent the total energies of adsorbate-substrate, substrate and isolated adsorbate, respectively.

3.3. Results and discussion

3.3.1. Characterizations

Figure 3.3 shows the unique fluffy interconnected nanosheet frameworks with loose and layered features as observed for the NC-900 sample. Similar features can be found for other NC-*x* samples (**Figures 3.4a-d**), which means that annealing temperature has little effect on the morphology. Moreover, the preparation strategy can be also generally applied to obtain similar carbon-based nanosheets from different precursors with more details shown in **Figures 3.4e,f.** The TEM images of the NC-900 presented in **Figures 3.5a,b** exhibit the micropore-dominated nanosheet structure, which is also consistent with the results of SEM images depicted above. Besides, the high-resolution TEM (HR-TEM) image of NC-900 sample shows abundant micropore channels uniformly distributed throughout the sample with no clear lattice fringe,

further indicating its amorphous feature (**Figure 3.5c**). Additionally, the scanning transmission electron microscopy (STEM) image of the NC-900 sample gives evidence of the coexistence and homogeneous distribution of C, N, and O elements in the sample shown in **Figure 3.5d**. These loose carbon frameworks composed of the nitrogen-doped carbon nanosheets in the NC-*x* samples are expected to provide efficient charge storage ability for the redox electrolyte system.

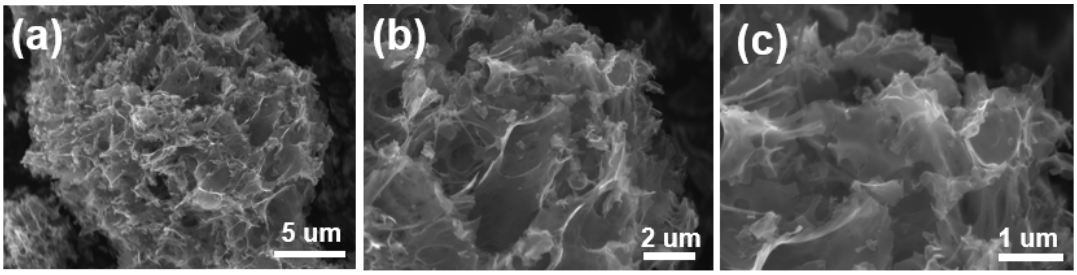

Figure 3.3 (a-c) FE-SEM and images of the NC-900 sample.

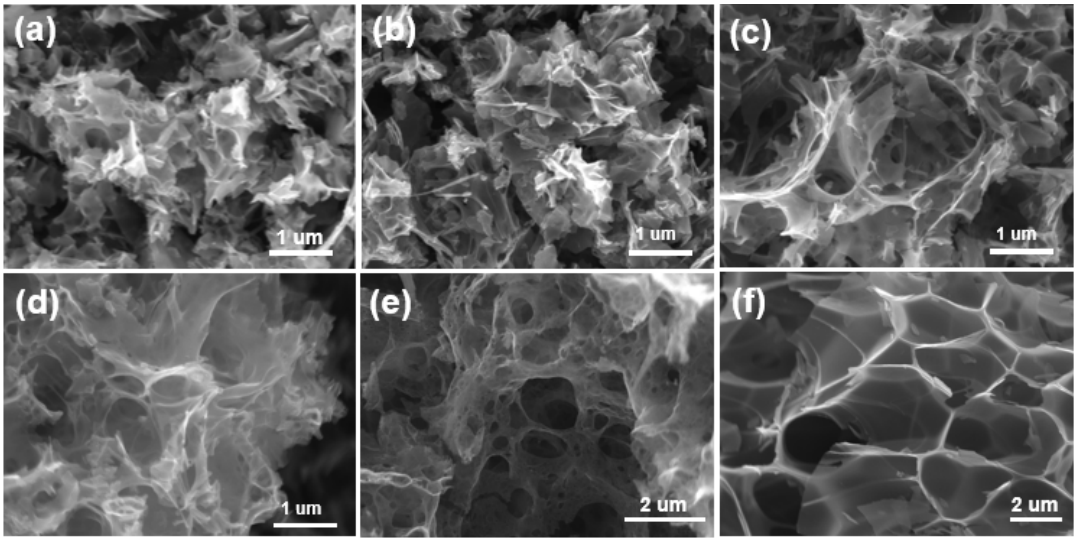

Figure 3.4 FE-SEM images of (a) the NC-600 sample, (b) the NC-700 sample, (c) the NC-800 sample, (d) the NC-1000 sample, (e) the PVA-derived carbon nanosheets and (f) the PVP-derived carbon nanosheets.

The powder X-ray diffraction (XRD) and Raman spectra were employed for the structural characterizations of the as-prepared samples. The two distinctive and broad peaks at 24° and 44° can be assigned to the (002) and (100) interlayer reflections respectively, confirming their amorphous structures (**Figure 3.6a**).[149] Additionally, the higher peak intensity and reduced peak broadening at about 44° suggest a more conjugated graphitic structure appeared as the carbonization temperature increases

from 600°C to 1000 °C. The Raman spectra of the as-prepared samples exhibit the intensity of D and G peaks associated with the disorder and crystalline graphite located at 1,350 cm^{-1} and 1,590 cm^{-1}, respectively, as shown in **Figure 3.6b**. The ratios of the intensity of D to G peaks are shown in **Figure 3.6c** in relation to the carbonization temperature. It is clear that there are similar defect levels for various as-prepared NC-*x* samples.

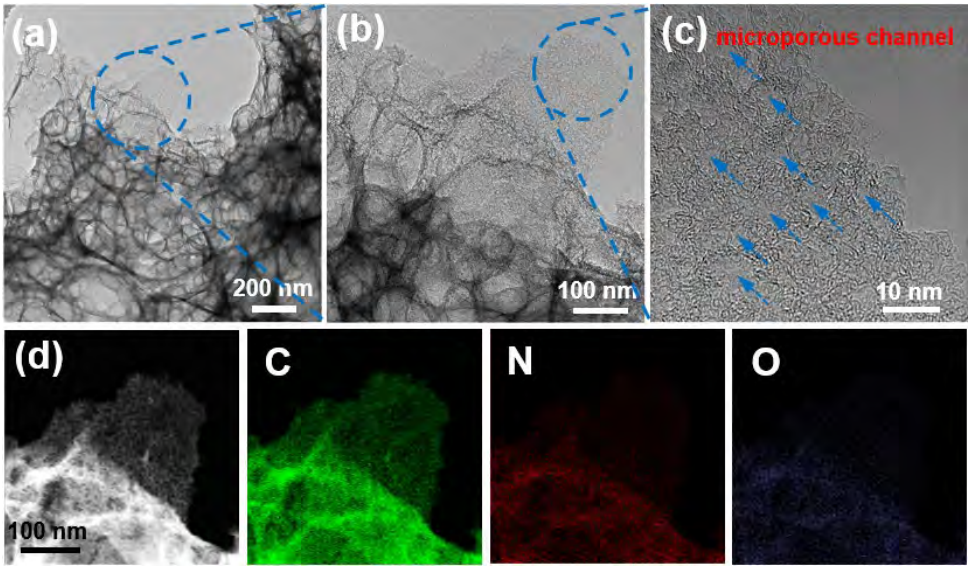

Figure 3.5 (a-c) TEM images of the NC-900 sample. (d) STEM image and corresponding elemental mapping of the NC-900 sample.

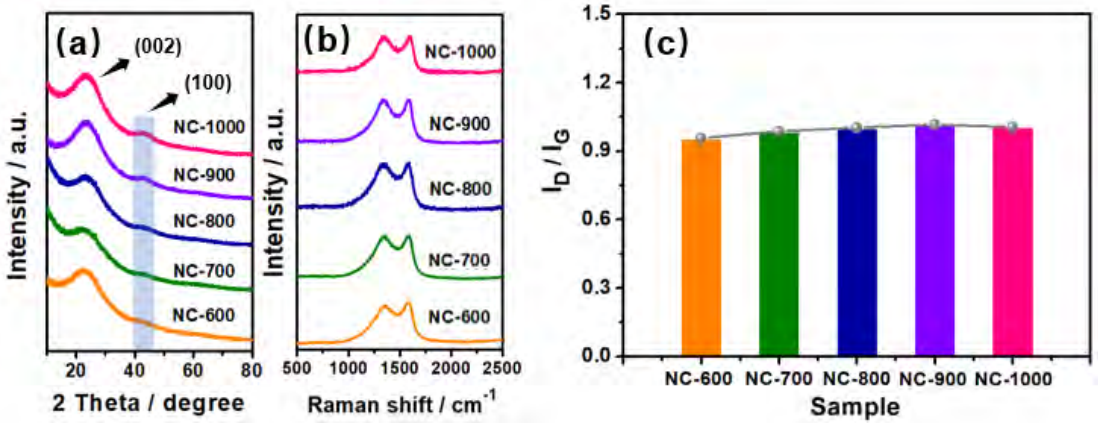

Figure 3.6 (a) XRD patterns and (b) Raman spectra of the as-prepared NC-*x* samples, and (c) the corresponding calculated I_D/I_G ratios of D and G peaks.

Furthermore, the surface chemical states of the NC-*x* samples were analyzed by X-ray photoelectron spectroscopy (XPS). The overall survey spectra are shown in **Figure 3.7a**. The presence of C, N, and O elements indicates the successful formation

of the N-doped configurations on carbon scaffolds, while a perceptible declining tendency of nitrogen content is attributed to the excessive loss of nitrogen species at the high annealing temperature. The C 1s curve can be split up into three separate peaks located at 248.6, 285.8, and 287.0 eV, corresponding to the C-C, C-O/C-N, and C=O groups, respectively (**Figure 3.7b**).[150] The high-resolution N 1s spectrum is deconvoluted into four subpeaks, namely, pyridine N (398.5 eV), pyrrole N (400.0 eV), graphitic N (401.1 eV), and pyridinic oxidized N (403.4 eV) as can be seen from **Figure 3.7c**.[150] It can be found that the thermal-induced composition evolution is clear as observed from the variations of various nitrogen species among these NC-*x* samples (**Figure 3.7d**). Although the total N content of the NC-800 sample is larger than that of the NC-1000, the contents of the graphitic N within these two samples are inverse on account of the higher graphitization degree for the NC-1000 sample. The various N-doping species have been considered to result in different delocalized "electron-donating areas", which can further influence the intrinsic conductivity and electrochemical activity of the electrode materials.[151] The nitrogen adsorption/desorption measurement was further conducted to evaluate the specific surface area and pore size distributions among all the samples. As shown in **Figure 3.8a**, type I then followed with type IV adsorption-desorption isotherms are exhibited for all the samples, evidenced by an abrupt adsorption plateau in the low relative-pressure region ($P/P_o < 0.4$) and hysteresis loops at high P/P_o region of 0.4-1.0, respectively.[152] The corresponding specific surface area and micropore volumes have a continuous increase with the carbonization temperature from 600 to 900°C (**Figures 3.8b**), which is caused by higher degree of carbonization and more sublimation of Zn particles. However, the excessive decomposition of precursor may lead to serious structural collapse, resulting in slight decrease in the SSA and pore volume for NC-1000 sample. In addition, the high SSA value of NC-900 sample is also derived from high micropore volume inside the sample (**Figure 3.8c**). Based on the comprehensive investigation of NC-*x* samples, the two key differences observed from nitrogen configurations and porosity characteristics make it achievable to reveal insights towards the congruent relationship between redox chemistry of electrolyte and carbon surface states.

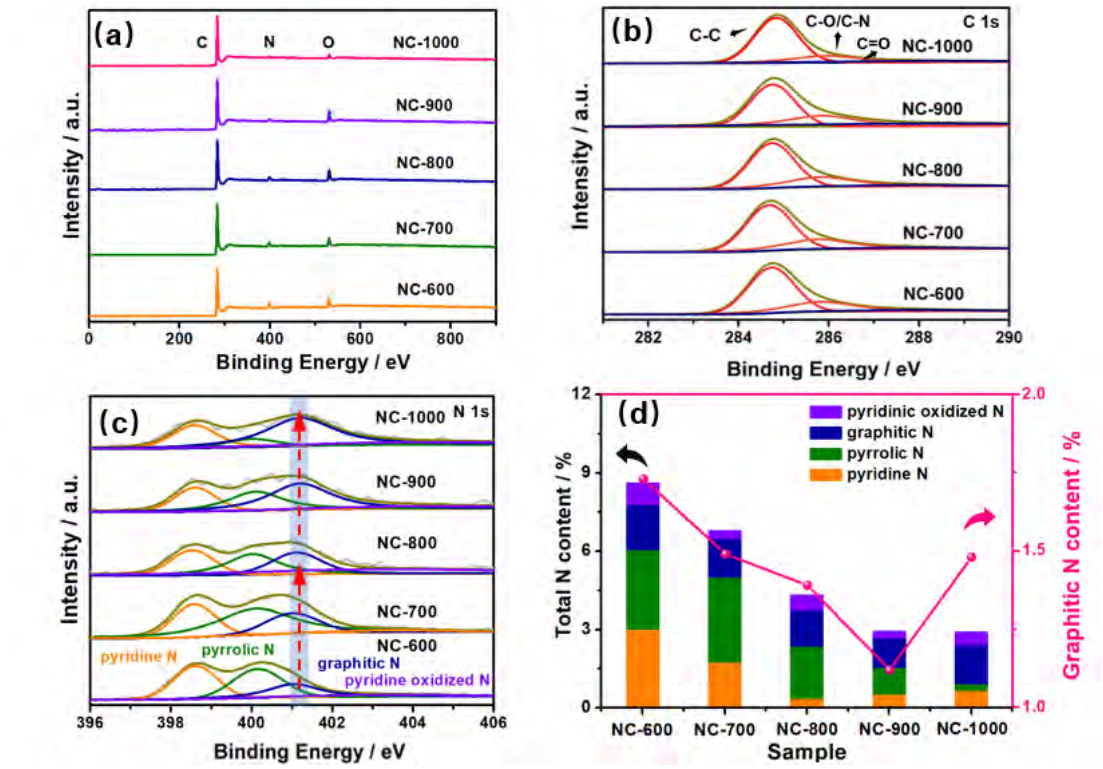

Figure 3.7 (a) XPS survey spectra and (b) High-resolution C 1s spectra of the as-made NC-*x* samples**.** (c) High-resolution N 1s spectra of the NC-*x* samples and (d) various nitrogen species contents.

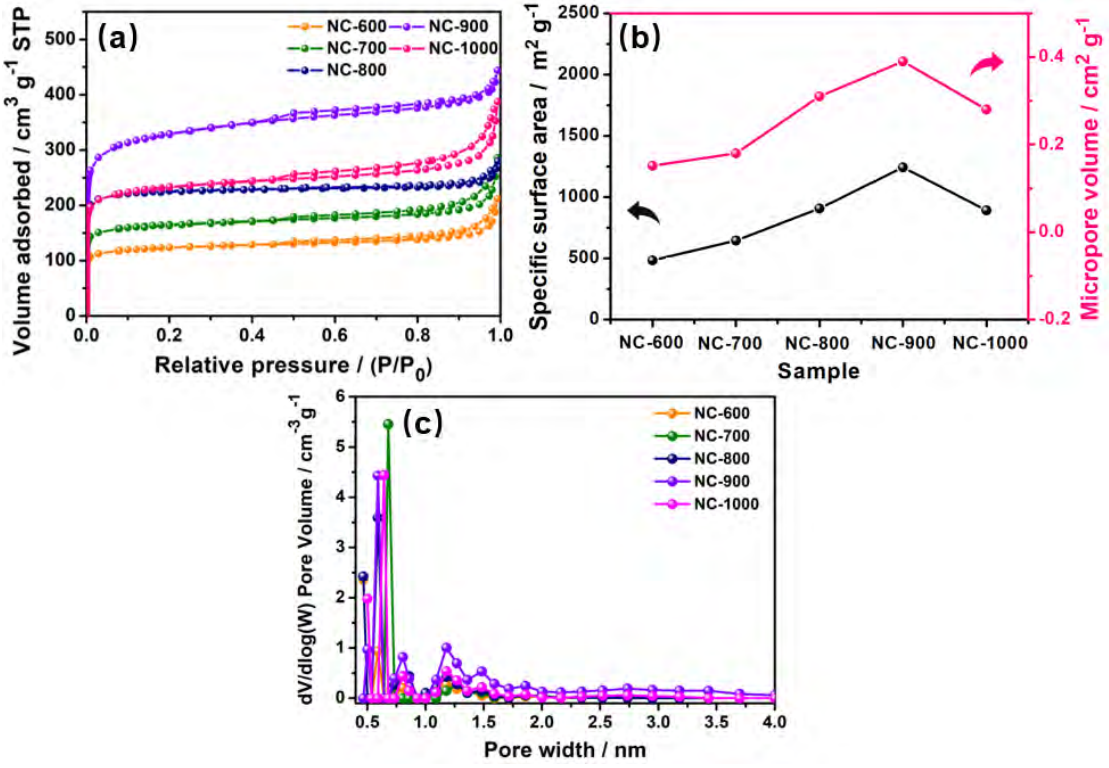

Figure 3.8 (a) Nitrogen adsorption-desorption isotherms, (b) Specific surface areas and pore volumes and (c) pore size distribution of the as-made NC-*x* samples.

3.3.2. Electrochemical performance

The electrochemical performances of NC-*x* samples were systematically investigated in two-electrode NC-*x*//NC-*x* symmetric devices, as illustrated in **Figure 3.9a**. Firstly, a common 2 M Na_2SO_4 solution was selected as the aqueous electrolyte to evaluate the electrochemical performance of NC-*x* samples**. Figure 3.9b** displays the cyclic voltammetry (CV) curves with a voltage window of 0-1.6 V. It can be seen that the surrounding rectangular area is dominated by electric double layer capacitance (EDLC). The weak redox peaks at about 0.1 V indicate the existence of a slight pseudocapacitance effect derived from nitrogen species.[153]

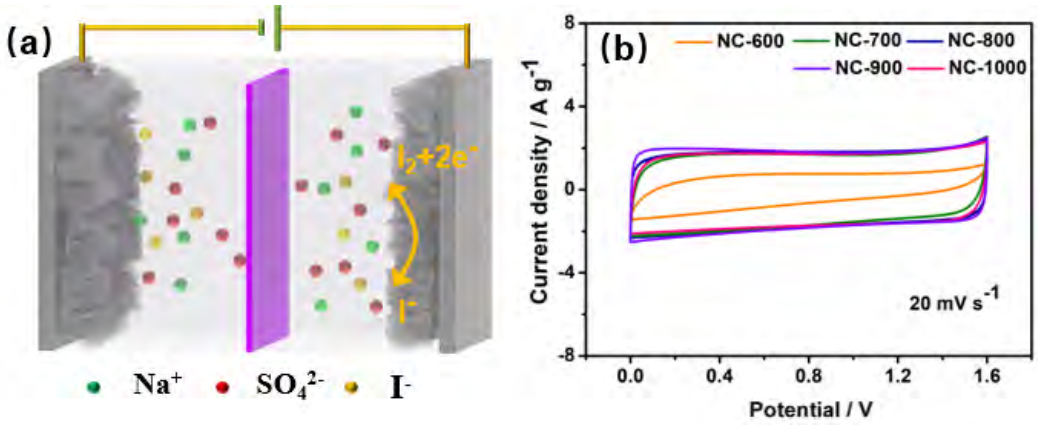

Figure 3.9 (a) Schematic illustration of two-electrode NC-*x*//NC-*x* symmetric supercapacitor with the aqueous redox electrolyte made of 2 M Na_2SO_4 and 0.05 M KI, in which the reversible iodide redox process mainly occurs in the positive electrode. (b) CV curves of as-made NC-*x* samples at 20 mV s^{-1} using 2 M Na_2SO_4 electrolyte.

The detailed CV and galvanostatic charge-discharge (GCD) curves of various samples are available in **Figure 3.10**. It can be seen from the CV results that more obvious distortion curves of NC-600 and NC-700 electrodes appear at high scan rate of 200 mV s^{-1}, indicating their poor rate capabilities compared with NC-800, NC-900 and NC-1000 electrodes, owing to their low specific surface areas with resulted fewer active sites for ions. Additionally, NC-600 shows non-straight curve of GCD results compared with others as exhibited in **Figure 3.10b**, which can be attributed to the pseudocapacitance derived from its high nitrogen content. Considering the calculated

capacitances from GCD results, the NC-900 electrode exhibits the best electrochemical performance with a specific capacitance of 92 F g^{-1} at a current density of 0.5 A g^{-1} followed with NC-800, NC-1000, NC-700, and NC-600. Such a trend is directly related to the porosity of the samples as seen from **Figure 3.11**.

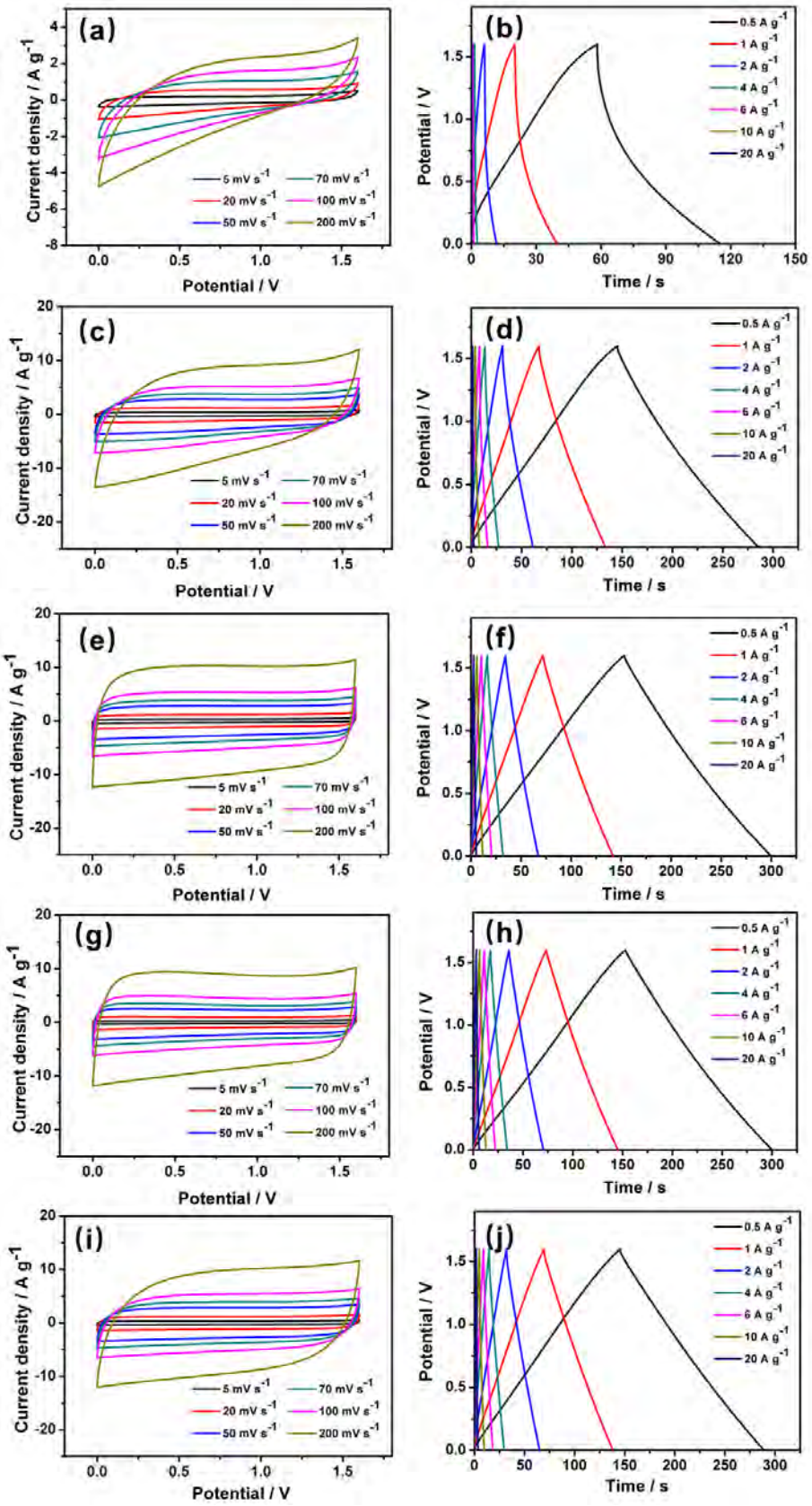

Figure 3.10 CV curves and GCD curves of (a,b) NC-600 sample, (c,d) NC-700 sample, (e,f) NC-800 sample, (g,h) NC-900 sample, (i,j) NC-1000 sample using 2 M Na_2SO_4 electrolyte.

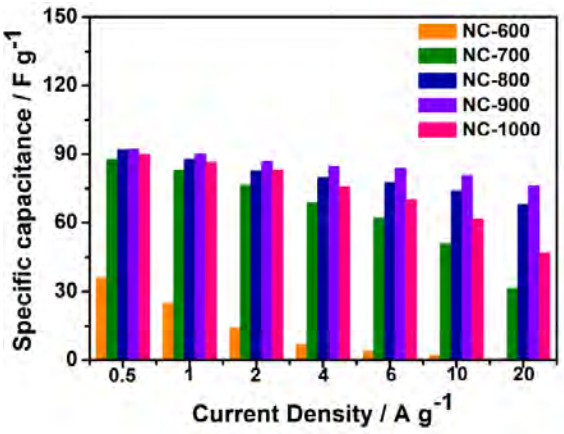

Figure 3.11 The specific capacitance of as-made NC-*x* samples using 2 M Na_2SO_4 electrolyte at different current densities.

It is important to note here that the two-electrode devices made of the same NC-*x* samples but assembled using the redox electrolyte (2 M Na_2SO_4 with 0.05 M KI), show much different corresponding CV curves at the same scan rate as shown in **Figure 3.12a**. As expected, the NC-900 electrode exhibits the largest quasi-rectangle area among the samples, corresponding to the largest specific capacitance of 145 F g^{-1} at 20 mV s^{-1}. Notably, there is a wide oxidation peak located at around 1.0 V in the forward scan and a reduction peak occurs at 1.2 V in the subsequent converse sweep for NC-600 sample. There is also slight shifts of oxidation and reduction peaks with the increase of temperature, indicating the redox reactions of the I^-/I_3^- couple occurring in the positive electrode which will be discussed detailly later.[154, 155] The detailed GCD curves of NC-900 sample are displayed in **Figure 3.12b.**

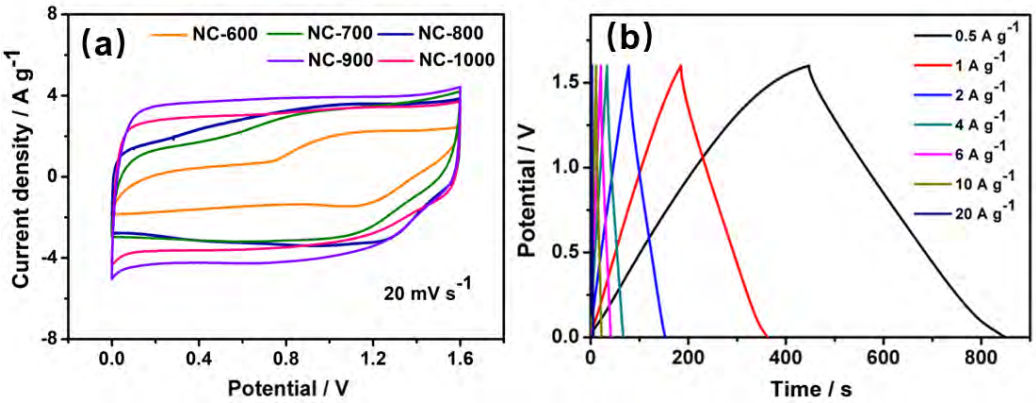

Figure 3.12 (a) CV curves of the NC-*x* samples at 20 mV s^{-1} and (b) GCD curves of the NC-900 electrode at different current densities using 2 M Na_2SO_4 and 0.05 M KI electrolytes.

The detailed CV and GCD curves of as-made NC-*x* samples in 2 M Na_2SO_4 and 0.05 M KI electrolyte are presented in **Figure 3.13**. From the CV curves of NC-600 and NC-700 electrodes, it can be observed that larger distortion of curve appears compared to the other electrodes with the increasing of scan rate from 5 to 200 mV s^{-1}, indicating the poor rate performances of NC-600 and NC-700 electrode in the redox electrolyte. Thus, the NC-600 and NC-700 electrodes with high nitrogen contents and low specific surface areas exhibit worse performance in both 2 M Na_2SO_4 electrolyte with or without addition of 0.05 M KI compared with others. The specific surface area can be regarded as the indicator to influence the intrinsic active sites inside the bulk structure of electrodes, which can provide ample channels and sites for the diffusion and adsorption of ions. Additionally, high nitrogen content cannot lead to a better electrochemical performance in redox electrolyte, demonstrating the total nitrogen content cannot promise the better electrochemical performance from the synergy with redox species. Further, it can be also concluded that the redox reaction of iodide species from the electrolyte occurs at the positive sites, confirmed by the abrupt change of CV curve of NC-600 electrode in **Figure 3.13a** at around 0.8 V compared to **Figure 3.10a**. The similar differences of CV curves of other NC-*x* electrodes also verify the conclusion above. Therefore, the capacitance change for the positive site is the main research emphasis in this research. The detailed experiments and analysis are provided in the subsequent part.

For the GCD curves of NC-600 electrode in **Figure 3.10b** and **Figure 3.13b**, there is an inflection point at around 0.8 V, which can be attributed to the redox reaction occurs as discussed for the CV curves. In addition, the straighter discharge cure in **Figure 3.13b** further emphasizes the influence of pseudocapacitance derived from iodide species, and the resulted longer discharge time validates the larger capacitance of NC-600 in the redox electrolyte. Moreover, all the obtained GCD curves of as-made electrodes exhibit slight distortion to some degree in the redox electrolyte compared with 2 M Na_2SO_4 electrolyte, meaning the successful enrollment of iodide species to increase the capacitance of electrodes. The detailed values and differences with or without redox species are summarized and discussed in the subsequent part.

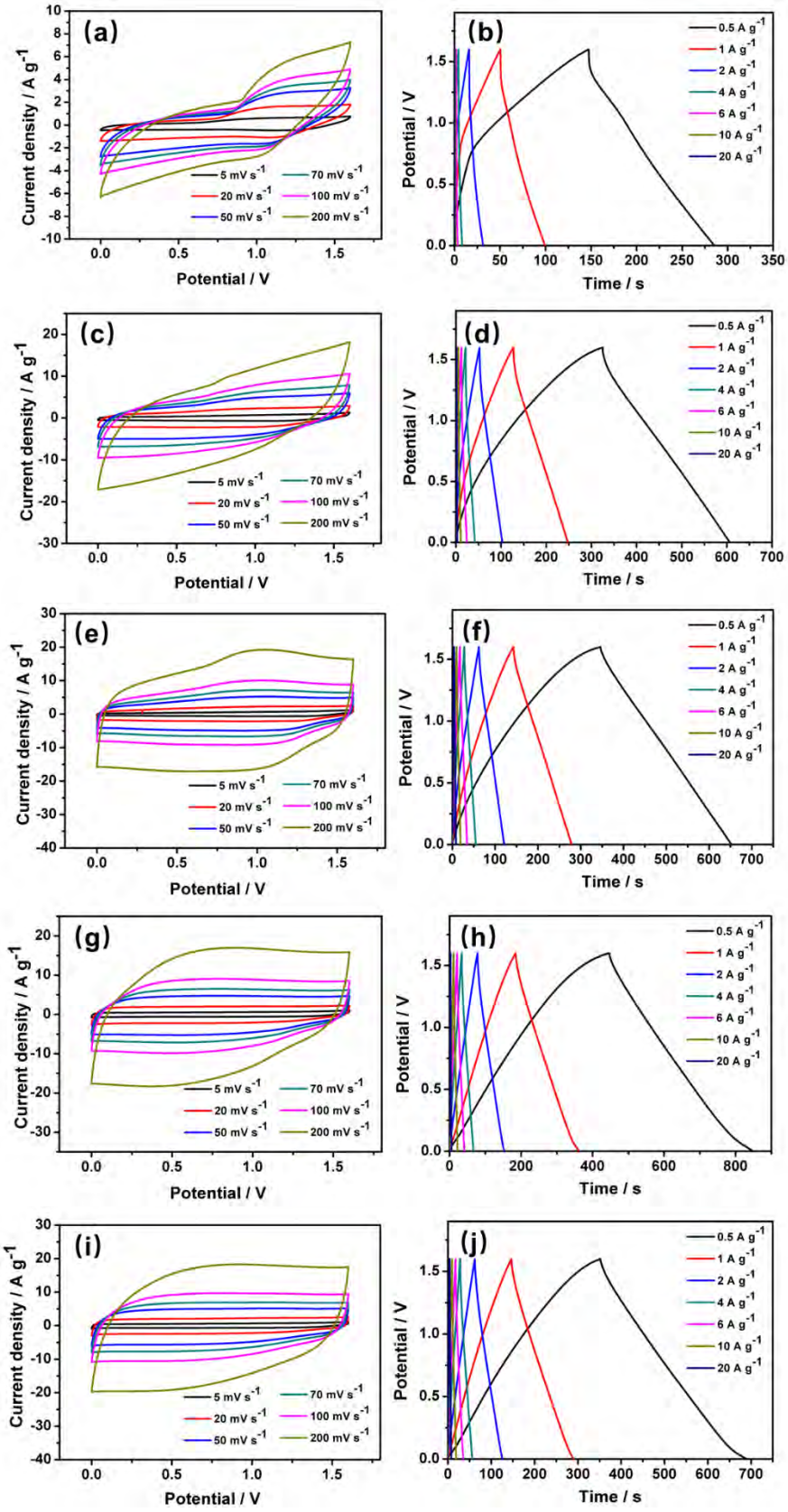

Figure 3.13 CV curves and GCD curves of (a,b) NC-600 sample, (c,d) NC-700 sample, (e,f) NC-800 sample, (g,h) NC-900 sample, (i,j) NC-1000 sample using 2 M Na_2SO_4 and 0.05 M KI electrolyte.

The corresponding specific capacitances are calculated and presented in **Figure 3.14a**. The NC-900 electrode displays the specific capacitance of 251 F g^{-1} at 0.5 A g^{-1}, increased by 173% compared with the control 2 M Na_2SO_4 electrolyte. This implies that the charge storage capacity of the NC-*x* electrodes is mainly assigned to the contribution of the porosity characteristics of the electrode combined with the redox reaction of the I^-/I_3^- couple. However, it is interesting to note that the NC-1000 electrode exhibits a higher specific capacitance of 211 F g^{-1} at 0.5 A g^{-1} than 191 F g^{-1} of the NC-800 electrode, which is different from the results using only 2 M Na_2SO_4 electrolyte without redox-active additives. Therefore, it can be inferred that the redox chemistry of the electrolyte at the electrode interface is also affected by the surface properties of carbon electrodes from nitrogen species in addition to its porosity characteristics. More detailed discussion on this aspect will be given subsequently. The Ragone-plots of the as-assembled devices using the two electrolytes are presented in **Figure 3.14b**. The feature of the microstructure here can be regarded as the main descriptor towards the electrochemical performance of electrodes in the aqueous electrolyte. The NC-900 sample exhibits the energy density of 22.4 Wh kg^{-1} at a power density of 400 W kg^{-1}, which are higher than the values reported by others using various redox species.[156-165] Furthermore, the as-assembled supercapacitor presents an excellent cycling stability with 96.5% capacitance retention after continuous charge and discharge cycling for 30,000 times at 6 A g^{-1} (**Figure 3.14c**).

To accurately clarify the underlying relationship between the redox chemistry of electrolytes and properties of carbon material surfaces, the rate capabilities of NC-*x* samples were investigated based on the results above (**Figure 3.11** and **Figure 3.14a**). The results are presented in **Figure 3.15a**. It can be found that the rates of all the NC-*x* samples exhibit decreasing tendency in redox electrolyte, although the overall capacitive values of NC-*x* samples are larger than that of control electrolyte at each current density as discussed above (**Figure 3.11** and **Figure 3.14a)**. Interestingly, the magnitudes of the declines from 52% to 47%, i.e. 5% for NC-1000 sample are the smallest, followed by NC-700, NC-800, and NC-900 samples with the approximate level of 13%, 20%, and 38%, respectively, implying the accelerated redox reaction of I^-/I_3^- couple taking place within the NC-1000 sample. It also should be noted that the SSA and pore volume of NC-1000 electrode are not the largest among all samples. Thus, another parameter derived from surface properties of carbon materials governed by nitrogen site configurations is expected to play the leading role influencing the redox

activity of I^-/I_3^- species. To elucidate the real electrochemical process at each NC-*x* electrode in the two-electrode symmetric device, a reference electrode was introduced in the test system. The corresponding CV curves of the NC-900//NC-900 symmetric supercapacitor and the positive and negative electrodes are shown in **Figure 3.15b** at a scan rate of 20 mV s^{-1}. More such CV curves for other samples are available in **Figure 3.16.** It is clear that the redox reaction of I^-/I_3^- couple mainly occurs at the positive electrode, which also verified by the equilibrium voltage shifts of the positive electrodes for the symmetric devices. Thus, the differential capacitance ($\Delta F\ g^{-1}$) value of the positive electrode in the redox and control aqueous electrolytes should be a critical variable to explore the effect of carbon surface on the redox chemistry of I^-/I_3^-.

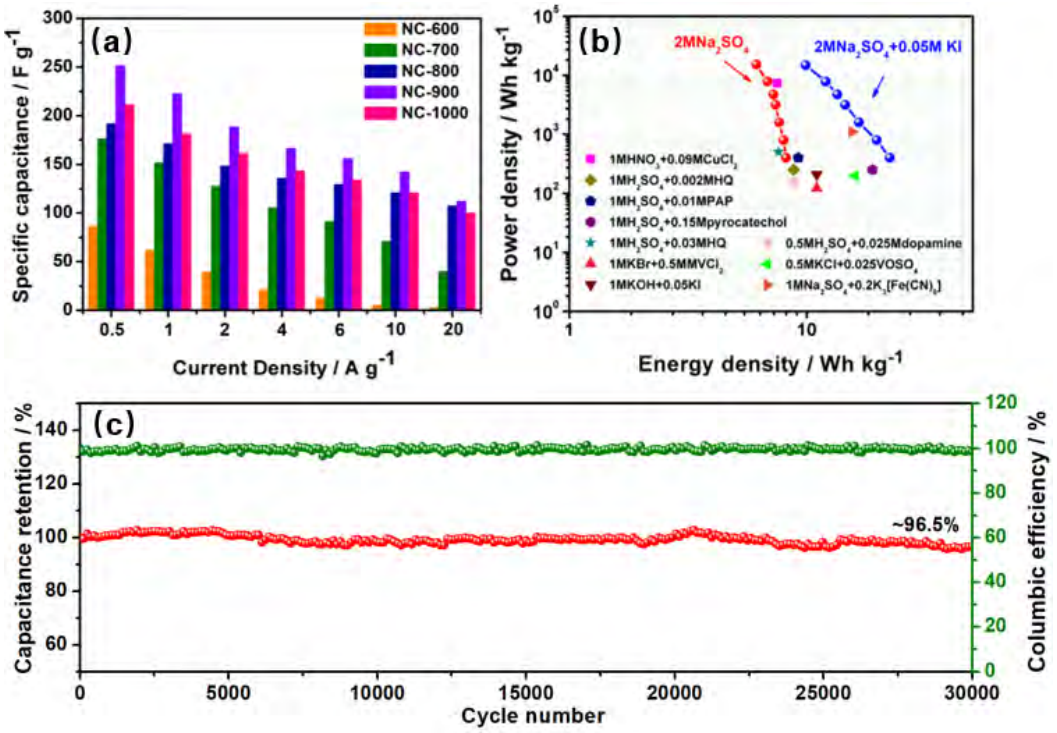

Figure 3.14 (a) The corresponding specific capacitance of as-made NC-*x* samples and (b) Ragone plots of the NC-900//NC-900 symmetric supercapacitors with and without redox-active additives and comparison of energy and power density values with the previous literature. (c) Cycling stability of the NC-900//NC-900 symmetric supercapacitors using 2 M Na_2SO_4 and 0.05 M KI electrolyte at 6 A g^{-1}.

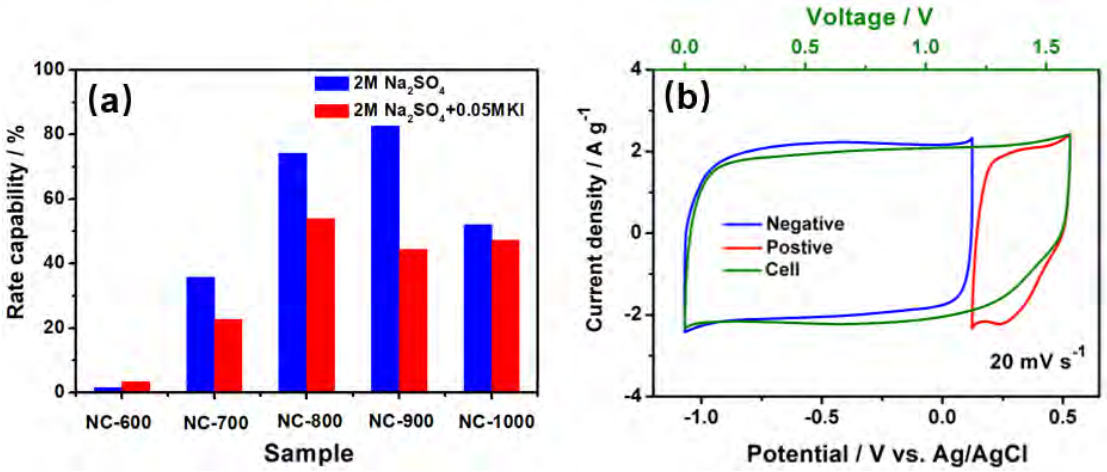

Figure 3.15 (a) Rate capabilities of the as-made NC-*x*//NC-*x* symmetric supercapacitors with and without redox-active electrolytes. (b) CV curves of the NC-900//NC-900 symmetric supercapacitor and the positive and negative electrodes at a scan rate of 20 mV s^{-1}.

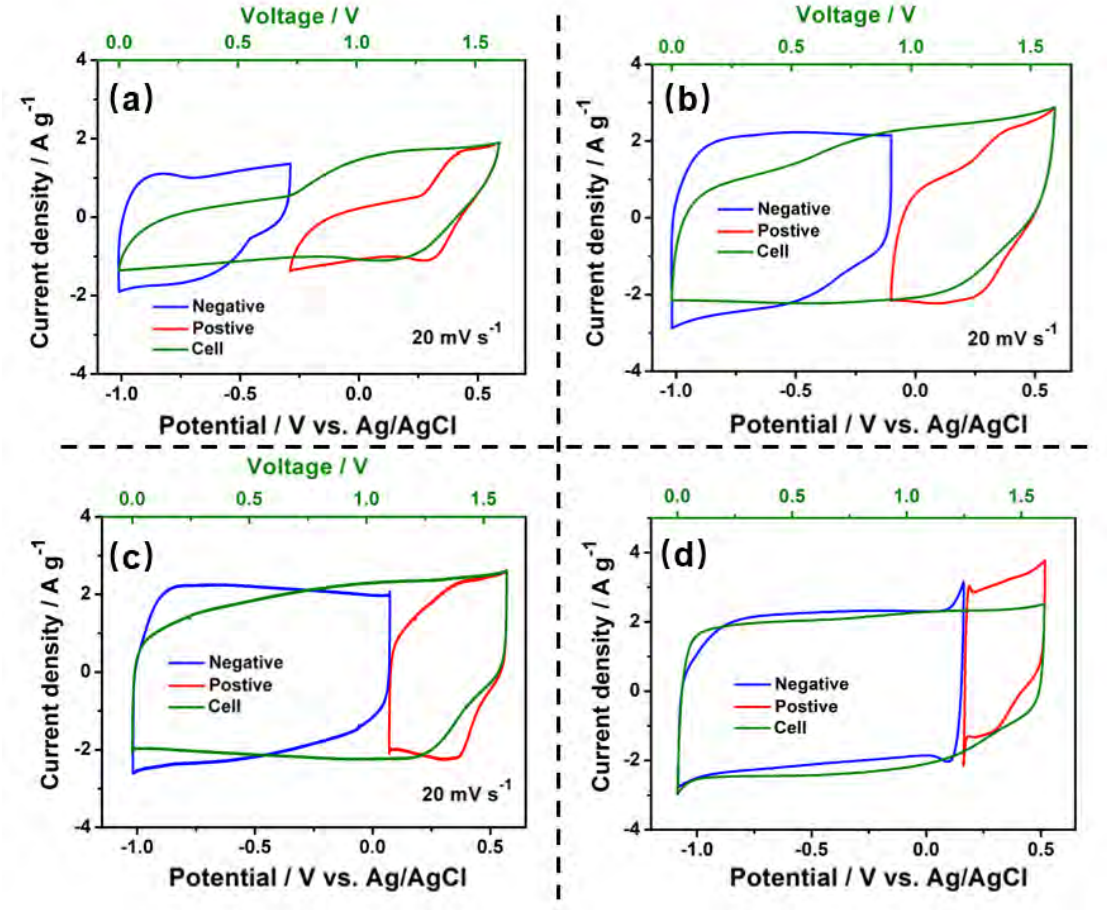

Figure 3.16 CV curves of the positive and negative electrodes at a scan rate of 20 mV s^{-1} of (a) the NC-600//NC-600 symmetric supercapacitor, (b) the NC-700//NC-700 symmetric supercapacitor, (c) the NC-800//NC-800 symmetric supercapacitor, (d) the NC-1000//NC-1000 symmetric supercapacitor.

Moreover, to eliminate the influence of microstructure factors, the differential capacitance is normalized by SSA ($\Delta F\ g^{-1}/m^2\ g^{-1}$, $\Delta F/m^2$) before correlating with nitrogen site configurations including pyrrole N, pyridine N, and graphitic N, as shown in **Figures 3.17a,b**, It can be found that the differential capacitances from redox reaction of I^-/I_3^- species cannot match well with the contents of pyrrole N or pyridine N configurations with untrustworthy values of R^2 (< 0.71), but it can be regarded as linearly correlated with the graphite N content which has a high value of R^2 up to 0.91. In addition, the differential capacitance is also mismatched with total N and C contents as shown in **Figures 3.17c,d**, which exhibit a R^2 value of 0.68 and 0.41. Interestingly, it shows a nearly linear relationship with the total N content for the NC-*x* samples below 1000 ^oC. There is a huge increase of differential capacitance appeared for the NC-1000 sample, which is in agreement with the tendency of the graphitic N content shown in **Figure 3.7d**, indicating the unique function of graphitic N within the carbon frameworks. For instance, although the total N content of the NC-1000 electrode is the lowest among NC-*x* electrodes, it can still realize a high capacitive contribution from redox species due to its high graphitic N content. In other words, the graphite N configuration on the carbon scaffolds plays a vital role in accelerating redox kinetics of I^-/I_3^- species, thus enabling superior rate capability of carbon electrodes. Additionally, it is also noted that the NC-900 electrode has a low ratio of graphitic N to total N content, but it still exhibits the highest specific capacitance, indicating the major impact of porosity characteristics for EDLC within the electrodes.

With the discussion above, one would agree that the graphitic N configuration can accelerate the redox reaction that occurred in the positive electrode. Meanwhile, the high SSA of the electrodes provides ample adsorption sites for electrolyte ions to further enhance the overall electrochemical performance of the supercapacitor. Therefore, the synergistic effect of porosity characteristics and the content of graphitic N configuration is crucial for enhancing the electrochemical performance of carbon-based electrodes in iodide redox electrolytes.

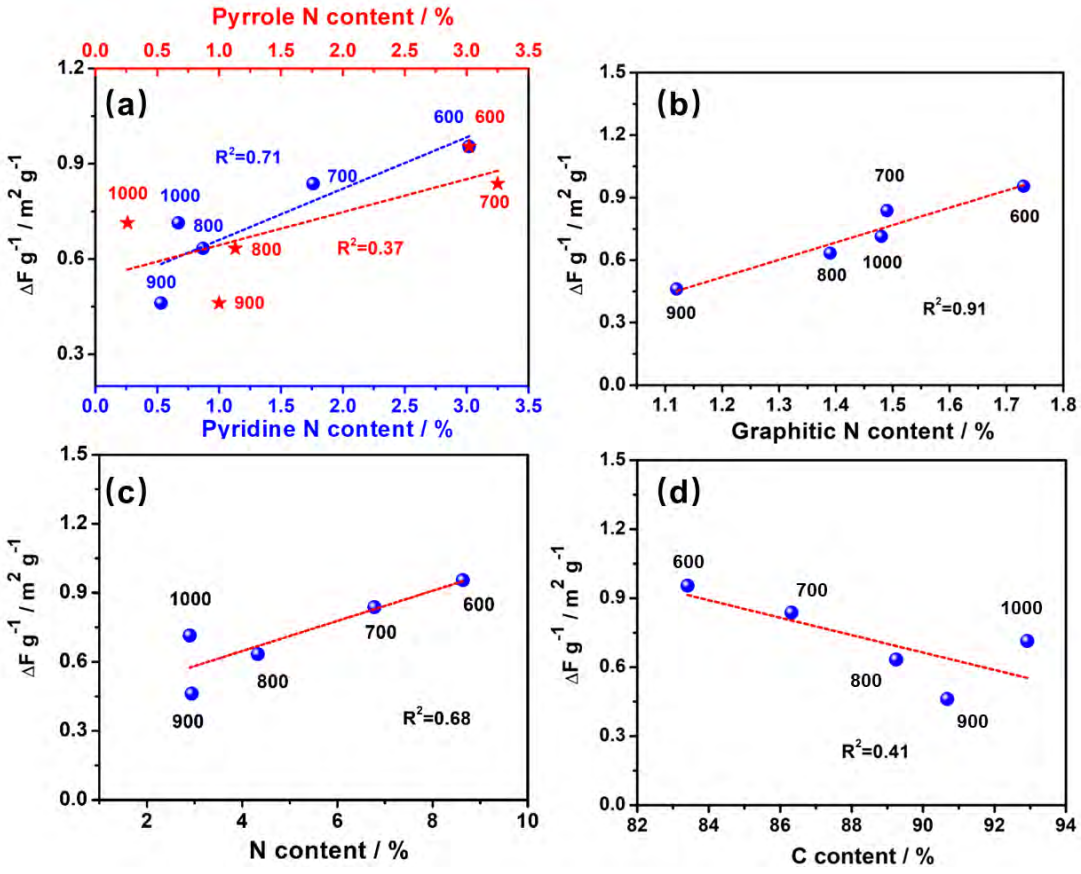

Figure 3.17 Relationship of differential capacitance normalized by SSA with (a) pyrrole N, pyridine N, (b) graphitic N, (c) N and (d) C contents based on the symmetric supercapacitor in redox electrolyte**.**

3.3.3. First-principles calculations

A theoretical investigation employing density functional theory (DFT) was conducted to further explore the N-doping effect on the redox chemistry of carbon-based electrodes. The redox reaction mechanism of the I^-/I_3^- species has been described in literature ($2I^- \leftrightarrow I_2 + 2e^-$; $I_2 + I^- \leftrightarrow I_3^-$).[166] The whole redox reaction involves a two-electron process from I^- to I_2, followed by the fast spontaneous transformation from I_2 into highly soluble I_3^- and finally reaching equilibrium, so that the iodide redox reaction is determined by $2I^- \leftrightarrow I_2 + 2e^-$. Therefore, the pristine graphene and other three type N-doped graphene models adsorbed with I atom (I^*) or I_2 molecule are optimized. The resulting models and adsorption energies of the I^* and I_2 are displayed in **Figure 3.18 and Figures 3.19a,b**. It can be found that the graphitic N configuration leads to the largest adsorption energy toward I^* and I_2 in comparison to other nitrogen

configurations. Besides, the optimized I-I distances on graphene, pyridine N, and pyrrole N sites are similar (2.68~2.69 Å) while the value is stretched to 3.07 Å for graphitic N, indicating that the activation of I_2 species is more feasible on graphitic N configuration. Similar conclusions can be further made by the electron density differences shown in **Figure 3.19c**, where the yellow and blue areas refer to the electron-rich and electron-deficient areas. From the top and side views, it can be found that the graphene, pyridine N, and pyrrole N sites exhibit similar bonding characteristics. As I_2 molecules are adsorbed onto the substrates, only a few C atoms contribute electrons to the C-I bonds among these configurations. However, the result is different for the graphitic N site, where many more C atoms cooperate and provide electrons to the I atom with no obvious p-orbital overlap from I and C atoms, thus creating a strong localization of electron density depletion around the adsorption sites. These results demonstrate that the graphitic N configuration has much potential on electron-donating characteristics and further accelerates the redox reaction of I^-/I_3^-. Therefore, based on the experimental and theoretical analyses, it can be concluded that a high ratio of graphitic N is not only beneficial for adsorbing I_2 and I* but also able to enhance the redox kinetics of I^-/I_3^- in the aqueous electrolyte.

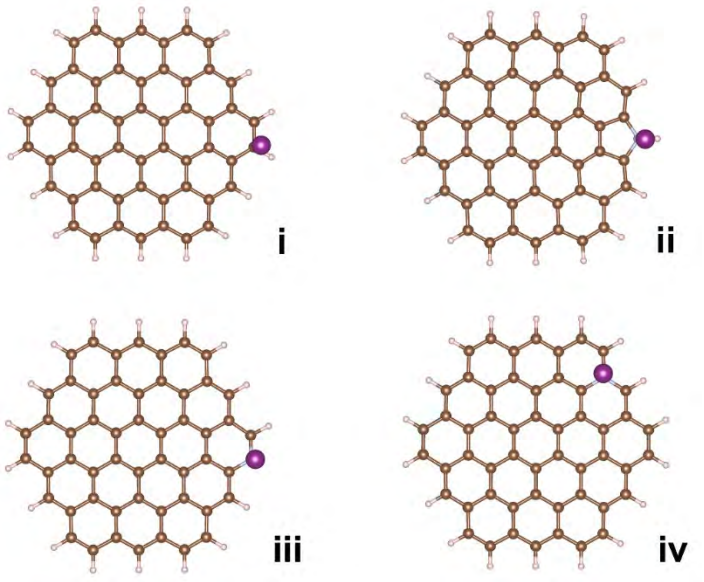

Figure 3.18 Optimized structure of I* absorbed onto various substrates.

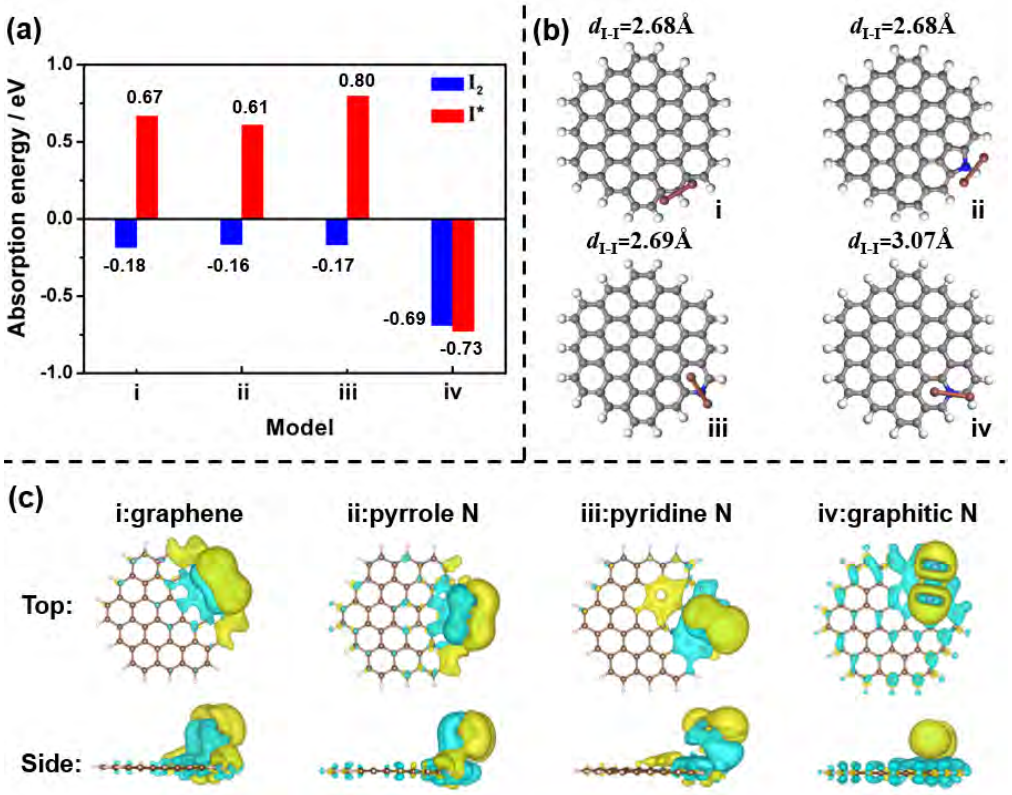

Figure 3.19 (a) Adsorption energies for I^* and I_2 on various configuration models, where the asterisk (*) stands for the adsorbed I atom. (b) Optimized structure of I_2 molecule adsorbed on the various configuration models. (c) Top and side views of the charge densities of I_2 molecule absorbed on various configuration models.

3.4. Summary

In summary, a facile and general strategy was developed for the fabrication of two-dimensional nitrogen-doped porous carbon nanosheets, serving as the demos to detect the relationship between redox chemistry of electrolyte and property of carbon surface. The ample micropore-dominated structure within all the NC-*x* samples provides the large electrode/electrolyte interfacial contact area, which enables abundant adsorption sites for charge storage. Impressively, the experimental and theoretical results confirm that the graphitic N content on the carbon scaffolds plays a vital role in accelerating the redox kinetics of the I^-/I_3^- couple in the aqueous electrolyte, thus enabling excellent rate capability of carbon-based electrodes. The N-doped carbon prepared at 900 ^oC annellation exhibit the highest energy and power densities of 22.4 Wh kg^{-1} and 15.2 kW kg^{-1} using redox electrolyte (2 M Na_2SO_4 and 0.05 M KI), as well as excellent stability of 96.5% capacitance retention after 30,000 charging/discharging cycles. This work provides a novel approach and insight for the design and fabrication of carbon material with optimal structure and composition for high-performance supercapacitor using the aqueous redox electrolyte.

Chapter 4 Enhanced Rate and Cycling Performance for Aqueous Hybrid Supercapacitor by Ionically Permeable Polymer Skin on Nickel-Cobalt Hydroxide Nanosheets

4.1. Introduction

Aqueous supercapacitors (SCs), as emerging advanced high-efficiency energy-storage devices, have been extensively researched and developed in recent years by virtue of its high rate capability and excellent cycling stability.[167-169] However, the unsatisfactory energy density of aqueous SCs severely hinders their further applications.[170, 171] In particular, asymmetric design of SCs by utilizing two different charge storage mechanisms of electrodes, i.e. aqueous hybrid SCs are considered the promising candidates for efficient energy storage systems, in which the Faradic-type /pseudocapacitive materials and carbon materials are usually employed as positive and negative electrodes, respectively.[172-176] Such configuration can break the low energy density (E) limit by enlarging the working voltage (V) according to Equation (2-3). Especially, transition metal-based compounds are regarded as the most promising Faradic-type electrode materials owing to their high theoretical capacitances and excellent reliability.[177-179] It is generally accepted that efficient superposition of redox peaks can expand the charge storage region to store more charges, as evidenced by the typical electrochemical behavior of pseudocapacitive materials such as RuO_2, Fe_3O_4 or MnO_2 with EDLC-like voltammogram shape.[180-182] Thus, the exploration of electrode materials with bimetallic active sites is of great interest to realize high electrochemical performance derived from the overlapping of multiple variable valences. Particularly, recent advances mainly include bimetallic oxides (sulfides, hydroxides) and their composites, such as manganese cobalt oxide/nickel foam, zinc cobalt sulfides, nickel cobalt layered double hydroxides, and so on, as high-performance electrode materials for supercapacitors.[183-191] Given that most electrochemical reactions are governed by a potential difference or gradient which strongly influences the electric field distribution and current density inside the bulk structure of electrode material, the inherent low conductivity of active species and their limited contact areas with conductive substrates can result in charge accumulation at specific interface with unevenly distributed electric

potential along the bulk phase of active species.[192, 193] In such case, the corresponding rate capability and cycling performance of SCs are still lower than expected.

Interface engineering can be regarded as an effective strategy to mediate the ion diffusion pathway and maintain dimensional stability of host materials.[194-197] The charge redistribution at junction area can spontaneously generate a built-in electric field at the interface, resulting in enhanced charge transfer capability and excellent rate capability toward SCs.[198-200] As proved, the feasible processing and good chemical compatibility of conductive polymers (CPs) allow strong interface connectivity onto various electrode materials. Especially, poly(3,4-ethylenedioxythiophene) (PEDOT) is deemed as a promising conductive layer in view of its intrinsically ultrahigh electric conductivity (up to 1,000 S m^{-1}) and superior electrochemical cycling stability.[22, 92, 201] Further, PEDOT with high mechanical strength up to 10 MPa can alleviate the effects of the expansion and shrinkage of fragile structures of active materials, giving rise to an improved mechanical stability upon redox cycling.[202-204] For example, Jia *et al.* firstly fabricated MoS_2 nanobelts onto the carbon cloth substrate to obtain a flexible electrode, followed by electrochemical polymerization of 3,4-ethylenedioxythiophene (EDOT) molecules onto the surface of MoS_2 nanobelts.[205] The resulted electrode exhibits significantly enhanced capacitive performance in terms of areal capacitance, rate capability and cycling stability. However, the typical solution-based methods cannot keep the crystal structure of precursor intact, nor control the thickness and integrity of polymer layer precisely onto the substrate, causing unpredictable wetting and solution effects combined with intrinsic structure distortion. The oxidative chemical vapor deposition (oCVD) technique provides the means of modifying solid surfaces with controllable coatings of thin conductive polymer layer by introducing vapor phase oxidants and monomers.[206-209] Under such consideration, the research group previously developed an oCVD facility and fabricated PEDOT skin on layered metal oxide cathode materials with electronic and ionic conductivity, exhibiting enhanced capacity and thermal stability under high-voltage operation in lithium-ion batteries application.[210] Thus, it is of great opportunity by adopting oCVD technique to rationally regulate the distribution of electric potential among the surface of redox active species, along with the ion diffusion flux by leveling polarization, leading to enhanced electrochemical performance for SCs.

Herein, some NiCo layered double hydroxides (NiCoLDH) nanosheets are synthesized as redox species onto carbon fiber substrate (named simply as LDH) via

electrochemical deposition procedure, followed by the oCVD technique to build a highly ionically permeable and electronically conductive PEDOT skin in-situ onto the above LDH (named as LDH/PEDOT-*x*, with *x* standing for coating time in minutes). The fabrication strategy proposed here is the first time to utilize both electrodeposition and oCVD technology to fabricate PEDOT-coated LDH as electrode material for supercapacitor. By using multiple electrochemical tests combined with COMSOL multiphysics simulation and DFT theoretical analysis, it has been found that the conductive layer can induce more uniformly distributed potential along the surface of NiCoLDH nanosheet, further altering the reaction pathway of ions to facilitate energy storage process. Moreover, the presence of PEDOT skin can not only introduce a built-in electric field between the interface but also decrease the desorption energy of H atoms from NiCoLDH to accelerate the redox reaction with OH^- ions. As a result, the as-obtained LDH/PEDOT-*10* as electrode material can deliver a high rate capability (79% retention from 1 A g^{-1} to 50 A g^{-1}) and cycling stability (92% retention for 6,000 cycles at 10 A g^{-1}) compared to the LDH electrode material (55% retention from 1 A g^{-1} to 50 A g^{-1}, 70% retention for 6,000 cycles at 10 A g^{-1}). The assembled supercapacitor made of LDH/PEDOT-*10*//AC can deliver a high energy density up to 58 Wh kg^{-1}. These results offer a novel method and concept for the boost of electrochemical performance of transition metal-based electrode materials in the energy storage and related fields. More details are discussed subsequently.

4.2. Experimental section

4.2.1. Fabrication of NiCoLDH onto carbon fiber

Typically, the 1 cm x 2 cm carbon fiber (CF) was washed by 2 M HCl, absolute ethanol and deionized water for four times to remove the impurities from the surface. Then, $NiSO_4 \cdot 6H_2O$ (0.532 g, 0.02 M), $CoSO_4 \cdot 6H_2O$ (0.282 g, 0.01 M) and thiourea (0.761 g, 0.01 M) were mixed into 100 mL deionized water under ultrasonic treatment for 30 mins to obtain a uniform aqueous solution. After that, carbon fiber was immersed into the above solution and used as the working electrode, coupled with Pt electrode and calomel electrode as counter and reference electrode, respectively. Thereafter, nickel cobalt layer double hydroxides deposited onto carbon fiber can be obtained by

electrodeposition method for 15 mins under a constant voltage of -1 V. Finally, after typical washing with deionized water for three times and drying in an oven at 70 ^{o}C overnight, the electrode was made with mass loading of active material being about 1.1 mg based on the mass change of carbon fiber before and after above treatment.

4.2.2. Fabrication of PEDOT-coated LDH

The as-fabricated LDH was coated with a custom-built rotary oxidative chemical vapor deposition (oCVD) system and exposed to the vapors composited of 3,4-ethylenedioxythiophene monomer and vanadium trichloride oxide ($VOCl_3$) oxidant at flow rates of 2±0.2 and 0.2–0.3 sccm, respectively. The pressure of the reactor was controlled around 300 mTorr and the water bath was kept at 90 ^{o}C while the rotation rate was maintained around 150 r.p.m.[210] During this process, the step growth of polymer occurred based on the simultaneous introduction of monomers and $VOCl_3$ on the surface of as-made sample, as illustrated in **Figure 4.1a**. Thus, the thickness-controlled PEDOT-coated samples can be obtained by optimizing the polymerization time. After the oCVD process, the sample was rinsed with methanol for three times to remove the unreacted monomers and oxidant, followed by drying in a vacuum oven at 70 ^{o}C for 12 hours. The as-obtained samples are denoted respectively as LDH/PEDOT-*5*, LDH/PEDOT-*10* and LDH/PEDOT-*20*, with the number reflecting the coating time in minutes. After introducing PEDOT onto the surface of LDH, the mass loading of total active material increases from 1.1 mg (LDH) to 1.2 mg (LDH/PEDOT-*5*), 1.3 mg (LDH/PEDOT-*10*) and 1.6 mg (LDH/PEDOT-*20*), respectively. Further, the optimized PEDOT layer is considered to be beneficial for maintaining structural integrity, coupled with providing a fast transport pathway for electrons, as shown in **Figure 4.1b**.

4.2.3. Material characterization

Various techniques were employed to characterize the synthesized samples. X-ray diffraction (XRD) and Raman spectroscopy patterns were obtained to record the crystal structure information of as-obtained samples. Besides, X-ray photoelectron spectroscopy were employed to test the corresponding compositions of the as-obtained samples. Furthermore, the field-emission scanning electron microscopy (FE-SEM) and

transmission electron microscopy (TEM) were performed to observe the detailed morphologies of the prepared samples.

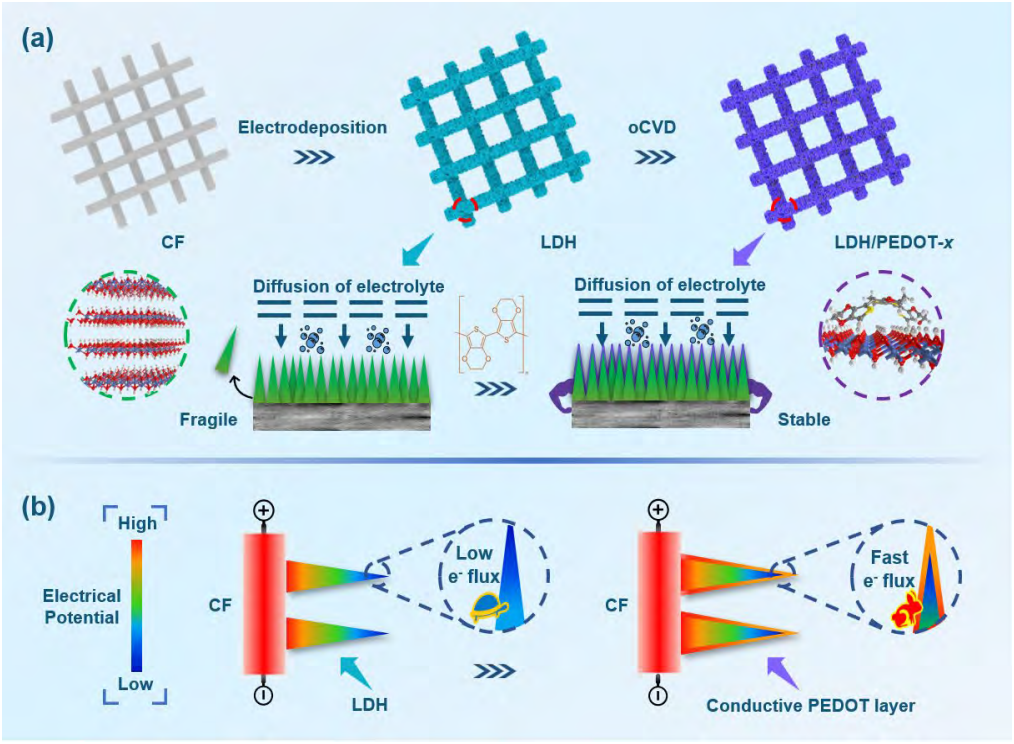

Figure 4.1 (a) The schematic illustration of the fabrication of LDH/PEDOT-*x*. (b) The comparison of electrical potential behavior of LDH with/without PEDOT layer.

4.2.4. Electrochemical characterization

The as-obtained samples were directly employed as working electrode materials and evaluated in 6 M KOH solution, using a typical three-electrode cell configured with a working electrode, a counter electrode (Pt foil), and reference electrodes (Calomel electrode). The Metrohm Autolab (NOVA) electrochemical workstation was used to perform the galvanostatic charge/discharge (GCD) measurements, cyclic voltammetry (CV) and electrochemical impedance spectroscopy (EIS). The cycling stability was tested by LANHE CT2001A instrument. Additionally, the asymmetric supercapacitor was assembled by employing activated carbon (AC) as the negative electrode, while the as-prepared samples and non-woven fabric were used as positive electrodes and membrane separator. The mass ratio of the positive and negative electrodes was estimated to be 1:2 based on the GCD results, so that the same amount of charge was

obtained on both sides in the electrochemical process ($Q^+=Q^-$). The corresponding performance was also investigated in 6 M KOH electrolyte.

4.2.5. Electrical field simulation

COMSOL Multiphysics 5.4 with an implemented finite element solver was applied in all physical field simulations in this work. "The Secondary Current Distribution" was used for the stimulation of model. The simulations of the ion flux distribution were conducted in a 1×1 μm^2 geometric model, as illustrated in **Figure 4.2**. For theoretical understanding of the unique role of the conductive PEODT layer, the triangle geometry (yellow part) represents the LDH material with weak conductivity (around 10^{-5} S cm^{-1}) and the surface chemical potential decreases linearly from bottom (0.5 V) to top (0 V) of LDH edge.[211, 212] On the contrary, PEDOT (black part) coated sample is assumed that the surface chemical potential (0.5 V) is constant along its surface of active electrode material because of the good conductivity of PEDOT (exceeding 1,000 S cm^{-1}).[22, 92] In this way, the influence of largely discrepant conductivity is manifested. For ionic conductivity constant of aqueous electrolyte, the typical value is at the level of 10 S m^{-1}.[213] The value decreases to the level of 10^{-1} S m^{-1} inside the polymer skin, which has been generally accepted and verified by the previous research.[202, 214, 215] Butler-Volmer expressions are used to describe the electrode reaction kinetics, and Nernst equations are used to calculate the equilibrium potentials. The anode and cathode surfaces are modeled using two Electrode Surface nodes, where the voltage of the electrode is thus the cell voltage. All other boundaries are isolated. Thus, the ionic current density represented by the green part can be obtained toward various models.

4.2.6. Theoretical calculation

All calculation was based on the density functional theory (DFT) performed in Vienna Ab-initio Simulation Package (VASP) and the spin-polarized Perdew-Burke-Ernzerhof (PBE) version of the generalized gradient approximation (GGA) was treated as the exchange-correlation functional, associated with the projector-augmented wave pseudopotential for electron-ion interaction.[138, 139, 212] The Grimme's zero damping

DFT-D3 method was further considered in view of the weak van der Waals dispersion forces between the adsorbates and the surfaces. The Monkhorst−Pack k-point sampling of 2 × 2 × 1 were selected for adsorption thermodynamics and density of state calculations, respectively.[147] For the calculations of total energy, a plane-wave kinetic cutoff energy of 400 eV was set to expand the valence electronic states. All atoms were optimized until the Hellman−Feynman force of each atom was lower than 0.05 eV $Å^{-1}$.

The build bulk NiCoLDH possesses two-dimensional structure composed of 20 nickel atoms, 20 cobalt atoms, 80 oxygen atoms and 80 hydrogen atoms in a unit cell (a=21.812, b=15.867, c=23.982 Å). The PEDOT layer has four repeat EDOT units above the NiCoLDH model. The charge density difference and electron localization function (ELF) were carried out based on the literature report.[217]

The desorption energy of H molecule (E^H_{des}) is defined as:

$$E^H_{\mathrm{des}} = \left(E^H_{\mathrm{substrate}} + E^H\right) - E^H_{\mathrm{total}} \qquad (4\text{-}1)$$

Where E^H_{total}, $E^H_{\mathrm{substrate}}$ and E^H represent the total energies of adsorbate-substrate, substrate and isolated adsorbate, respectively.

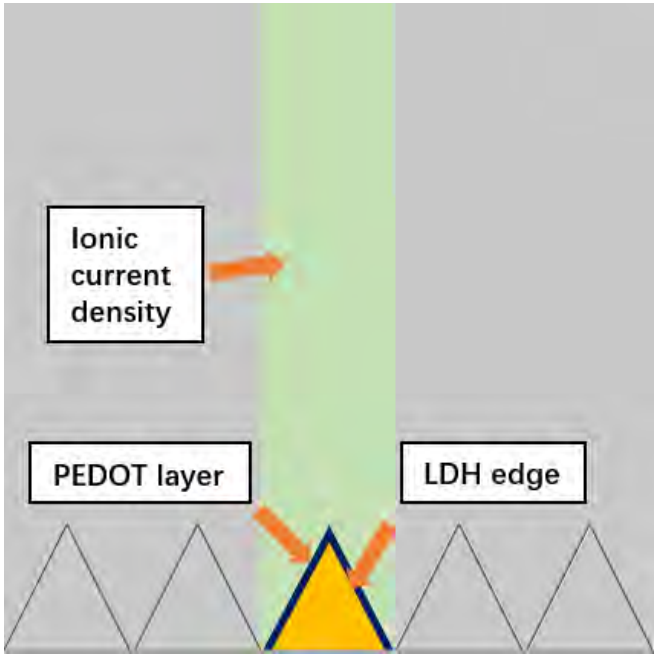

Figure 4.2 The schematic illustration of built model where selected yellow, black and green regions represents LDH, PEDOT and electrolyte, respectively.

4.3. Results and discussion

4.3.1. Characterizations

Figure 4.3a shows the typical appearance of carbon fiber with smooth surface. After the electrodeposition process, multiple nanosheets are grown uniformly and interlaced on the carbon fiber surface as exhibited in **Figure 4.3b**, indicating the successful electrodeposition process. The nanosheets are NiCo layered double hydroxides. As to the PEDOT-coated samples shown in **Figures 4.3c-e**, it can be seen that PEDOT layer becomes more obvious with the increasing of coating time from 5 mins to 10 mins and 20 mins, corresponding to the increased thickness of PEDOT layer among the LDH surface. In addition, it should be noted that the original structure of LDH sample can be maintained without any damage, highlighting the unique ability of oCVD technology to grow a PEDOT layer compatible with the substrate.

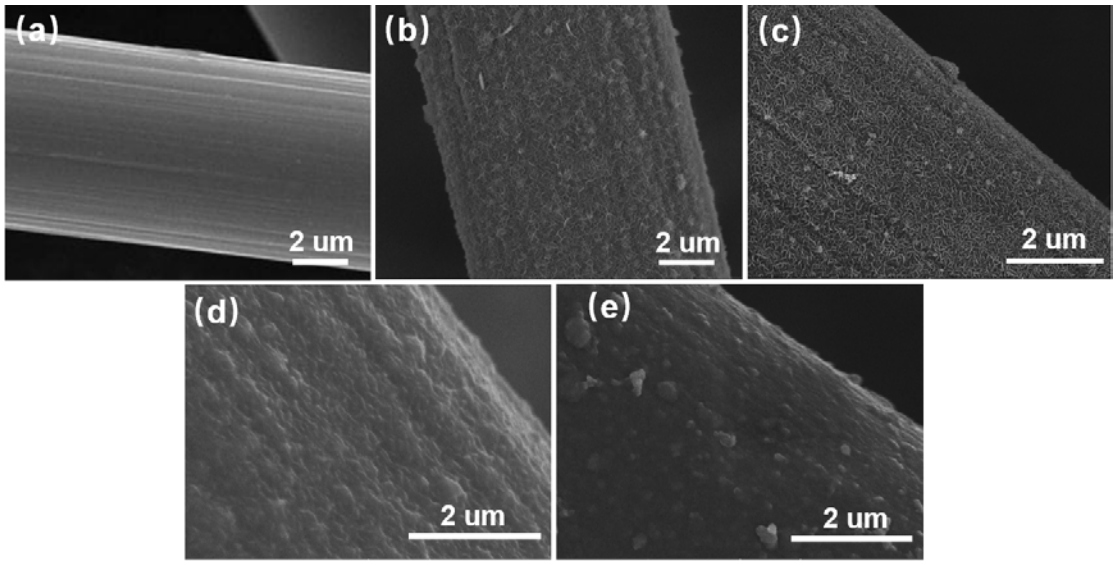

Figure 4.3 FE-SEM images of (a) carbon fiber, (b) the LDH sample, (c) the LDH/PEDOT-*5* sample, (d) the LDH/PEDOT-*10* sample, (e) the LDH/PEDOT-*20* sample.

Furthermore, the TEM images of LDH/PEDOT-*10* sample are exhibited in **Figures 4.4a,b,** where the nanosheet structure consists of randomly dispersed small and well-crystallized lattice fringes. The corresponding lattice spacing is calculated to be 0.26 nm, which can be assigned to the NiCoLDH crystal structure.[218] Moreover, the thickness of as-made PEDOT-coated samples are measured from 5nm, 10nm to 40nm

as exhibited in **Figures 4.4c-e**, which is consistent with the tendency of structural evolution observed in SEM images (**Figures 4.3c-e**). Additionally, the coexistence and uniform distribution of Ni, Co, C, O and S elements can be detected by the energy dispersive X-ray spectrometry (EDS) mapping analysis in **Figure 4.5**, indicating the successful and uniform PEDOT coating. Such kind of precisely thickness-controlled PEDOT layer can make it achievable to give deep insights into the influence of thickness of PEDOT layer on electrochemical performance of LDH.

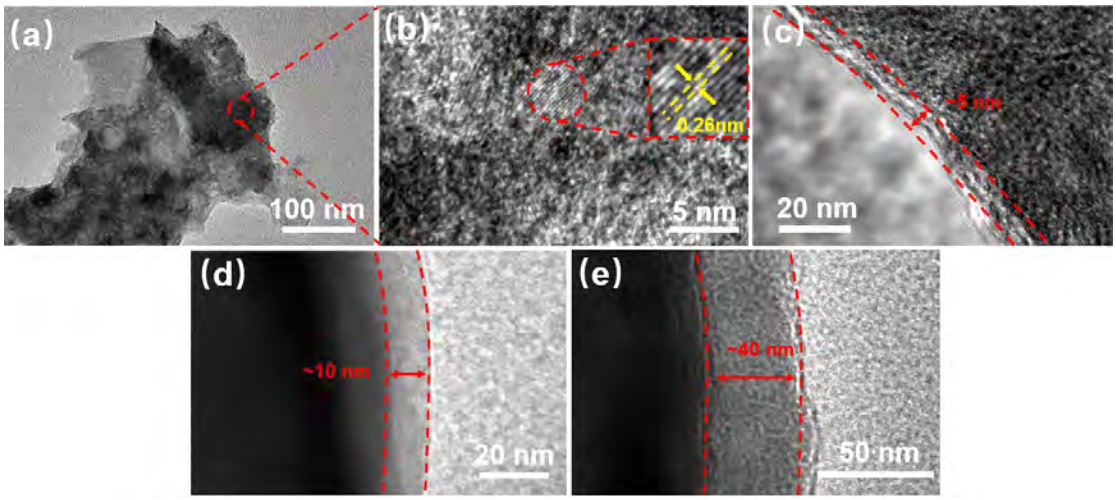

Figure 4.4 (a) TEM image of the LDH/PEDOT-*10* sample. HR-TEM images of (b,c) the LDH/PEDOT-*5* sample, (d) the LDH/PEDOT-*10* sample and (e) the LDH/PEDOT-*20* sample.

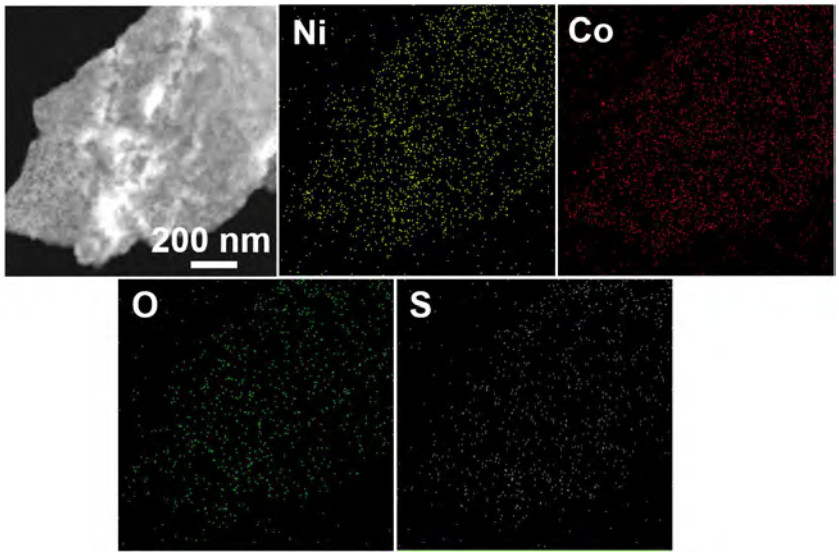

Figure 4.5 STEM image and corresponding elemental mapping of the LDH/PEDOT-*10* sample.

The X-ray diffraction (XRD) patterns of the as-prepared samples are displayed in **Figure 4.6a.** Except for the obvious diffraction peaks of pure carbon fiber, no other peaks can be seen among other samples, indicating that the peak intensities of LDH and PEDOT are too low compared to that of pure carbon fiber. Thus, Raman test was conducted to confirm the existence of PEDOT layer with the obtained spectrum of LDH and LDH/PEDOT-*10* displayed in **Figure 4.6b**. Many new bands especially at higher wave number from 1,300 to 1,600 cm^{-1} appeared, which can be attributed to the typical C_α-C_β stretching vibration of PEDOT molecule.[219] Furthermore, the surface characteristics and elemental compositions of the as-made samples were detected by X-ray photoelectron spectroscopy (XPS) in **Figure 4.7a**. Low-resolution XPS survey verifies the presence of C, Ni, Co and O elements in the LDH sample, while S element appears in the LDH/PEDOT-*10* sample, further confirming the presence of PEDOT film layer. Detailly, as shown in **Figure 4.7b**, high resolution Ni 2p spectrum exhibits two main peaks of $2p_{3/2}$ and $2p_{1/2}$ orbitals, along with corresponding two shake-up satellites. The similar peaks of Ni 2p can be seen from these two samples, meaning that the thin PEDOT film shows no influence on the intrinsic property of the substrate sample.[220] The similar result can be also confirmed by the high-resolution of Co 2p spectrum in **Figure 4.7c**.[220] For the S elements, there are four types of sulfur in the composite, which are assigned to aromatic sulfur (S–C groups) at 164.0/165.4 eV and the other oxidized sulfur at around 169.4/170.5 eV as shown in **Figure 4.7d**, indicating the existence of PEDOT layer.[221]

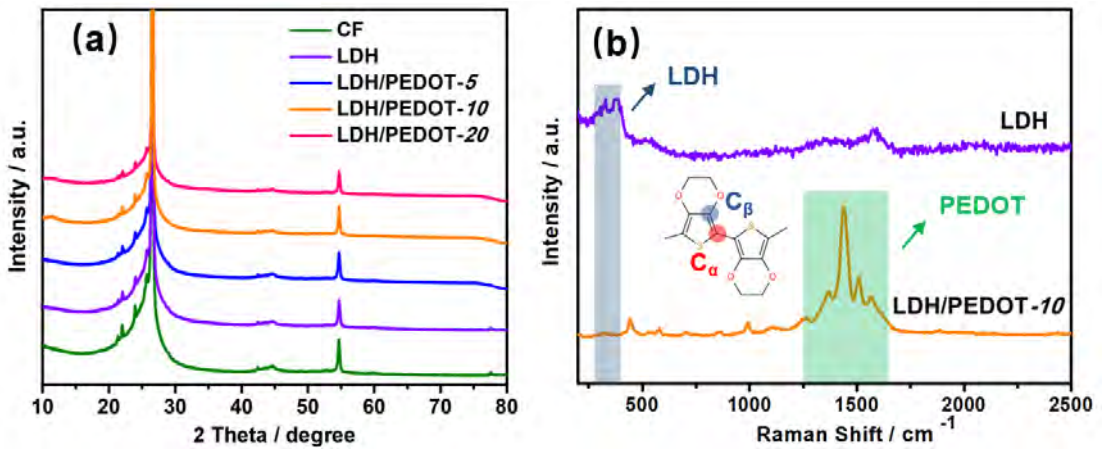

Figure 4.6 (a) XRD patterns of the as-prepared samples. (b) Raman survey spectra of the and LDH and LDH/PEDOT-*10* samples.

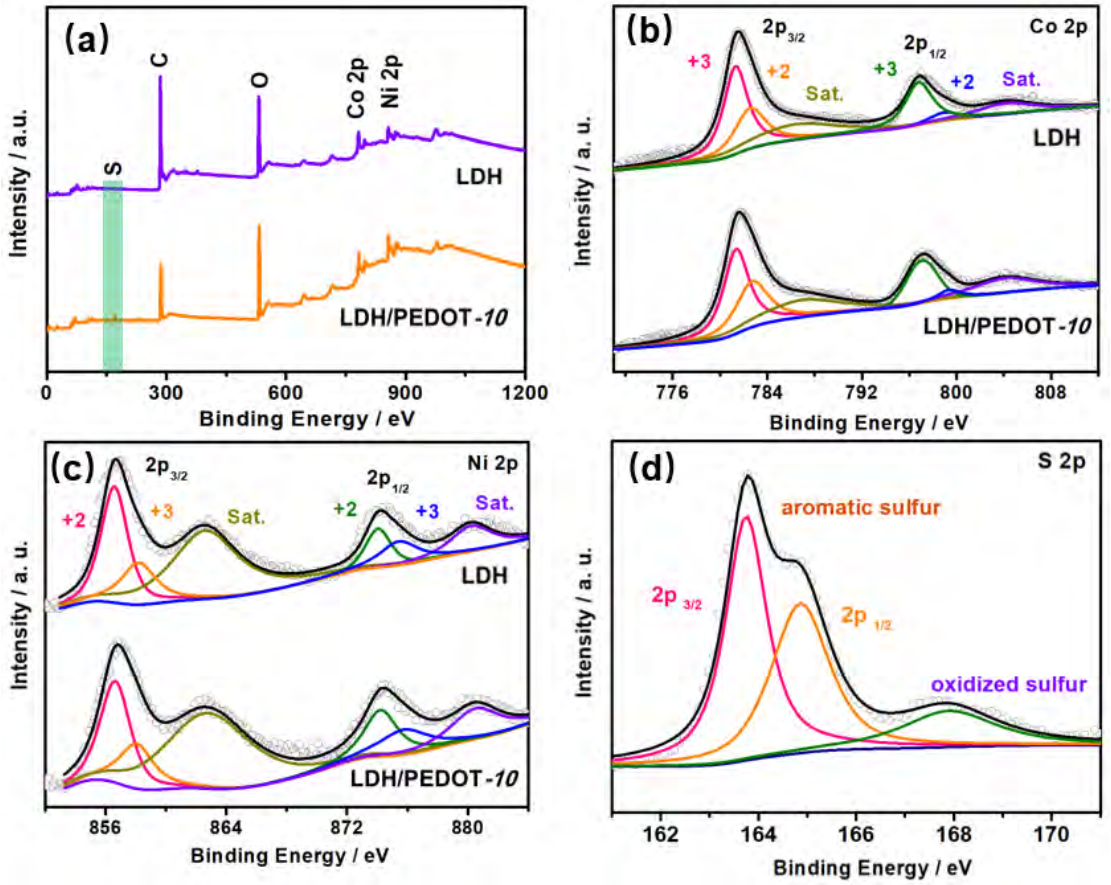

Figure 4.7 (a) The XPS spectra of the LDH and LDH/PEDOT-*10* samples. (b-d) High-resolution Co 2p, Ni 2p and S 2p spectra of the as-made samples.

4.3.2. Electrochemical performance

The electrochemical performances of the as-prepared samples were firstly tested in the three-electrode system to evaluate the electrochemical performance. **Figure 4.8a** shows the typical CV curves of LDH electrode at various scan rates from 0.1 to 1 mV s^{-1}. A wide oxidation region composed of two redox peaks (P1 and P2) located at 0.25-0.35 V can be seen owing to the slightly overlapping redox reactions of multiple valances of cobalt (P1/P3) and nickel (P2/P4) ions inside the electrode, which has been widely observed by the previous works.[118, 222, 223] On the contrary, the current response of LDH/PEDOT-*10* electrode exhibits nearly a single peak at each scan rate in **Figure 4.8b**, indicating that a favorable electrochemical reaction kinetics of the electrode was achieved after the PEDOT coating. Besides, the CV curves of electrodes with different coating time (from 5 to 20 mins) at 2 mV s^{-1} are presented in **Figure 4.8c**, where LDH/PEDOT-*20* electrode shows obviously decreasing capacitance, indicating the thick PEDOT film (up to 40nm as shown in **Figure 4.4e**) can cause adverse influence

on the capacitance loss of active material due to the insufficient contact between the active material and electrolyte.

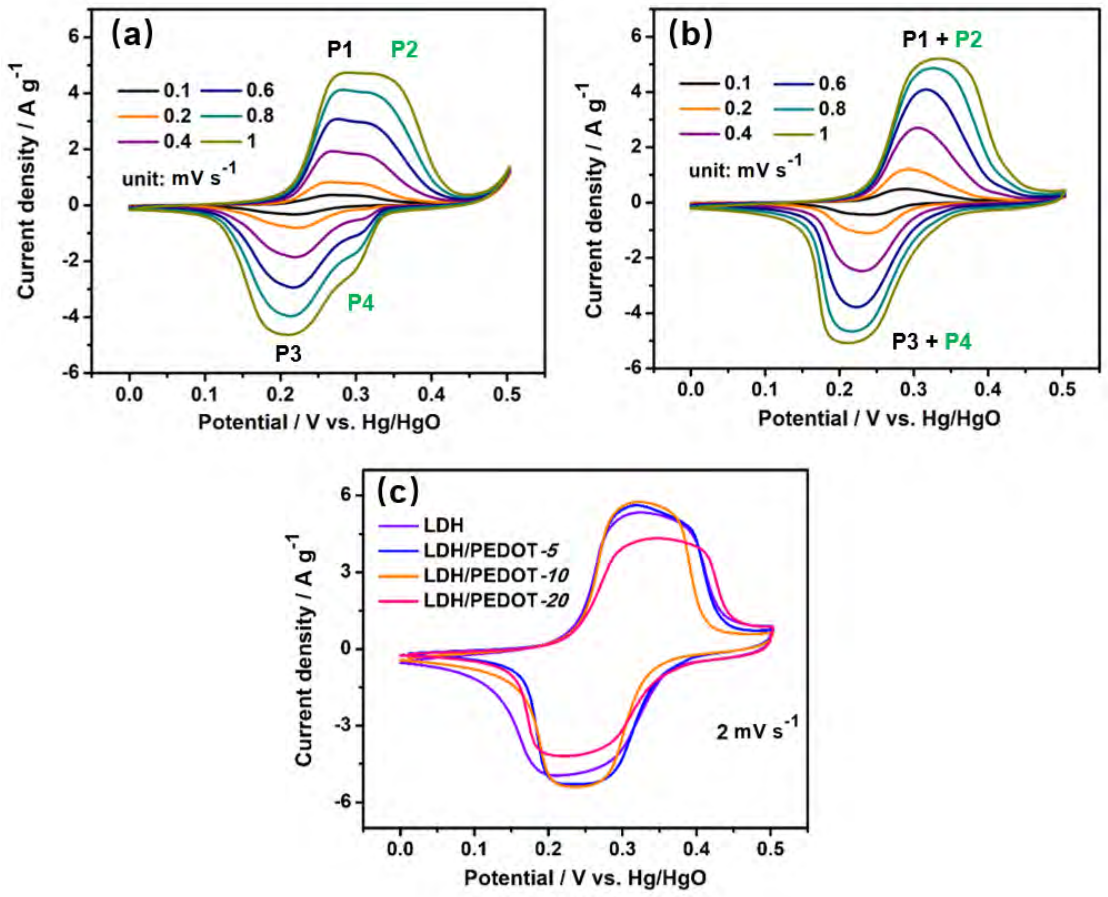

Figure 4.8 CV curves of (a) LDH and (b) LDH/PEDOT-*10* electrodes at 0.1-1 mV s^{-1}. (c) CV survey spectra of the as-prepared electrodes at 2 mV s^{-1}.

With the increase of scan rates from 2 to 20 mV s^{-1}, the distortion can be found among the CV curves because the larger polarization happened at higher scan rates (**Figure 4.9**).[224, 225] Specifically, the recovery curve from 0.5 V to 0 V at high scan rate of 20 mV s^{-1} can be selected as the indicator for rate performance. The released electric energy is influenced by the impedance and intrinsic reaction kinetics inside the sample. The quick current value changes in reverse can be regarded as the behavior of better reversible redox reaction, corresponding to the higher reaction kinetics during the reaction.[110, 226, 227] Thus, it can be assumed that the LDH/PEDOT-*10* sample with less distortion shows higher reversible redox peaks compared to others, meaning its enhanced rate performance. The LDH/PEDOT-*20* sample with the largest distortion is

also considered to exhibit the lowest rate performance among the samples, owing to its thick thickness of PEDOT skin layer.

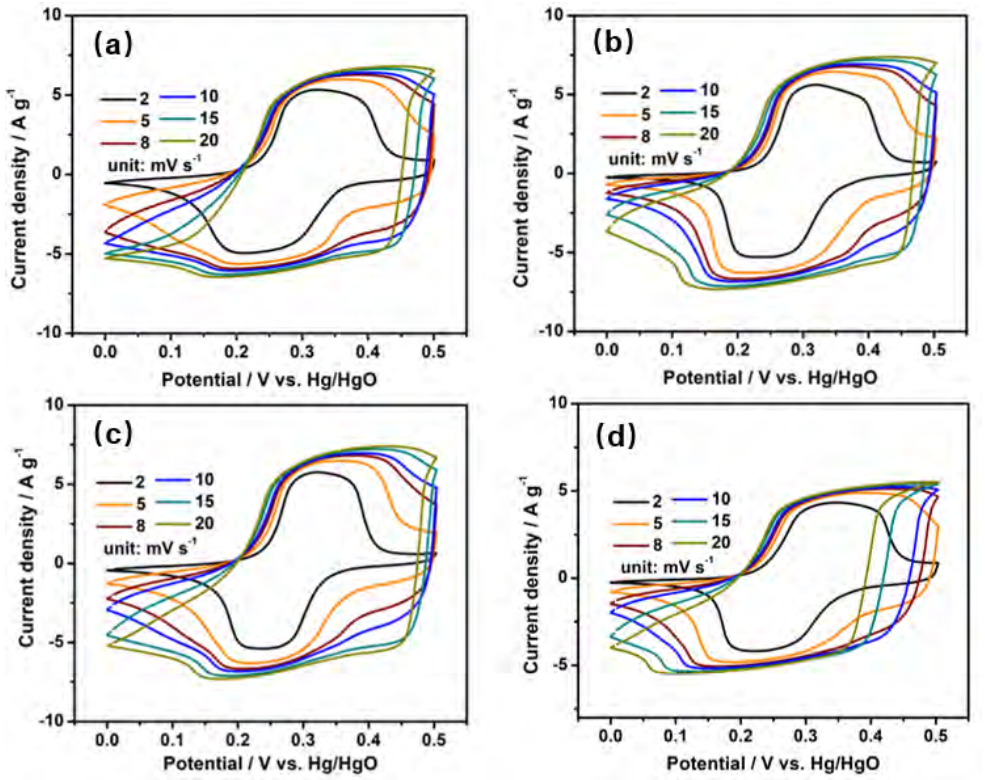

Figure 4.9 CV curves of (a) LDH, (b) LDH/PEDOT-*5*, (c) LDH/PEDOT-*10* and (d) LDH/PEDOT-*20* samples at various scan rates from 2 to 20 mV s^{-1}.

Further, the as-made electrodes were tested by galvanostatic charge/discharge (GCD) tests with results in **Figure 4.10**. It is clear that the LDH, LDH/PEDOT-*5* and LDH/PEDOT-*10* electrodes show nearly the same specific capacitance around 1,250 F g^{-1} at low current density of 1 A g^{-1} within the working voltage from 0-0.48 V (**Figure 4.10a**). However, the value of LDH/PEDOT-*20* electrode (around 1,050 F g^{-1}) decreases apparently because of the presence of thicker PEDOT film (up to 40 nm as shown in **Figure 4.4e**) with the resulted long ions diffusion pathway. Additionally, the charging and discharging curve of LDH/PEDOT-*10* are more symmetric compared with others, indicating its better reaction kinetics with lower degree of polarization. Besides, the calculated capacitances based on the GCD results of as-made electrodes are summarized in **Figure 4.10b** and the detailed GCD curves at different current densities can be found in **Figures 4.10c-f**. The rate performances of LDH/PEDOT-*5* and LDH/PEDOT-*10* electrodes are 79% and 65% from 1 to 50 A g^{-1}, which are higher compared to the LDH (55%) and LDH/PEDOT-*20* (56%) samples. The better performance of LDH/PEDOT-*10* indicates that the optimized thickness of PEDOT film

(10 nm) can facilitate the redox reaction at high current density by providing high electronic conductivity, also confirmed by the lowest electrochemical impedance value of LDH/PEDOT-*10* electrode (**Figure 4.11**).

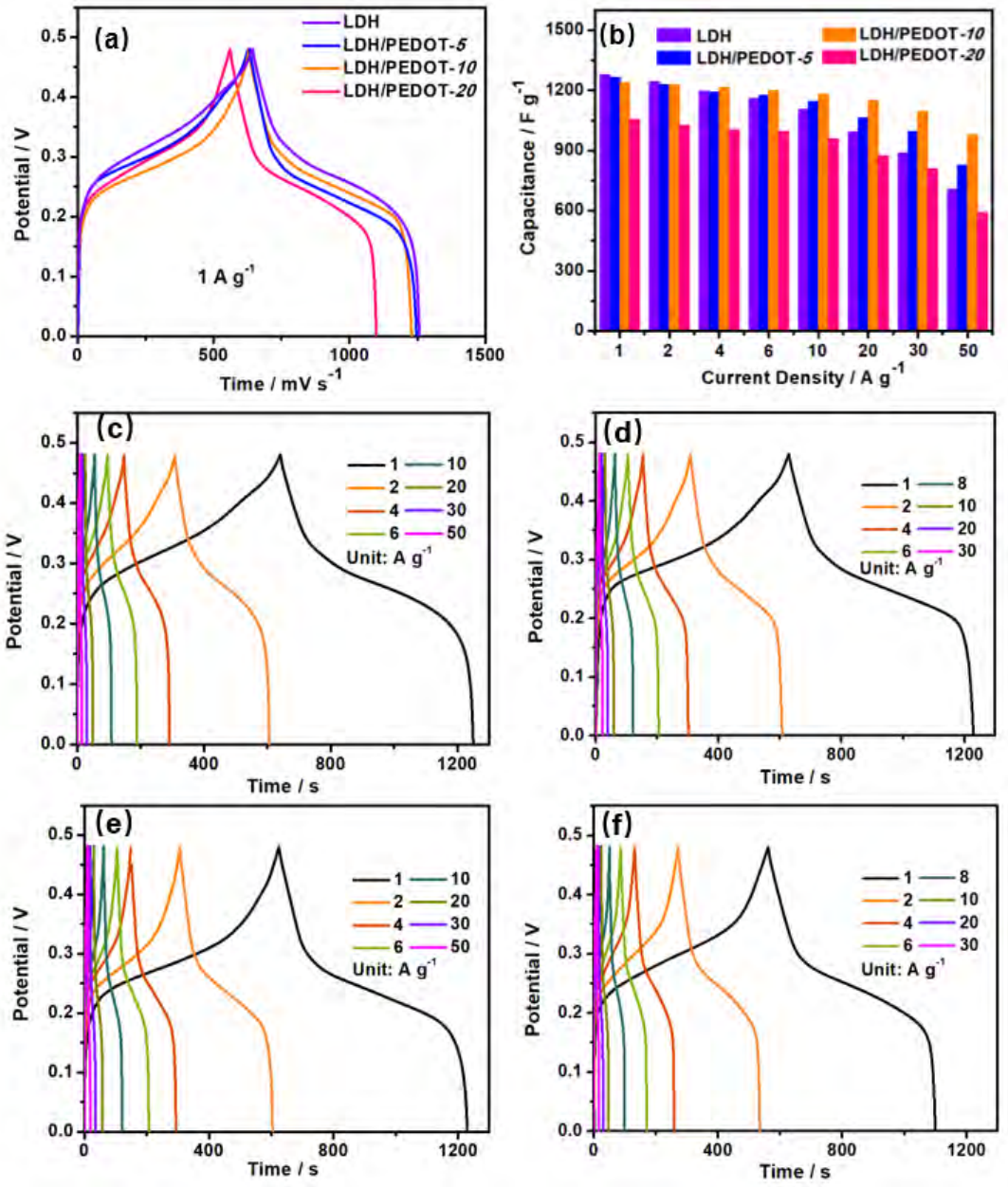

Figure 4.10 (a) GCD profiles of the as-made electrodes at 1 A g^{-1}. (b) The calculated specific capacitances of as-made electrodes on various current densities. (c-f) GCD curves of LDH, LDH/PEDOT-*5*, LDH/PEDOT-*10* and LDH/PEDOT-*20* samples at various current densities from 1 to 50 A g^{-1}.

The long cycling stability results of the tested samples were further carried out and presented in **Figure 4.12**. It can be seen that with the optimized thickness of PEDOT film (10 nm), the resulting LDH/PEDOT-*10* electrode exhibits the longest stability

about 92% retention after 6,000 cycles, which is much higher than that of LDH electrode (~70%). Note that there is an obvious increasing trend for both electrodes at the first 200 cycles, because the activation process derived from the continuous insertion and extraction of ions to the material surface during the operation of supercapacitor.[228]

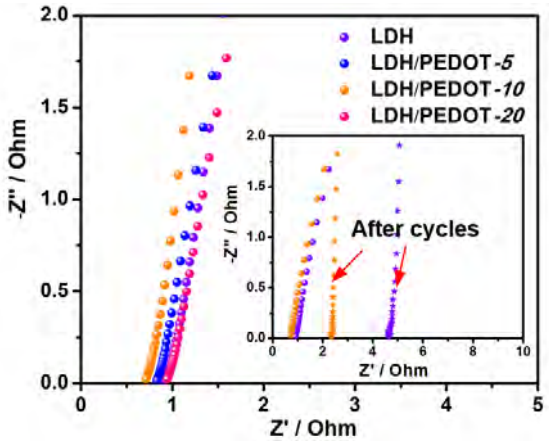

Figure 4.11 The EIS spectra of as-made electrodes (the inset contains EIS spectra after cycling test).

With the progress of cycling, the integrated structure would be gradually deteriorated with continuous structural evolution, creating more contact area between electrolyte and electrode surface and resulting in a slight increase for LDH electrode at around 2,250 cycles and decrease finally due to the collapse of the active material. With a PEODT layer, this phenomenon occurs at around 4,000 cycles due to the improved mechanical cycling stability upon redox cycling. Further, the more integrated structure of LDH/PEDOT-*10* electrode can be obtained after cycling test compared to the distorted structure of LDH electrode, as illustrated in **Figure 4.13**.

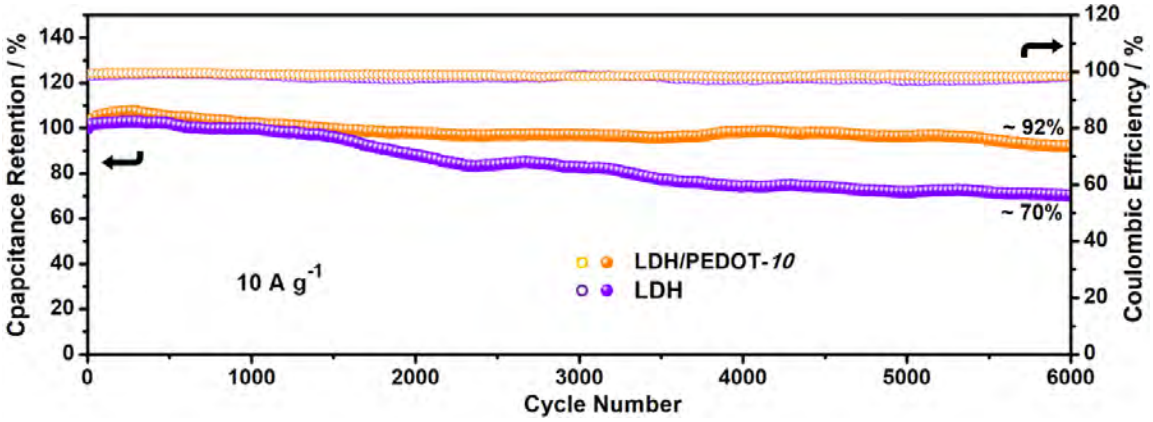

Figure 4.12 The cycling stability tests of LDH and LDH/PEDOT-*10* electrodes for 6,000 cycles at 10 A g^{-1}.

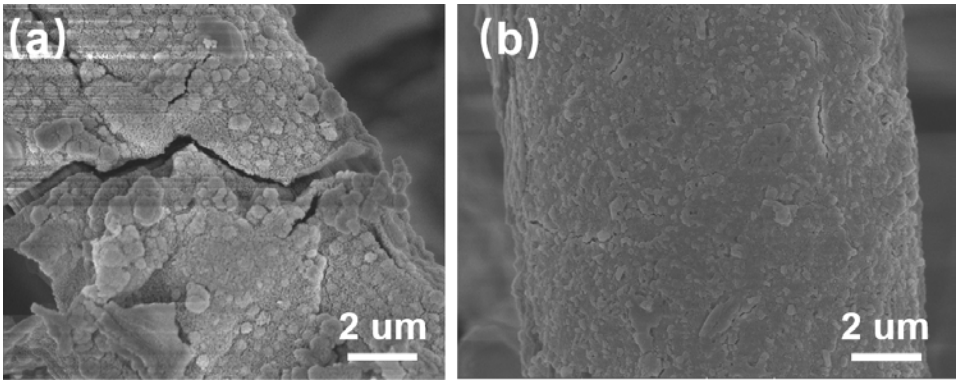

Figure 4.13 SEM images of (a) LDH electrode and (b) LDH/PEDOT-*10* electrode after cycling test.

The presented electrochemical results above indicate the presence of uniform and optimized PEDOT skin can not only utilize high conductivity to improve the rate performance but also enhance the cycling stability attributed to its high mechanical strength. For further evaluating the multifunction of such kind of conductive polymer layer, a multi-potential step measurement (MPSM) technique was employed to investigate the electrochemical performance of LDH and LDH/PEDOT-*10* electrodes. Specifically, by applying potential steps from 0.05 to 0.45 V (green curve) in a typical three electrode system, current response (purple and yellow curves) derived from working electrode at each potential can be obtained owing to various electrochemical processes as shown in **Figures 4.14a,b**. Besides, aiming to reflect the complete electrochemical behavior during the operation, the same duration of 300s was set to ensure the complete electrochemical reaction. The low current responses can be observed at relatively low potentials (from 0 to 0.2 V), which is attributed to a typical capacitive behavior without Faradaic effect. After that, an enlarged current response occurs at the very beginning, followed by a sharply decreased current and finally stabilized at a small value. The larger current value can be regarded as the redox reactions of nickel and cobalt species combined with continuous diffusion of ions from electrolyte to electrode surface. Thus, the total charge (Q_t) calculated by integrating the MPSM curve can be regarded as the indicator reflecting the dynamic electrochemical process as shown in **Figure 4.14c**. The corresponding other results derived from various potentials are summarized in **Figure 4.14d**. It is found that at low voltage, the values of Q_t towards these two samples are nearly the same. With the increase of applied voltage more than 3.5V, the Q_t value of LDH/PEDOT-*10* is higher than that of LDH

and keep at a high level in the following voltages, meaning that the PEDOT-coated sample with higher redox activity shows more capability to achieve a high capacitance.

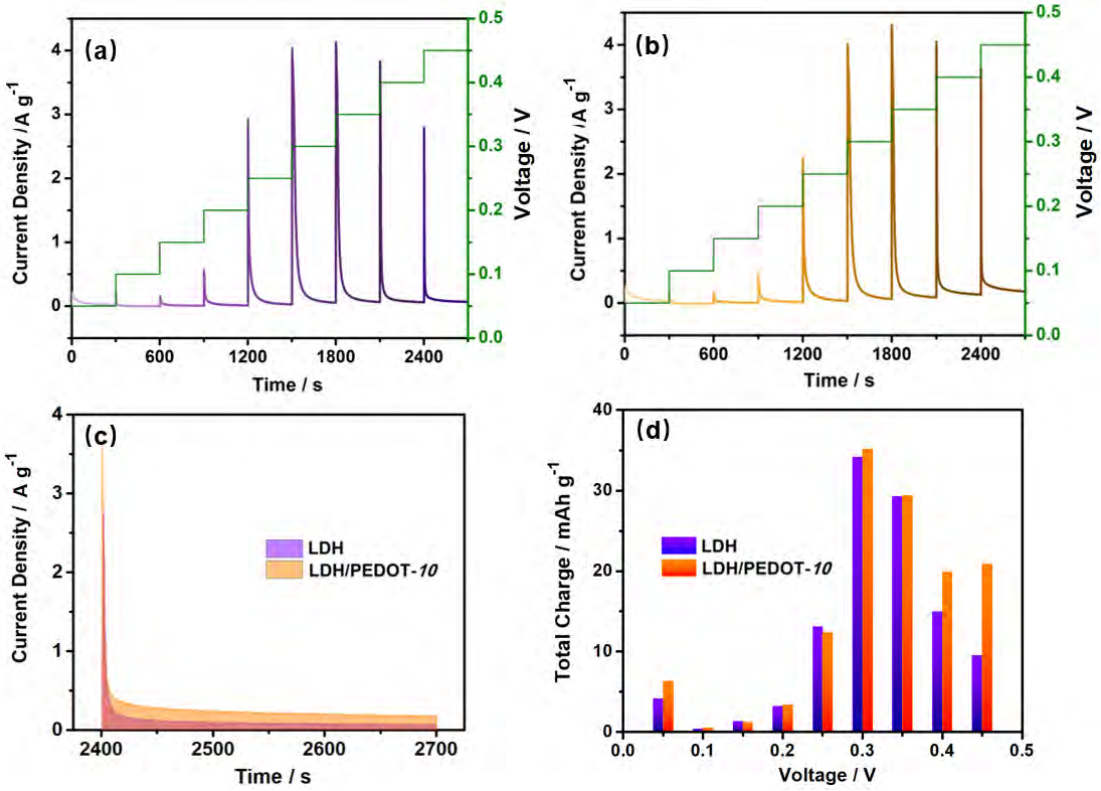

Figure 4.14 (a,b) Schematic diagram for multi-potential steps measurement (green curve: input potential, purple curve: current response of LDH electrode, yellow curve: current response of LDH/PEDOT-*10* electrode). (c) Illustration for the calculation of total charge at each step. (d) The calculated total charges of LDH and LDH/PEDOT-*10* electrodes at each step.

4.3.3. COMSOL stimulation

Aiming to further understand such MPSM results, a COMSOL Multiphysics analysis based on the finite element method was performed to analyze the distribution of OH^- flux among the various surfaces. There are two dominated parameters influencing the stimulation results. One is electronic conductivity, which is related to the polarization behavior of electrode material. The other one is ion diffusivity inside PEDOT thin layer toward OH^- ions. Under the consideration above, the models with three different interfaces were created and briefly illustrated in **Figure 4.15a**. The wave edges of triangle pattern represent the edge of deposited LDH nanosheet and the surface chemical potential decreases linearly from 0.5 to 0 V due to its low conductivity (around 10^{-5} S cm^{-1}).[211, 212] For the PEDOT-coated samples, the corresponding surface

chemical potential along its layer is assumed constant with a value of 0.5 V because of its higher conductivity (exceeding 1,000 S cm^{-1}) and lower polarization degree compared with LDH.[22, 92] Additionally, the ionic diffusion coefficient inside the PEDOT layer was set as the value of 10^{-1} S m^{-1}, which has been generally accepted and proved by previous researchers.[202, 214, 215] Besides, the value for ionic diffusion coefficient in the LDH model was set as the value of 10 S m^{-1}, which is also the typical value of ions in an aqueous solution because the ions can directly diffuse to the surface of LDH.[213] Thus, it can be seen that the ionic current density of thin PEDOT film coverage (model II) increases in the upper region compared to the LDH model (model I), that is because the high conductivity of PEDOT induces more uniform distribution of electric field along the surface of LDH. However, when the thickness of conductive layer continues to increase, the overall value of flux (model III) decreases apparently due to the influence of long diffusion pathway for OH^-, resulting in low diffusion rate. Besides, the distribution of OH^- flux among the surface is also changed significantly after the introduction of conductive layer, as shown by the enlarged image in **Figure 4.15b**. For the uncoated model, the OH^- flux concentrates at the bottom of the valley due to its large voltage drop along the surface, further concentrating the active sites of OH^- near the bottom. On the contrary, the OH^- flux changes to cover larger area among the conductive layer, which can provide more active sites to facilitate the redox process. These experimental and simulation results indicate that the whole electrochemical performance of LDH can be enhanced by introducing the conductive PEDOT layer with suitable thickness to improve the interface condition.

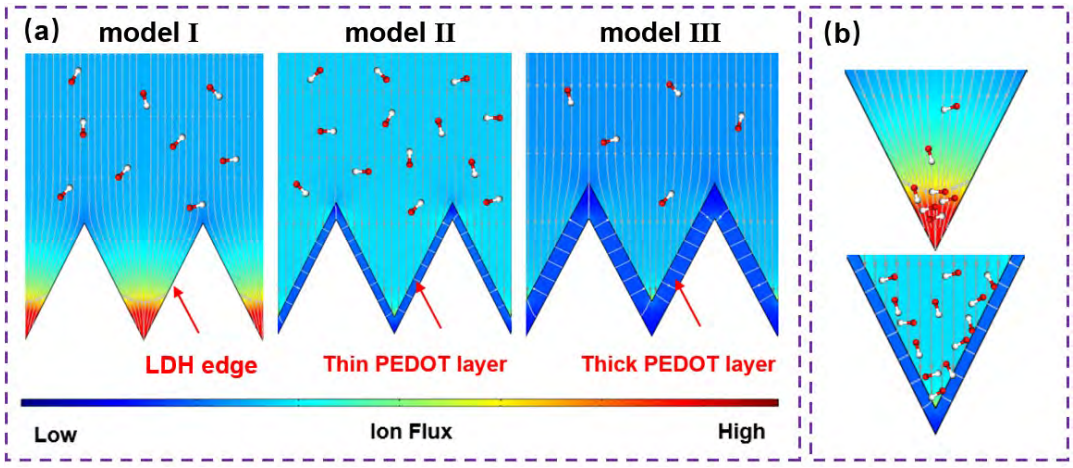

Figure 4.15 (a) The schematic distribution of OH^- flux on the various electrode surfaces. (b) The schematic distribution of OH^- ions among the surface of LDH and thin PEDOT layer models.

4.3.4. First-principles calculations

DFT calculations were further performed to have an insight into the enhanced electrochemical performance of the interfacial structure (LDH/PEDOT). Under the consideration of such a complex system, a simplified model composed of one layer of LDH crystal (composed of 20 nickel atoms, 20 cobalt atoms, 80 oxygen atoms and 80 hydrogen atoms) and PEDOT film (4 repeat EDOT units) was adopted to get a convergent result. The Grimme's zero damping DFT-D3 method was further considered in view of the weak van der Waals dispersion forces between the adsorbates and the surfaces. The top view of the optimized structures of models are shown in **Figure 4.16.** The valence electron localization function (ELF) was firstly employed to stimulate the interaction state among the interface, where ELF values range from 0 to 1 by definition (1.0 means the most localized state). As illustrated in **Figure 4.17a**, the high ELF value at C and O atoms sites for LDH indicates strongly paired electrons owing to their high electronegativities. Moreover, partially ionic bonding states between metal and O atoms can be also observed from the distorted square distribution shape around metal sites. Besides, the ELF distribution at the upper sites of LDH of LDH/PEDOT model is not as high as that of LDH model, indicating the influence of the interaction between LDH and PEDOT. Additionally, the low ELF value between LDH and PEDOT layers indicates that van der Waals (VdW) interactions dominate between layers. These results may enrich the interfacial behavior between LDH and PEDOT, contributing to understand the formation mechanism of this unique structure.

Further, charge density difference was applied to the investigation of the charge transfer after introduction of PEDOT layer into the LDH structure, and also reflected their electrostatic interactions (**Figure 4.17b**). A strong charge accumulation can be found under the PEDOT plane, where the charge depletion region appears near the top sites of O atoms (facing the PEDOT layer). This indicates that there is a charge transfer from LDH crystal to PEDOT layer, which can induce band bending to form a built-in electric field, further contributing to faster charge transfer kinetics. In addition to the electronic structure, the influence of PEDOT was also investigated on the desorption of surface hydrogen atoms, which is a critical step in the redox reaction of metal hydroxides. As illustrated in **Figure 4.17c**, five hydrogen sites were selected denoted as H1 to H5 for samples with/without the coverage of PEDOT thin layer. The calculated results are summarized in **Figure 4.17d**, from where it can be seen that the existence of

PEDOT can lower the desorption energy at each site, highlighting the unique function of PEDOT inducing high redox activity and cycling stability with OH^- in the electrolyte. These combined theoretical results further suggest that the interface of LDH/PEDOT plays a pivotal role in enhancing the redox reaction kinetics and electrochemical performance.

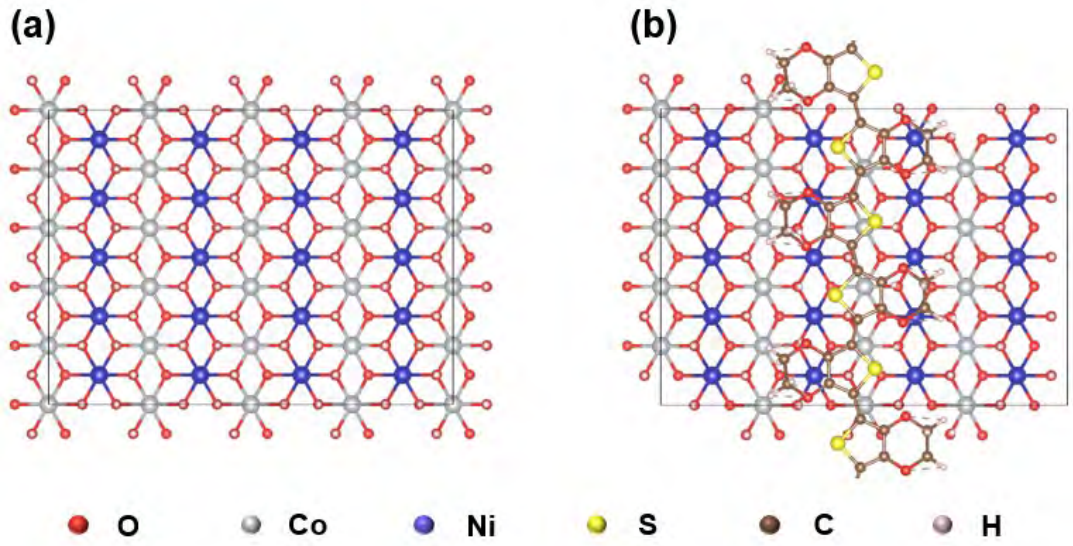

Figure 4.16 The built models of (a) LDH and (b) LDH/PEDOT.

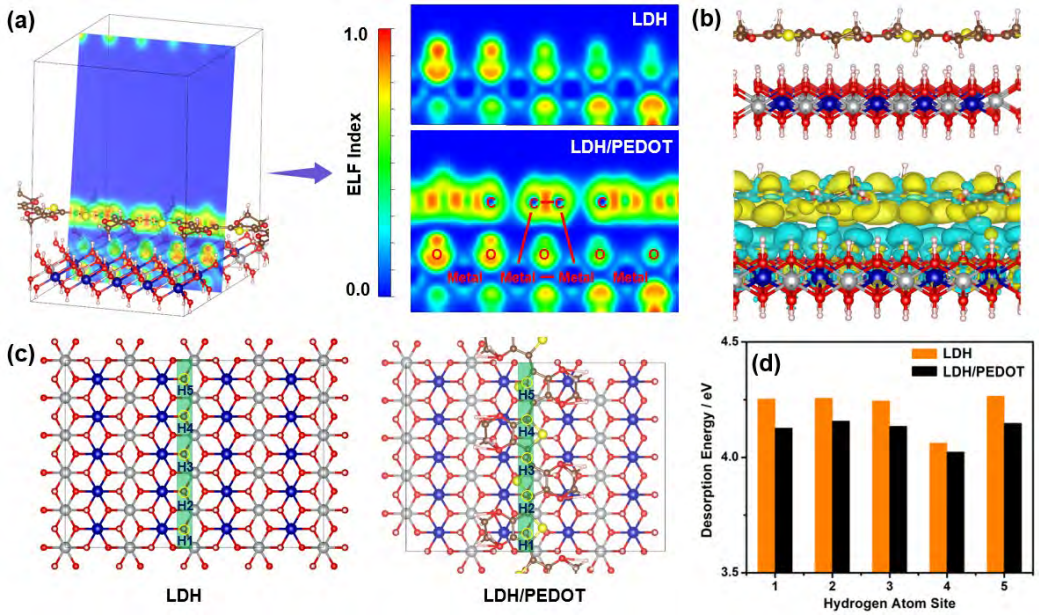

Figure 4.17 (a) Two- and three-dimension ELF results of as-build models. (b) The side view of LDH/PEDOT model and corresponding charge density difference map. (c) The selected desorption sites of H atom. (d) The desorption energy results of as-build models.

4.3.5. Asymmetric supercapacitors performance

To further investigate their potential in practical application, the as-made samples were further evaluated by the two-electrode system. The asymmetric supercapacitors consisted of AC as negative electrode and as-made samples as positive electrode were also immersed in 6 M KOH with voltage range from 0 to 1.6 V. **Figure 4.18** displays the CV curves of the negative and positive electrodes at a scan rate of 5 mV s^{-1}. The redox peak of LDH/PEDOT-*10* positive electrode shows the typical pseudocapacitive type mechanism and the almost rectangular curve of AC shows the obvious double-layer capacitive mechanism. The tested CV and GCD curves of asymmetrical supercapacitors are presented in **Figure 4.19.** It can be seen that LDH/PEDOT-*10*//AC can retain the shape of CV curves with the scan rate increasing from 2 to 20 mV s^{-1}. On the contrary, the disappearance of redox peak at high scan rate of 20 mV s^{-1} LDH//AC indicates its poor rate performance. Further, the calculated capacitances based on the GCD results are displayed in **Figure 4.20a**. From the current densities of 0.5 and 10 A g^{-1}, the LDH/PEDOT-*10*//AC and LDH//AC devices can achieve high specific capacitances of 163 F g^{-1}/93 F g^{-1} and 164 F g^{-1}/71 F g^{-1}, respectively, indicating the better rate performance of LDH/PEDOT-*10*//AC. The calculated energy density and power density are summarized in **Figure 4.20b.** A maximum energy density of 58 Wh kg^{-1} can be achieved at a power density of 400 W kg^{-1}, which is much higher than the reported results for a similar electrode.[229-234] Moreover, the LDH/PEDOT-*10*//AC can achieve a high capacitance retention of 80% after 6,000 cycles at a current density of 5 A g^{-1}, which is much higher than that for LDH//AC with only 75% capacitance retention after 1000 cycles (**Figure 4.21**). As discussed in **Figure 4.12**, the low electrochemical stability of LDH is its inherent characteristics in three electrode system. For the as-made LDH//AC device, the mismatched electrical storage mechanism of electrodes of two sides can cause rapid drop of capacity at the initial cycling test. The fast capacity decay in capacitance can be further observed after 400 cycles, owing to the competition between the exposure of the active sites of the electrode material and the continuous collapse of the electrode structure. On the contrary, the enhanced reaction kinetics and mechanical support by introducing PEODT skin onto the LDH can largely adapt the mechanism difference of electrical storage behavior and buffer the stress originating

from the volume variation of materials during the cycling test, leading to a better cycling performance of LDH/PEDOT-*10*//AC device.

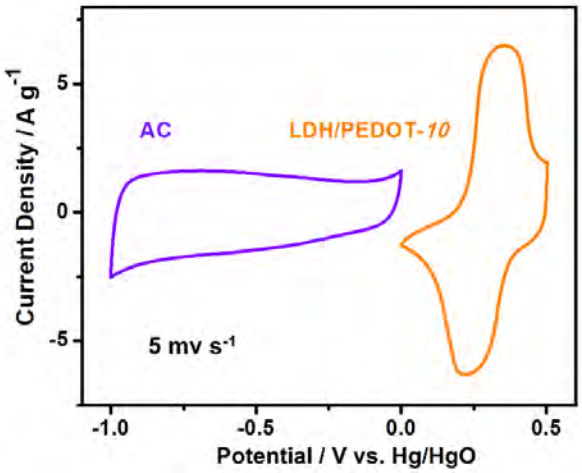

Figure 4.18 CV curves of AC and LDH/PEDOT-*10* samples at a scan rate of 5 mV s^{-1}.

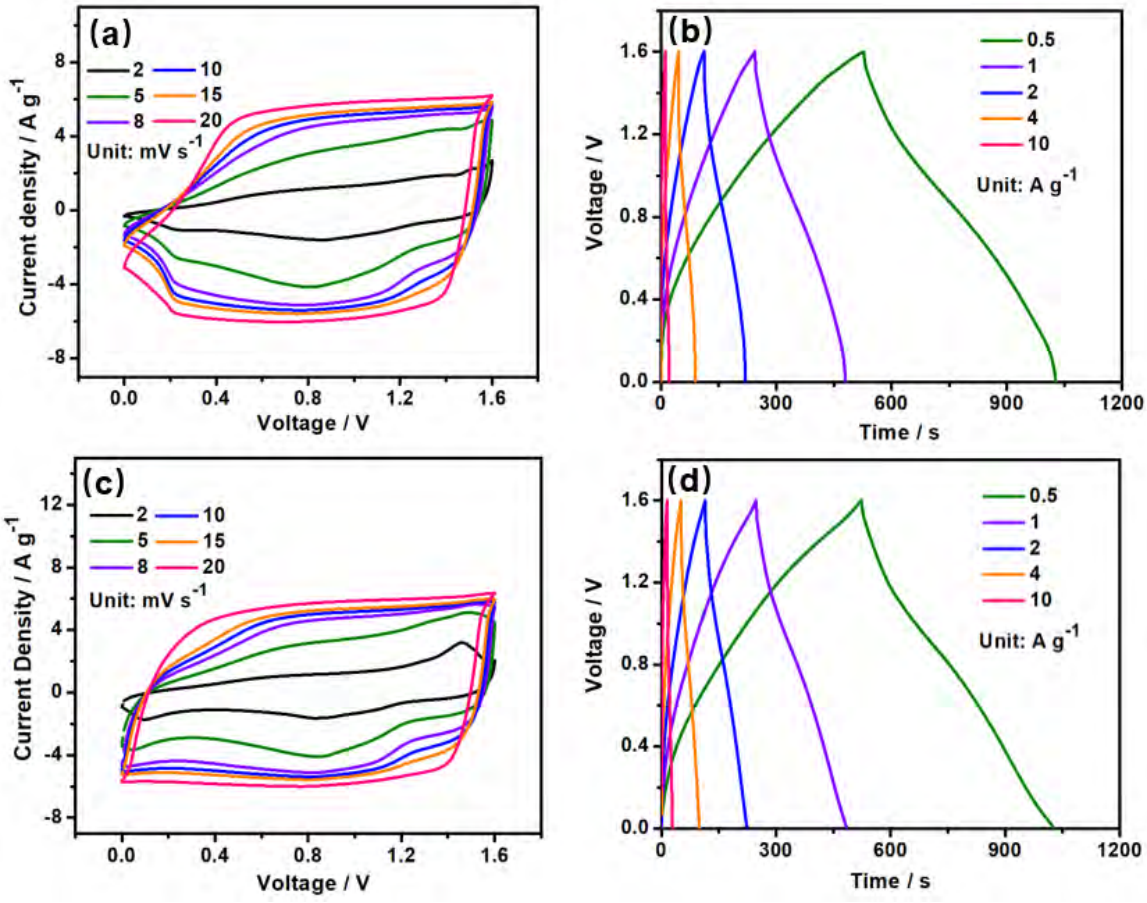

Figure 4.19 CV curves at various scan rates and GCD curves at various current densities of the (a,b) LDH/PEDOT-*10*//AC and (c,d) LDH//AC.

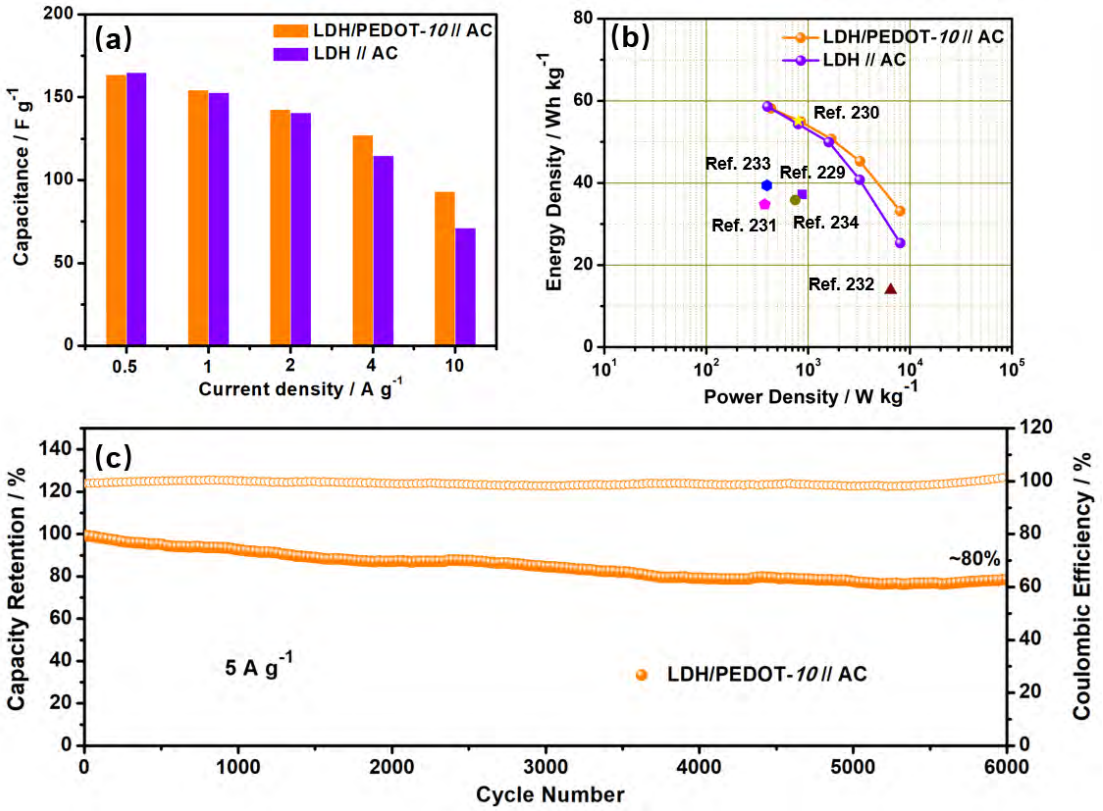

Figure 4.20 (a) The calculated capacitances of LDH/PEDOT-*10*//AC and LDH//AC based on the GCD curves, (b) Energy densities and power densities curves of LDH/PEDOT-*10*//AC and LDH//AC, (c) Cycling stabilities of LDH/PEDOT-*10*//AC at a current density of 5 A g^{-1}.

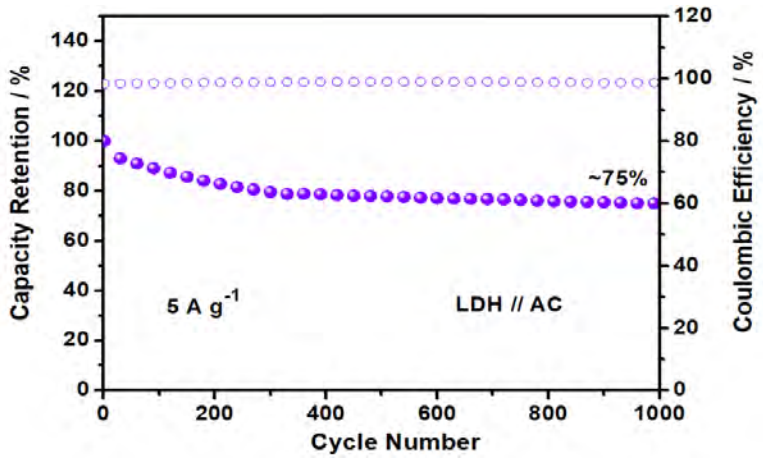

Figure 4.21 Cycling stabilities of LDH//AC at a current density of 5 A g^{-1}.

4.4. Summary

In summary, a facile and controllable strategy was introduced to deposit conductive PEDOT skin onto the surface of NiCo layer double hydroxides. The role of such kind of conductive PEDOT skin for enhanced SCs performance was investigated on samples with coating thickness of PEDOT skin controlled respectively at 5, 10 to 40 nm by varying the deposition time. Excellent performance on capacitive energy storage was found for 10 minutes coating incidentally having 10 nm thickness, LDH/PEDOT-*10*. This is attributed to the synergistic effect of optimized potential distribution and OH^- flux pathway along the surface of LDH nanosheet by the conductive polymer. Additionally, DFT simulations show that the charge transfer and possible built-in electric field at the interface between LDH and PEDOT could significantly accelerate reaction kinetics. PEDOT also leads to a lower desorption of H^* atoms from the LDH structure. The fabricated LDH/PEDOT-*10*//AC device asymmetrical supercapacitor exhibits a relatively high energy density of 58 Wh kg^{-1} at a power density of 400 W kg^{-1} along with enhanced cycling stability (80% retention after 6,000 cycles). This work may open a new way for the design and fabrication of novel structure for energy storage material.

Chapter 5 Enhanced Reversible Sloping Capacity Enabled by Boron-Doped Sites in Porous Carbon Nanosheet

5.1. Introduction

Sodium ion capacitors (SICs) are considered as competitive and promising alternatives for high-performance energy storage devices, which combine the high energy output feature of the battery-type anode and the fast charging-discharging feature of the capacitive-type cathode.[58, 235-237] Nevertheless, further development of SICs still suffers from the lack of appropriate electrode materials with acceptable electrochemical behavior to match the ion transfer kinetics of electrodes on both sides, leading to the unsatisfied electrochemical performance.[13, 121, 238, 239] For anode materials of SICs, hard carbon (HC) stands out owing to its abundance, low cost and modifiable surface configuration.[240-243] Sodium ions can be absorbed and intercalate into the local rumpled and short-ordered graphitic structure of HC forming intercalation compound (NaC_x).[244-246] However, the low electrochemical reaction potential plateau (0.01-0.1V) of ion intercalation is easily affected by polarization at high current density, resulting in low rate capability of SICs. It may also trigger sodium plating and cause the destruction of the carbon structure so as to bring about safety issues and degrade electrochemical performance.[247-250] Thus, the development of advanced hard carbon with improved sloping capacity is still a big challenge in the construction of high-performance SICs.

Many efforts have been made to improve the sodium storage capability by tuning the morphology and composition of the hard carbon materials. On the one hand, porosity engineering is an effective strategy to regulate the structure of amorphous carbon materials for increasing atomic disorder at sub-nm scale. The well-developed hierarchical pore structure can provide highly accessible surface areas coupled with fast ion channels for sodium ions transportation.[251-254] On the other hand, heteroatom doping, such as nitrogen, phosphorus, sulfur and boron, can be regarded as another strategy to modify carbon surface configuration.[255-257] Physically, the interlamellar spacing of carbon nanosheet can be enlarged by introducing specific doped heteroatom with large atomic radius, thus broadening the transfer approach and storage space for Na ions.[258, 259] Chemically, the heteroatom doping can cause the charge

distortion/redistribution of the original carbon atom, change the electron transfer behavior and further induce lower adsorption barrier for sodium ions, which shows high promise for boosting pseudocapacitive capacity without trading off initial columbic efficiency.[260, 261] For example, Pan *et al.* introduced ample sulfur-carbon bonds (C-S-S-C) on the edge of carbon skeleton to extend accessible subsurface region, yielding enhanced sodium ions storage performance via expanding pseudocapacitive contribution from a stepwise redox reaction between sodium and sulfur.[262] Additionally, Jiang *et al.* proposed ultrahigh phosphorus (P) doped carbon anode for sodium ion battery application. The strong confinement effect of interlayer P-P bonds coupled with alloying reaction of elemental P and Na make it achievable to obtain a high electrochemical performance with large pseudocapacitive contribution.[263] Nowadays, in-plane substitutional doping of boron (B) atom in carbon network has been widely investigated from experimental and theoretical perspectives for energy storage and conversion application.[264] Note that all peripheral electrons of B atom are easily participated in σ-bonds of carbon atom, which can maintain the pristine carbon nanostructures. Besides, a *p*-type boron doping site can be introduced due to the short of one electron compared with one carbon atom, thus enhance the electrostatic adsorption between carbon surface with metal atom.[265] However, there is still a lack of simultaneous regulation of the component and structure to increase the pseudocapacitive capacity ratio for sodium ions storage by introducing boron doping into the porous carbon structure.

With the above analysis, a new and facile strategy is proposed here to fabricate boron-doped porous carbon nanosheet material (BPCN) with the aid of H_3BO_3 as boron source while zinc nitrate hexahydrate as pore-forming agent. Such kind of boron-doped porous carbon nanosheet is the first time to be used as high-performance electrode material for sodium ion capacitor application. By investigating multiple characteristic measurements, kinetic analysis and DFT calculations, the mesopore-dominated porous structure combined with ample boron-doped sites are employed as anchoring sites for sodium ions to promote pseudocapacitive capacity during the charge and discharge process. Thus, the obtained BPCN electrode delivers a high capacity of 357 mAh g^{-1} at 0.1 A g^{-1} while a specific capacity of 164 mAh g^{-1} can be maintained at a high current density of 10 A g^{-1}. Moreover, a superior long cycle performance can be also achieved after 1,000 cycles under 320 mAh g^{-1} at 1 A g^{-1}. In addition, the assembled SICs using BPCN as negative electrode and commercial activated carbon (YP-50) as positive

electrode delivers a maximum specific capacity of 64.8 Wh kg^{-1} and a good cycling retention of 80% after 1,500 cycles at 1 A g^{-1}.

5.2. Experimental section

5.2.1. Fabrication of boron-doped porous carbon nanosheet (BPCN)

The facile synthesis procedure is briefly illustrated in **Figure 5.1**. The citric acid monohydrate (1 g), boric acid (1.5 g) and zinc nitrate hexahydrate (2.0 g) were directly dissolved into 30 mL pure deionized water, further stirring at 80 °C for 0.5 hours to ensure that the chemicals were completely dissolve.[60] Then, the above mixture was dried using a typical freeze-drying procedure for 24 hours at a temperature around -20 °C and an intensity of pressure around 10 Pa, aiming to keep the porous and loose cross-linked structure of the as-obtained precursor.[266] The uniformly mixed precursor can be easily obtained where boric acid, citric acid and zinc nitrate are used as boron source, carbon source and pore-creating agent, respectively. Further, the obtained precursor was annealed in a tube furnace with a heating rate of 5 °C min^{-1} to reach 900 °C then kept at 900 °C for two hours. Afterwards, the obtained sample was purified using 150 ml 2 M HCl for 6 hours at 80 °C. The boron-doped porous carbon nanosheet (BPCN) can then be obtained and collected after washing with DI water for four times. It is dried in the oven at 70 °C for 12 hours.

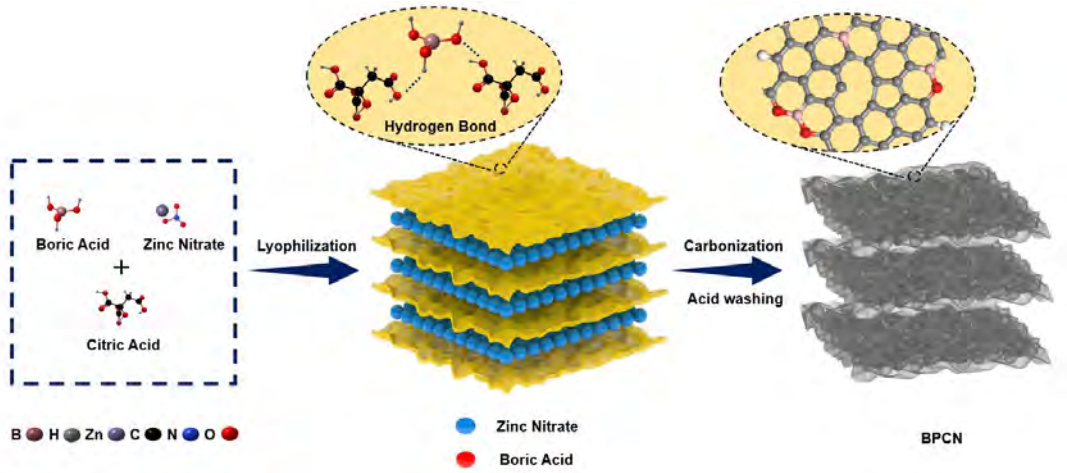

Figure 5.1 The schematic illustration of the fabrication of BPCN sample**.**

5.2.2. Fabrication of boron-doped carbon nanosheet (BCN) and porous carbon nanosheet (PCN)

For the fabrication of boron-doped carbon nanosheet (BCN) sample, the citric acid monohydrate (1 g) and boric acid (1.5 g) were directly dissolved into 30 mL pure deionized water and stirring for 0.5 hours at 80 °C, followed by the same procedure for obtaining BPCN sample.

The fabrication of porous carbon nanosheet (PCN) is similar to that of BPCN but without the addition of boron source. Namely, the citric acid monohydrate (1 g) and zinc nitrate hexahydrate (2 g) were directly dissolved into 30 mL pure deionized water and stirring for 0.5 hours at 80 °C, followed by the same procedure for obtaining BPCN sample.

5.2.3. Material characterization

The corresponding surface chemical states were analyzed and recorded by X-ray photoelectron spectroscopy. The surface structures and morphologies of the as-made samples were observed by field-emission scanning electron microscopy (FE-SEM) and transmission electron microscopy (TEM). X-ray diffraction and Raman spectroscopy patterns were obtained to analyze the morphology and chemical states of as-prepared samples. Additionally, the detailed Brunauer-Emmett-Teller (BET) surface area and the pore size distributions were investigated by nitrogen adsorption/desorption isotherms analyzer.

5.2.4. Electrochemical characterization

The as-obtained samples were prepared and served as electrodes both in half- or full-cell for studying their electrochemical sodium storage performance. The working electrodes were fabricated by spreading the slurry of electrode materials on Cu foil, which was composed of active materials (BPCN, PCN or BCN), carbon black, and polyvinylidene fluoride (PVDF) binder with a mass ratio of 8:1:1, and then drying at 80 °C in vacuum oven for 12 hours. The mass loading was around 0.8-1 mg cm^{-2} (based on the quantity of active material). The CR2025 type coin cells were assembled in a

MBRAUN glove box filled with ultrahigh purity Argon. For the half-cell configuration, metallic sodium foil was employed as counter and reference electrodes, glass fiber filter paper acted as the separator, and 1 M $NaPF_6$ in diglyme (80 µl) was used as the electrolyte, respectively. For the full-cell fabrication, the cathode and anode active material were commercially available carbon (YP-50) and pre-sodiumzed BPCN, respectively, and the mass ratio of cathode to anode was set at 4:1 for balancing the same amount of charge on both sides.[265] Pre-sodiumization of BPCN was carried out by cycling the electrode for ten times in the half-cell aiming to compensate the loss of sodium during the first few cycles in the full-cell. CV curves were obtained by using LAND Battery Testing System at different scan rates in the voltage range of 0.01–3.0 V (vs Na^+/Na) for half-cell and 0.01–4.0 V for full-cell. Galvanostatic discharge/charge tests were carried out on a LAND CT2001A instrument at different current densities in the same voltage range. Galvanostatic intermittent titration technique (GITT) test was conducted in half cell with a current density of 0.1 A g^{-1} for 5 minutes between rest intervals for 1 hour.

5.2.5. First-principles calculations

All calculation was based on the density functional theory (DFT) performed in Vienna Ab-initio Simulation Package (VASP) and the spin-polarized Perdew-Burke-Ernzerhof (PBE) version of the generalized gradient approximation (GGA) was treated as the exchange-correlation functional, associated with the projector-augmented wave pseudopotential for electron-ion interaction.[144, 145, 216] The Grimme's zero damping DFT-D3 method were further considered in view of the weak van der Waals dispersion forces between the adsorbates and the surfaces. The Monkhorst−Pack k-point sampling of 2 × 2 × 1 was selected for adsorption thermodynamics and density of state calculations, respectively.[147] For the calculations of total energy, a plane-wave kinetic cutoff energy of 400 eV was set to expand the valence electronic states. All atoms were optimized until the Hellman−Feynman force of each atom was lower than 0.05 eV eV $Å^{-1}$. The charge density difference and electron localization function (ELF) were utilized based on the literature.[217]

The adsorption energy (E_{ads}) of sodium atom on the surface of BC3 monolayer with and without defects is computed by

$$E_{ads} = E_{BC3+Na} - E_{BC3} - E_{Na} \quad (5\text{-}1)$$

Where E_{BC3+Na} and E_{BC3} are the computed total energies of the BC3 monolayer with and without sodium atom; E_{Na} represents the total energy (or chemical potential) of sodium atom.

5.3. Results and discussion

5.3.1. Characterizations

BCN sample exhibits the cross-linked and stacked carbon skeleton structure as shown in **Figure 5.2a**. The reason is the hydrogen bonds firstly formed between carboxy groups of critic acid and hydroxyl groups of boron acid, followed by an unavoidable decomposition and continuous structural evolution of precursor during the calcination process. As to the SEM image of PCN sample shown in **Figure 5.2b**, partially overlapped porous three-dimensional nanosheet structure with large pores can be obtained, highlighting the pore-creating function of zinc composites, which is consistent with results from other report.[267] Moreover, for the BPCN sample, similar cross-linked structure of the BCN sample can be observed in **Figures 5.2c,d**, highlighting the unique role of hydrogen bond in inducing the oriented growth of BCN. Additionally, the above-mentioned stacked structure of the BCN sample and overlapped porous structure of the PCN sample can be further confirmed by the TEM images shown in **Figures 5.2e,f**. Interestingly, a hollow and porous structure appears on the BPCN sample as seen from the TEM images **(Figure 5.2g)**. This can be attributed to the formation during annealing process and the disappearance of zinc borate during the etching process.[267, 268] Besides, high-resolution TEM (HR-TEM) image of the BPCN sample shows no obvious crystal lattice, **Figure 5.2h**, indicating its amorphous structure. The uniform distribution of C, B and O elements on the BPCN surface can be also verified by scanning transmission electron microscopy (STEM) image in **Figure 5.2i**.

The X-ray diffraction (XRD) patterns of PCN, BCN and BPCN samples are shown in **Figure 5.3a**. Three samples all show two broad diffraction peaks, corresponding to the (002) and (100) crystal planes of the graphitic structure, respectively.[269] Besides, the intensity ratio of the I_D (1,350 cm^{-1}, disordered or

effective graphite band) and I_G (1,580 cm^{-1}, crystalline graphite band) peaks observed from Raman spectroscopy can be used to evaluate the degree of disorder in the carbon material, **Figure 5.3b**.[270] The similar I_D/I_G values for BPCN, PCN and BCN samples are obtained as 1.00, 1.02, and 0.98, respectively. A relatively high degree of disorder inside the BPCN sample is potentially beneficial for exposing more active sites for fast sodium ions storage by shortening the diffusion distance.

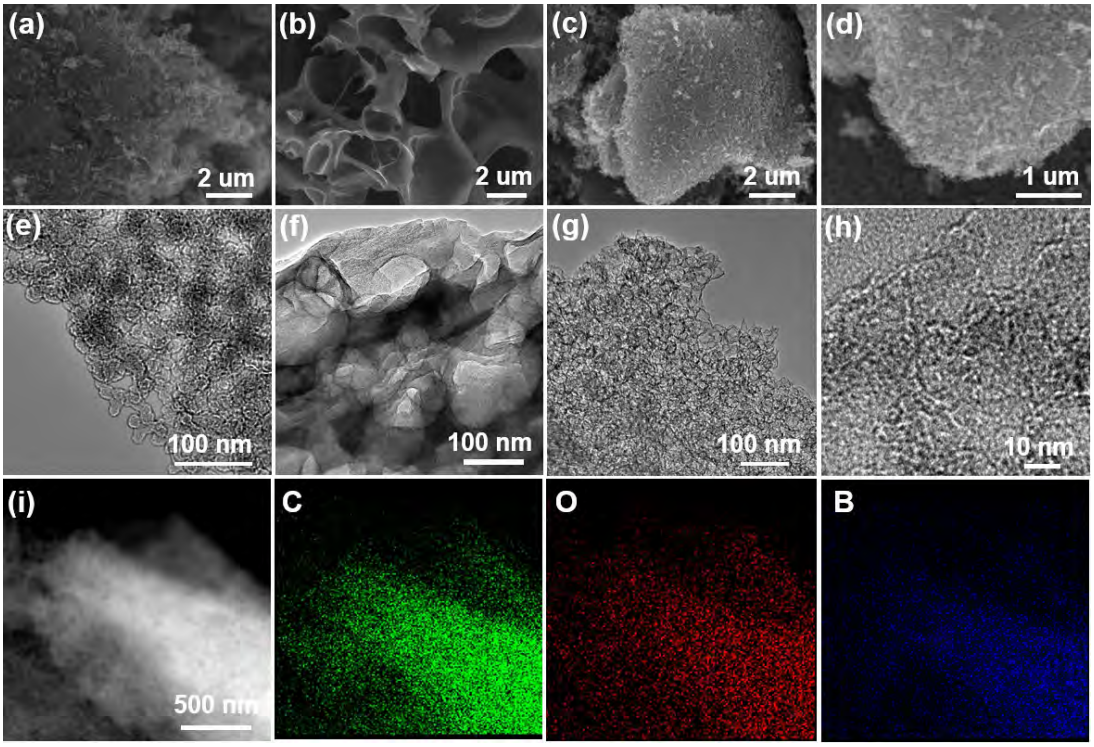

Figure 5.2 FE-SEM images of (a) BCN sample, (b) PCN sample and (c,d) BPCN sample. TEM images of (e) BCN sample, (f) PCN sample and (g,h) BPCN sample. (i) STEM image and corresponding elemental mapping of the BPCN sample.

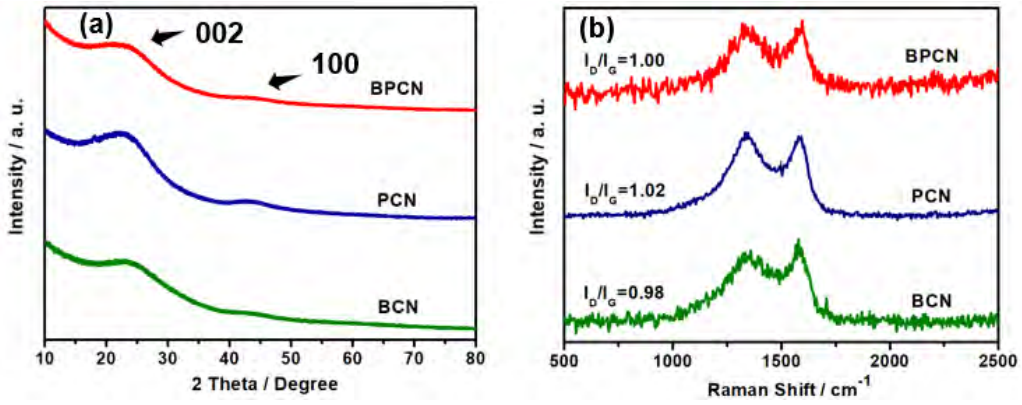

Figure 5.3 (a) XRD patterns, (b) Raman spectra of BPCN and BCN samples.

Additionally, X-ray photoelectron spectrometer (XPS) results are exhibited in **Figures 5.4a,b**. It can be seen that both BCN and BPCN samples include C, B, and O elements while PCN sample only has C and O elements, indicating the successful boron doping into the carbon structure with the addition of boric acid. The corresponding high-resolution XPS spectra of C 1s are displayed in **Figure 5.4c** where three/four peaks can be found at 284.0, 284.6, 285.9, and 289.1 eV, corresponding to C-B, C-C, C-O, C=O bonds, respectively.[271] Besides, three B 1s peaks (B-C, B-O and B=O bonds) located at 190.6, 191.8 and 193 eV are observed for BPCN and BCN samples (**Figure 5.4d**) where the higher occupancy of B-C bond in the BPCN sample implies more in-plane doping sites in the carbon structure compared with BCN sample.[272]

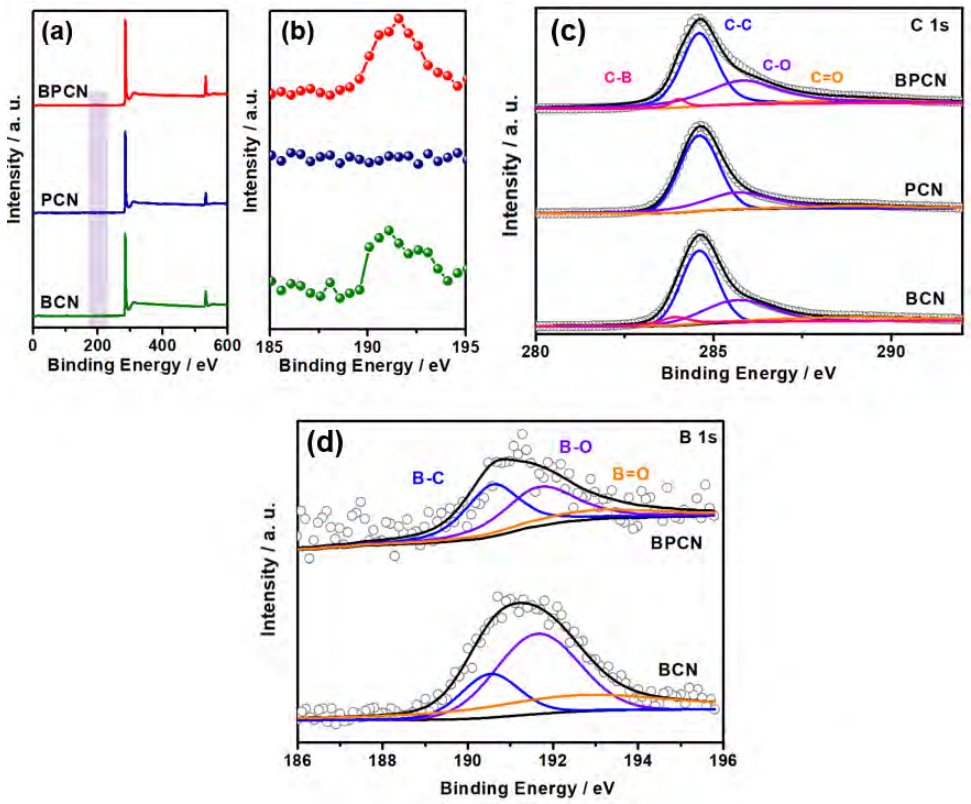

Figure 5.4 (a) XPS survey spectra of BPCN, PCN and BCN sample. (b) Enlarged XPS survey spectra of BPCN, PCN and BCN samples. (c) High-resolution C 1s spectra of BPCN, PCN and BCN samples. (d) High-resolution B 1s spectra of BPCN and BCN samples.

Moreover, the porosity and specific surface area (SSA) information of as-made samples are shown in **Figure 5.5**. Detailly, all the samples display typical adsorption-desorption isotherms of type-I followed with type-IV curves (**Figure 5.5a**), indicating the co-existence of micropore, mesopore and macropore inside the structures.[273] The

SSA of BPCN sample is 698 $m^2 g^{-1}$, which is lower than that of PCN sample (1,644 $m^2 g^{-1}$) and BCN sample (1,187 $m^2 g^{-1}$). However, it should be noted that the mesopore ratio of BPCN sample (~89%) is significantly higher than that of other samples (both are 73%), as presented in **Figure 5.5b**. The reason behind these results can be attributed to the formation of zinc borate composite by the reaction between boric acid and zinc nitrate during calcination, which acts as mesoporous template during further etching process.[268] Such kind of hierarchically porous structure with high mesopore volume inside BPNC framework can not only afford plenty of fast diffusion channels to store sodium ions, but also potentially alleviate the volume change during the sodiumization/desodiumization process.[274] Thus, based on the morphology and composition analysis, it can be expected that the BPCN sample possesses the unique two-dimension mesopore-dominated nanosheet structure coupled with boron doping configuration, which is expected to show a superior sodium ions storage performance.

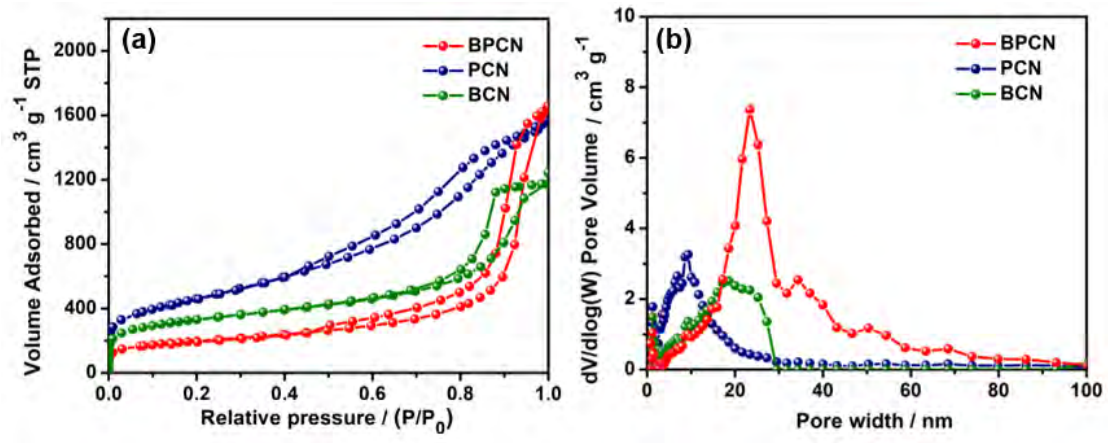

Figure 5.5 (a) Nitrogen adsorption-desorption isotherms and (b) Pore volumes of BPCN, PCN and BCN samples.

5.3.2. Electrochemical performance

The sodium storage properties of as-made samples were firstly tested in half-cell within the potential range of 0.01-3 V (vs Na/Na^+). As shown in **Figure 5.6a**, the first discharge and charge capacities of BPCN electrode are 532.9 and 381.5 mAh g^{-1} at a current density of 0.1 A g^{-1} in 1 M $NaPF_6$/DIGLYDME electrolyte, exhibiting an initial Coulombic efficiency (CE) up to 72%. The capacity lose is due to the irreversible formation of solid electrolyte interphase (SEI) at the interface between the electrode and electrolyte.[275] The high electrode reversibility can be also confirmed by the similar

capacity after 2nd, 5th and10th cycles, and the slight change of discharge line is due to the continuous formation of SEI. To further probe the behavior of BPNC in sodium ions storage, ex-situ Raman spectroscopy measurement was performed (**Figure 5.6b)**. Six points ranging from 0.01V to 3V were selected corresponding to various charge and discharge states and the corresponding curves are displayed in **Figure 5.6c**. The I_D/I_G values were calculated as points corresponding to the right Y-axis and displayed in **Figure 5.6b**. A varying tendency of value was observed, decreasing as voltage drops and increasing as voltage rises. During the discharge process, the disorder degree decreases after the sodium ion interacts with the carbon matrix, and the opposite phenomenon occurs during the charge process. The obtained nearly reversible variation of I_D/I_G values also confirms the highly reversible behavior of BPCN electrode for sodium ions storage.

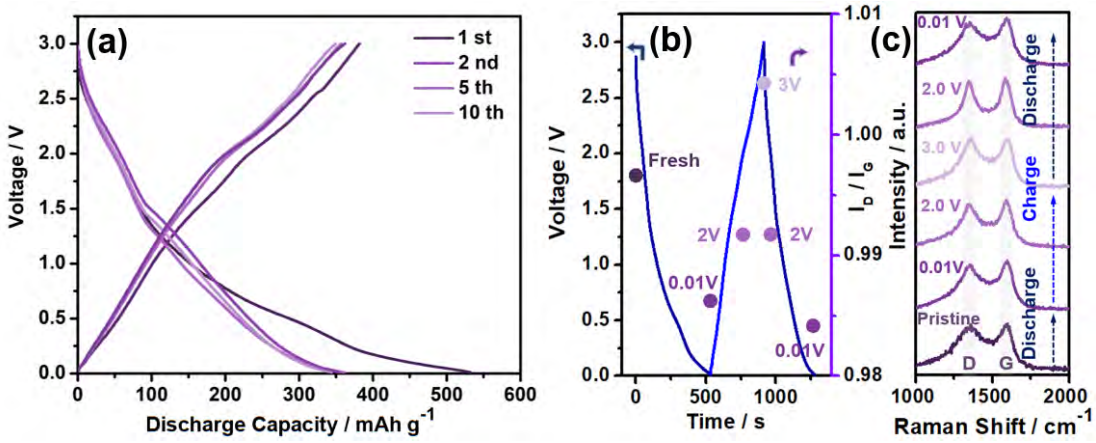

Figure 5.6 (a) The discharge–charge profiles (0.1 A g^{-1}) at the 1st, 2nd, 5th, and 10th cycles of BPCN electrode. (b) Charge and discharge curves of BPCN electrode in the voltage range 0.01–3.0 V and the calculated I_D/I_G values. (c) Ex situ Raman spectra at six selected voltages.

Additionally, the comparable cyclic voltammetry (CV) curves at 0.1 mV s^{-1} are shown in **Figure 5.7**. Several pairs well-defined redox peaks are observed from the CV curves of BCN and BPCN electrodes compared with PCN electrode, which can be mainly attributed to pseudocapacitance derived from boron-doped sites. In order to further understand the effect of boron doping into the carbon matrix on the above CV, five models were built using density functional theory (DFT) method under the consideration of the C basis, vacancy, and three boron states (BC3, BC2O and BCO2) inside the carbon framework (**Figure 5.8a**). The corresponding calculated adsorption energy toward Na^* of these optimized models are summarized in **Figure 5.8b**. It can be

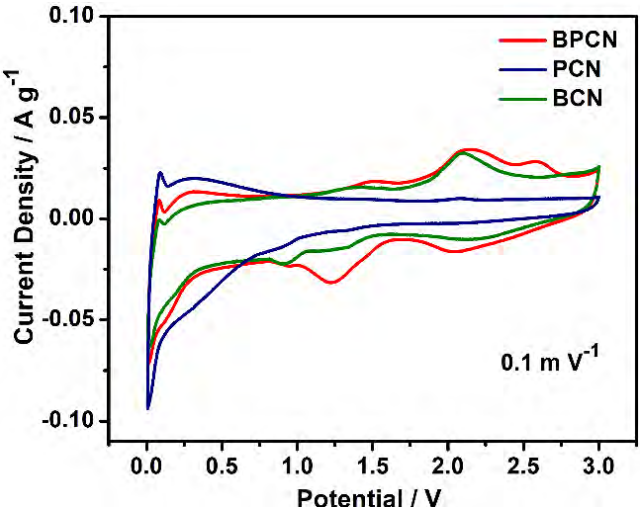

Figure 5.7 The CV curves of BPCN, BCN and PCN at 0.1 mV s^{-1}.

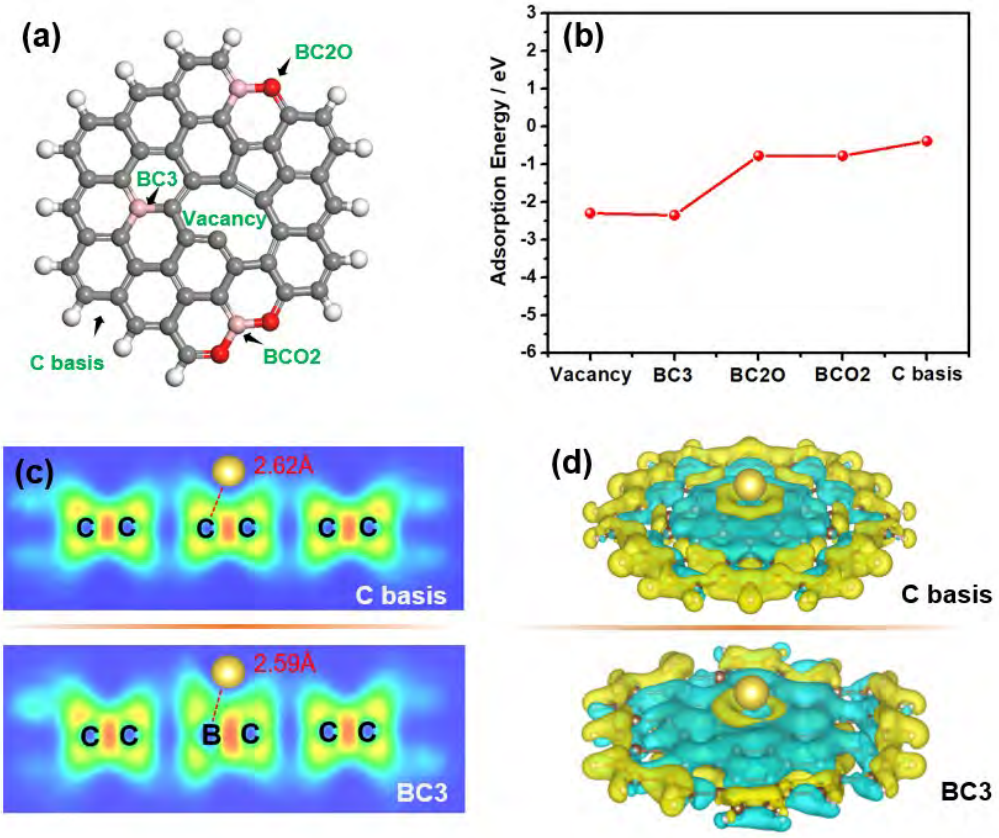

Figure 5.8 (a) The illustration of C basis, BC3, BC2O, BCO2 and vacancy models. (b) Adsorption energies for Na^* on various configuration models. (c) Electron localization function results of Na^* on C basis and BC3 models. (d) The electron density differences of Na^* absorbed on C basis and BC3 models.

concluded that the presence of vacancy and boron-doped sites can largely increase the adsorption energy of Na^* on the corresponding model surface compared to C basis model. Besides, the partially ionic bonding states between Na^* and B/C atoms can be observed from the results of electron localization function (ELF) displayed in **Figure 5.8c**. The distorted shape around boron-doped sites appears with smaller distance (2.59 Å) toward Na^* compared with C basis model (2.62 Å), further confirming the strong adsorption of boron-doped sites for Na^*. Moreover, similar conclusions can be also verified by the electron density differences of C basis model and BC3 model shown in **Figure 5.8d**, where the yellow and blue areas refer to the electron-rich and electron-deficient areas. Many more C atoms cooperate and provide electrons to the Na^* atom from the BC3 model, further creating a strong localization of electron density depletion around the adsorption sites. Thus, it can be speculated that the boron-doped sites can cause unique role on providing additional pseudocapacitance toward sodium ion storage.

The detailed CV and GCD curves of PCN, BCN and BPCN electrodes are presented in **Figure 5.9**. From the results of CV curves, the well retained shapes of as-made electrodes demonstrate the excellent rate performances from 0.1 mV s^{-1} to 2 mV s^{-1}. In addition, the slight offset of curves can be observed especially for BPCN electrode, which is the influence of polarization at high scan rates due to its pseudocapacitance-dominated sodium storage behavior. Besides, one small reduction induced pseudocapacitance. Accordingly, the capacity results calculated from GCD curves are summarized and presented in **Figure 5.10a**, following the order of BPCN (357 mAh g^{-1})>BCN (244 mAh g^{-1})>PCN (183 mAh g^{-1}) at low current density of 0.1 A g^{-1}. The mesopore-dominated pore structure of BPCN electrode combined with rich boron-doped active sites (C-B-*x*, *x* stands for C or O atoms) are expected to provide ample transportation channel and reaction active sites for sodium ions at low current densities, leading to higher capacity. However, the order gradually changes at the subsequent higher current densities (10 A g^{-1}), becoming BPCN (164 mAh g^{-1})>PCN (132 mAh g^{-1})>BCN (71 mAh g^{-1}) at 10 A g^{-1}. The reason behind that is the lower reaction kinetics of the pseudocapacitive process compared with the electric double layer capacitive (EDLC) process. Interestingly, the capacity of PCN electrode exhibits a trend of slight increase and then decrease. This is because the continuous diffusion of sodium ions into/out of the micropore structure makes fully use of active sites, followed by the influence of polarization at high current densities. To obtain more insights into

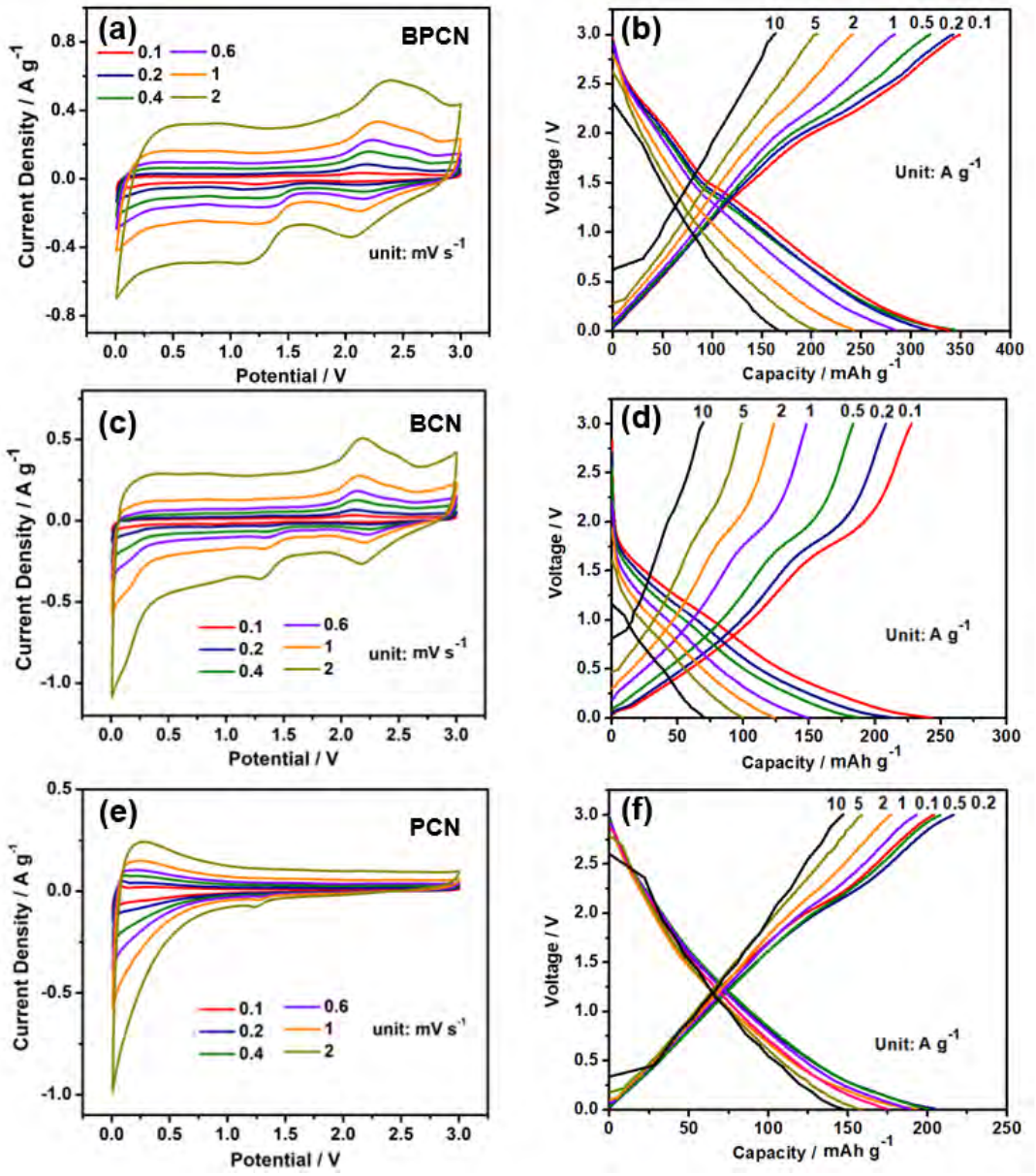

Figure 5.9 (a) CV curves and (b) Charge and discharge curves of BPCN electrode in the half cell. (c) CV curves and (d) Charge and discharge curves of BCN electrode in the half cell. (e) CV curves and (f) Charge and discharge curves of PCN electrode in the half cell.

the electrochemical performances of the cells, electrochemical impedance spectroscopy (EIS) analysis was conducted with results shown in **Figure 5.10b**. The fresh BPCN electrode shows slightly higher interfacial resistance compared to PCN electrode and lower than the BCN electrode, revealing the unique role of ample mesopore channels. With the progress of charge and discharge process, a lower EIS is observed for BPCN electrode due to the continuous activation of carbon-based materials.[276, 277] Besides, the BPCN electrode displays an excellent cycling performance with a capacity retention

of 320 mAh g^{-1} after 1,000 cycles at 1 A g^{-1}, indicating a high reversible reaction with sodium ions and the structural stability of the electrode material, as displayed in **Figure 5.11**.[278] The retained capacity of PCN and BCN electrodes after 1,000 cycles are 200 and 150 mAh g^{-1}, respectively. The slight increase in capacity can be observed during the cycling test of BPCN electrode, which can be assigned to the intrinsic mesopore-dominated structure with shortened transport routes and typical electrochemical activation of anodes for sodium ion storage application.[279, 280] On the contrary, the capacity of PCN electrode decreases initially and then increases during the cycling test. Because the micropore-dominated structure can provide more accessible area for the formation of SEI at high current density, leading to slight decrease in capacity at initial cycling followed with typical activation process of carbon-based material. In addition, suitable porosity structure of BCN associated with boron-doped composition make it stable during cycling, although the capacity is relatively low among the electrodes.

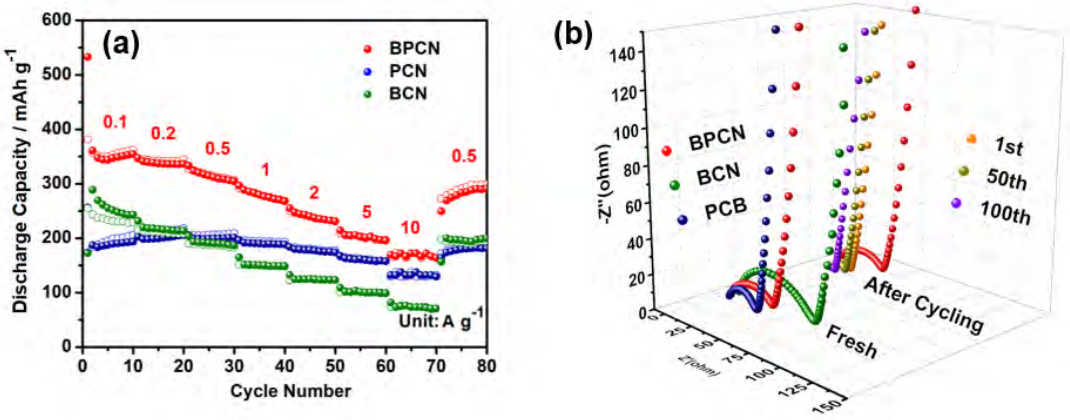

Figure 5.10 (a) Rate performances of BPCN, BCN and PCN electrodes at different current densities. (b) EIS curves of BPCN, PCN and BCN electrodes in half cells (the inset: EIS curves of BPCN electrode after different cycles).

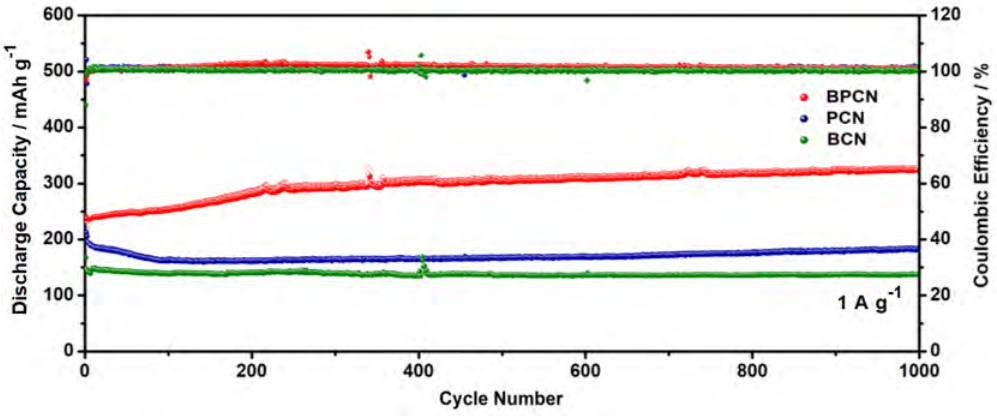

Figure 5.11 Long cyclic performance of BPCN, BCN and PCN electrodes at 1 A g^{-1} for 1,000 cycles.

5.4. Kinetics analysis

To reveal the role of porous structure in improving the kinetics of Na^+ migration, the sodium-ions diffusion coefficients (D_{Na}) of as-made electrodes are estimated by the galvanostatic intermittent titration technique (GITT).[281] The representative voltage responses of BPCN, PCN and BCN electrodes during sodiumization processes are displayed in **Figure 5.12.** It can be seen that the less potential change is observed for BPCN electrode during each relaxation process, corresponding to the lower overpotential for the charge/discharge period. The larger D_{Na} value of BPCN is obtained compared to the PCN and BCN electrodes, indicating its faster diffusion kinetics derived from the unique mesopore-dominated structure. Note that a decreasing tendency of D_{Na} during discharge process can be also observed because of the increased resistance for the adsorbed Na^+ on the near surface region of the electrode diffusing farther into the material interior.

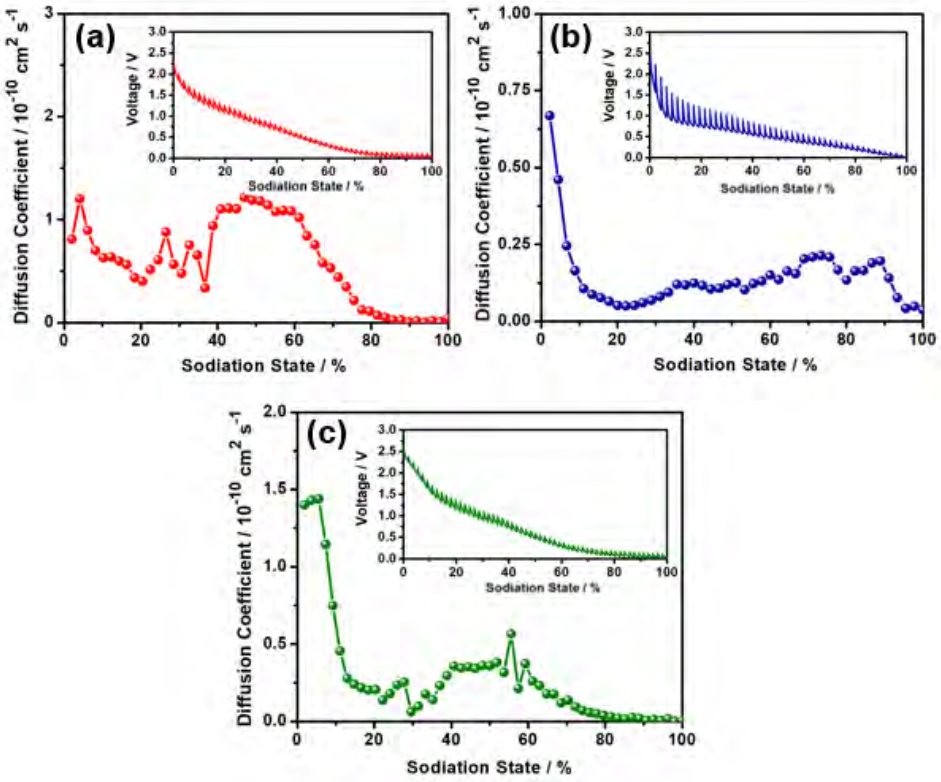

Figure 5.12 GITT and diffusion coefficient profiles of (a) BPCN, (b) PCN, and BCN electrodes.

Further, the log(*i*)-log(*v*) plots of as-made electrodes for the current values obtained from typical oxidation/reduction peaks show a linear relationship with the

logarithm of scan rate as shown in **Figure 5.13**.[282] The values of the slope, *b*, would show the sodium ions storage mechanism in terms of the capacitive or diffusion-controlled contribution. Typically, *b* approaching to 0.5 represents a mainly diffusion-dominated manner, while closing to 1.0 indicates a capacitive dominated situation. The obtained *b* values of BPCN electrode are 0.92 and 0.97 for cathodic peak (Peak 1) and anodic peak (Peak 2), respectively, which are higher than that of PCN electrode (0.77 for Peak 1, 0.73 for Peak 2), elucidating that more pseudocapacitive behavior appears

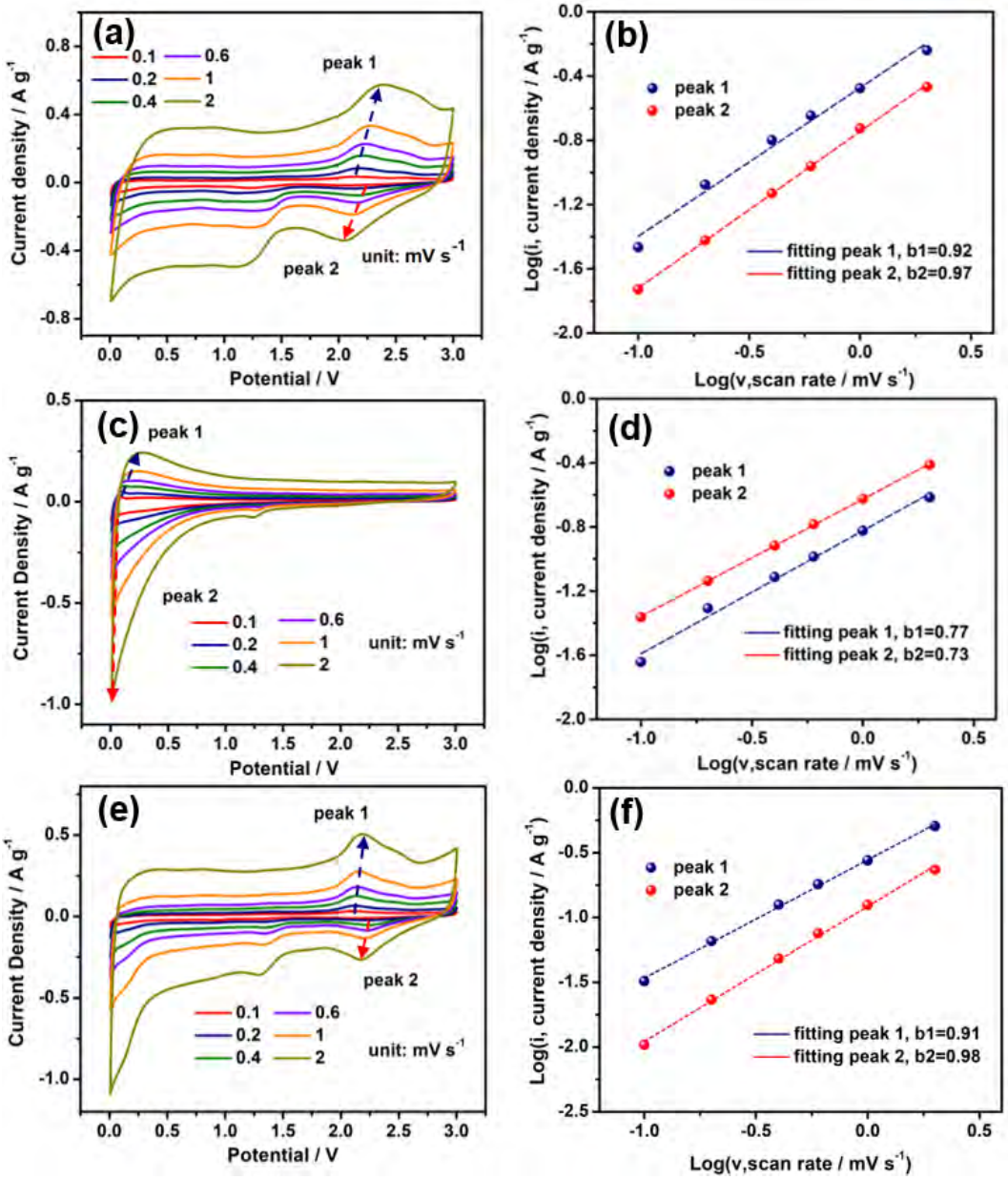

Figure 5.13 CV curves with scan rates from 0.1 to 2 mV s^{-1} and log (*i*) versus log (*v*) plots at selected peak currents of (a,b) BPCN, (c,d) PCN and (e,f) BCN electrodes.

and occupies the predominate position of BPCN electrode for the sodium-ions storage. Besides, the BCN electrode (0.91 for Peak 1, 0.98 for Peak 2) shows nearly similar *b* values to the BPCN, indicating the unique boron-doped sites for improving the pseudocapacitance.

Quantitatively, the capacitive contribution to the overall capacity can be also calculated using Equation below:

$$i = k_1 v + k_2 v^{1/2} \quad (5\text{-}2)$$

where $k_1 v$ and $k_2 v^{1/2}$ stands for the capacitive and diffusion reaction respectively.[282] As shown in **Figure 5.14**, the PCN electrode shows a 34.1% capacitive contribution at 0.2 mV s^{-1}, suggesting its diffusion-dominated process. In comparison, the BPCN

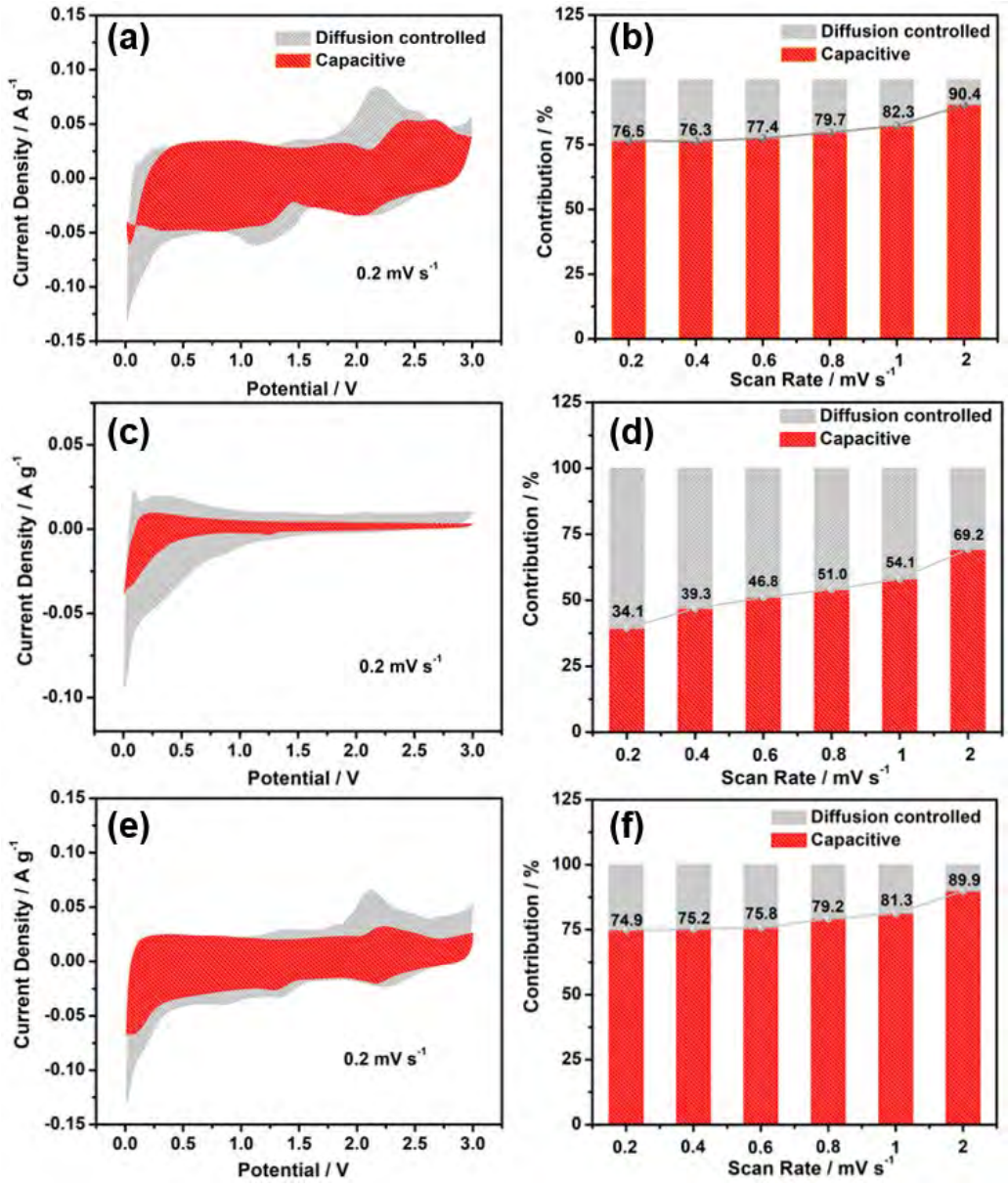

Figure 5.14 Capacitive and diffusion-controlled contribution at 0.2 mV s^{-1} of (a) BPCN,

(c) PCN and (e) BCN electrodes. Capacitive and diffusion-controlled contributions at various scan rates of (b) BPCN, (d) PCN and (f) BCN electrodes.

electrode (76.5%) and BCN electrode (74.9%) exhibit higher capacitive contributions at the same scan rate. Besides, the capacitive contributions for the BPCN electrode increases from 76.5% to 90.4% from 0.2 to 2 mV s^{-1}, which are significantly larger than PCN electrode at similar scan rates (39.4% to 69.2%). Thus, it is considered that the synergetic effect between porous carbon structure coupled with multiple boron-doped active sites can reversibly capture more sodium-ions by surface pseudocapacitive reaction in BPCN electrode, thus enhancing the surface pseudocapacitive contribution.

5.5. Sodium ion capacitors performance

It is demonstrated that the benefit of the synergistic effect of the mesopore-dominated porous structure and ample boron-doped sites inside BPCN electrode shows excellent ions diffusion kinetics, low charge-transfer resistance, and also exhibits high specific capacity and stable cycling stability. Thus, high-performance sodium ion capacitors (SICs) is to be expected. For positive electrode, the commercial activated carbon (AC, YP-50) is selected and tested in a half-cell. The summarized charge and discharge curves are presented in **Figure 5.15a.** It can be seen that significant reversible

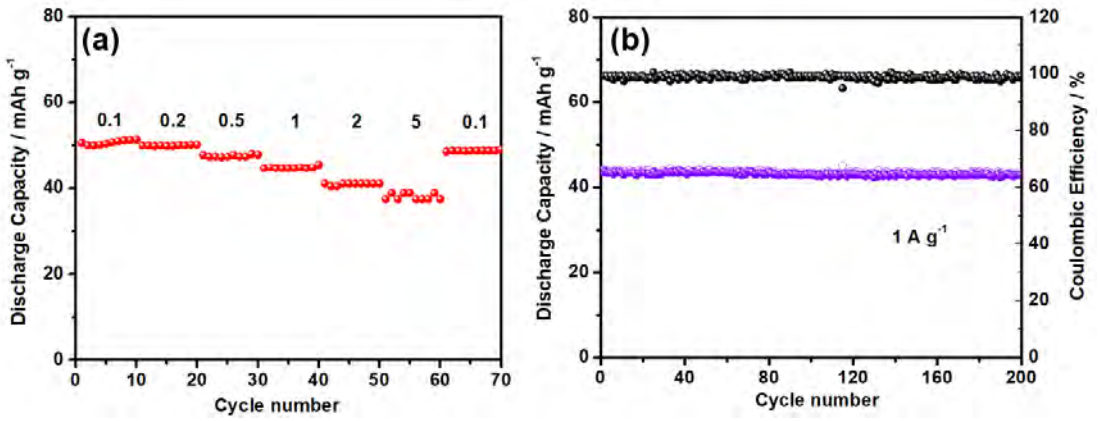

Figure 5.15 (a) Rate performance of YP-50 electrode at different current densities. (b) Long cyclic performance of YP-50 electrode at 1 A g^{-1} for 200 cycles.

capacity of 50.6 and 37.5 mAh g^{-1} for AC electrode can be achieved at 0.1 and 5 A g^{-1}, respectively. Moreover, the AC electrode shows a high capacity retention of 100% and high Coulombic efficiency of about 100% over 200 cycles at 1 A g^{-1}, **Figure 5.15b**,

manifesting the advantages of AC electrode with both highly reversible sodium-ion storage capability and good cycling stability. Thus, a SICs using BPCN as a negative electrode and AC as a positive electrode was assembled for its performance test. It is denoted as BPCN//AC.

As the scheme diagram shown in **Figure 5.16a**, the PF_6^- anions are absorbed in the porous surface of the positive electrode (AC), and at the same time the Na^+ cations are intercalated/absorbed into/on the negative electrode (BPNC) during the charging process. The discharge process of the SICs is the reverse process. **Figure 5.16b,c** respectively display the CV and GCD curves of the BPCN//AC. The nearly straight lines with no visible redox peak indicate that the storage mechanism is primarily governed by capacitive-controlled behavior with a certain degree of pseudocapacitance, which can be ascribed to the abundant boron doping sites and surface defects. In **Figure 5.17a**, BPCN//AC displays a high specific capacity of 32.3 mAh g^{-1} at 0.2 A g^{-1} and maintains 13.9 mAh g^{-1} even at an ultra-high current density of 5 A g^{-1}. Furthermore, the BPCN//AC full capacitor displays a high energy density of 64.8 Wh kg^{-1} at 0.1 A g^{-1} and maintains 30.5 Wh kg^{-1} even at an ultra-high current density of 5 A g^{-1} as exhibited in **Figure 5.17b**, which is much higher than the similar reported results.[240, 283-287] The superior rate performance of BPCN//AC is a result of the similar sodium ions storage mechanism of the negative and positive electrodes. The above SICs can maintain ~80% capacity compared with its initial value after 1,500 cycles at 1.0 A g^{-1}, as well as a nearly 100% CE, **Figure 5.17c**. The initial fluctuation of capacity is due to the continuous matching process of both sides to a stable state. These results show a promising future storage device with high energy/power density and long cycling life.

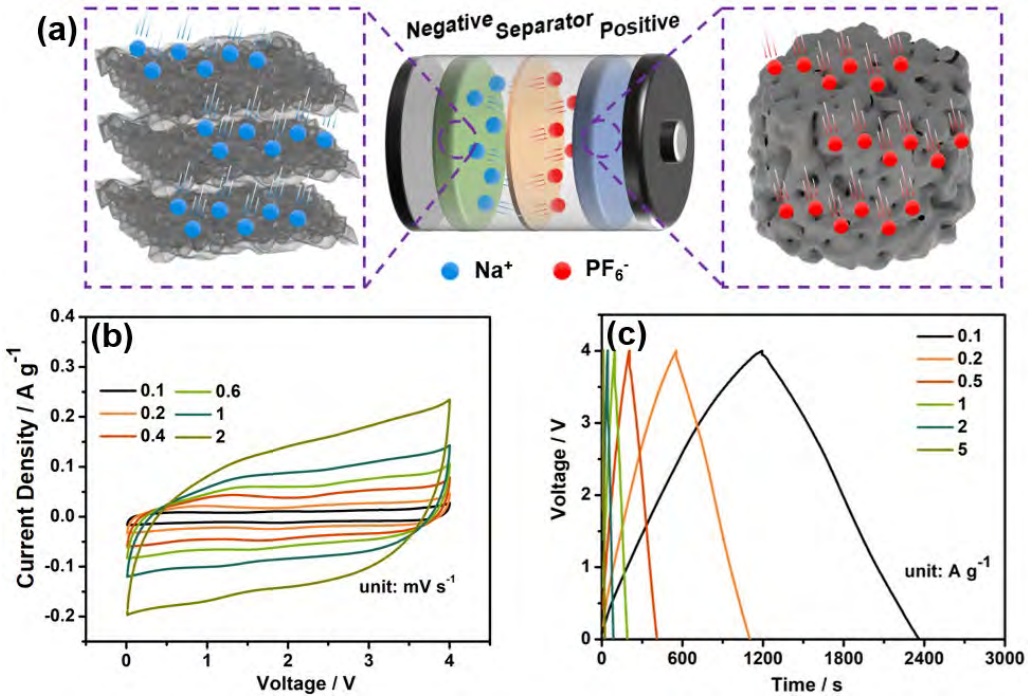

Figure 5.16 Electrochemical performance of BPCN//AC: (a) Schematic illustration, (b) CV curves and (c) GDC curves.

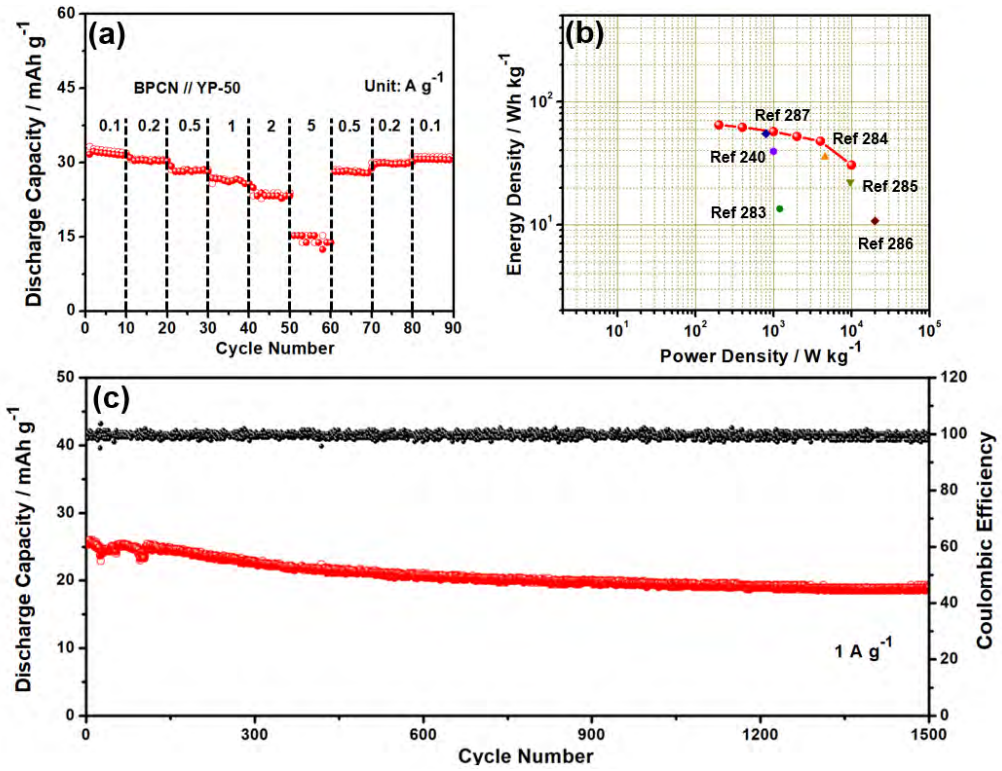

Figure 5.17 Electrochemical performance of BPCN//AC: (a) Rate performance, (b) Ragone plots of BPCN//AC with others (c) Long cyclic performance of BPCN//AC at 1.0 A g^{-1} for 1,500 cycles.

5.6. Summary

In summary, a mesopore-dominated porous carbon nanosheet structure was synthesized with boron doping configuration. The resulted BPCN electrode exhibits significant sodium ions storage performance in terms of high reversible capacity, fast-rate capability as well as long cycling stability. Ex-situ Raman and electrochemical results indicate that BPCN electrode has a reversible sodiation/desodiation reaction during discharge/charge process, benefiting for high structural and cycling stability. Accordingly, the obtained BPCN electrode delivers high capacities of 357 mAh g^{-1} and 164 mAh g^{-1} at 0.1 A g^{-1} and 10 A g^{-1}, respectively. Further analysis of the experimental and DFT results show that the introduced *p*-type boron doping sites can also generate a strong adsorption region for sodium ions, thereby increasing pseudocapacitive capacity from 36% to 76% to replace insertion/desertion process which is not resistant to high current densities. By pairing with commercial YP-50 carbon material as positive electrode, the full sodium ion capacitor can be optimized to deliver a maximum specific capacity of 64.8 Wh kg^{-1} and a good cycling retention of 80% after 1,500 cycles at 1 A g^{-1}.

Chapter 6 Conclusion

6.1. Contributions to knowledge

In the present study, carbon-based materials were fabricated and investigated for high-performance supercapacitors application. Through the structural design, interface and composite modification, new electrode materials with micro/nanostructures have been successfully prepared to match various electrolytes from aqueous to organic solutions. The corresponding energy density of supercapacitors has been successfully increased by optimizing the electrode and electrolyte configuration. New concepts have been presented for both theoretical research and industrial design. The following contributions to knowledge have been made:

(1) Tuning the active sites of carbon surface for boosting redox chemistry of redox additives in aqueous electrolyte:

It is generally accepted that the energy density of supercapacitors using carbon electrodes can be largely enhanced by introducing additional redox species from the electrolytes. However, the relationship between the redox chemistry of electrolytes and carbon surfaces is still undefined, leading to unsatisfactory supercapacitor performance.

Herein, nitrogen-doped carbon nanosheet were developed by controlling the annealing temperature from 600 ^{o}C to 1000 ^{o}C, and tested in the aqueous iodide (I^{-}/I_3^{-}) electrolyte (2 M $NaSO_4$ +0.05 M KI). The experimental and theoretical investigations reveal that not only the considerable influence of the porosity, but the graphitic N content on the carbon scaffolds can also accelerate the redox kinetics of the I^{-}/I_3^{-} couple, thus enabling excellent rate capability of carbon-based electrodes for supercapacitor. Accordingly, the sample prepared at 900 ^{o}C annellation exhibited the highest energy and power densities of 22.4 Wh kg^{-1} as well as excellent stability of 96.5% capacitance retention after 30,000 charging/discharging cycles.

(2) Constructing conductive PEDOT skin onto nickel cobalt layer double hydroxides/carbon fiber for achieving hybrid design of high-performance supercapacitor in aqueous electrolyte:

Aiming to tackle restrain of working voltage in aqueous electrolyte, hybrid design of supercapacitors combined with capacitive negative electrode and pseudocapacitive-type positive electrode is considered as the most promising strategy. However, the low

rate capability and cycling stability of positive sides still limit the wide application of such configuration.

Herein, from the perspective of interface modification, carbon fiber was firstly chosen as substrate for the deposition of nickel cobalt layer double hydroxide (NiCoLDH) nanosheets to increase the active sites of the electrode material. Further, thin PEDOT skin was constructed onto the NiCoLDH nanosheets by oCVD method, inducing high electron conductivity coupled with ionically permeable characteristics. Combined with COMSOL and DFT stimulation, the presence of PEDOT layer can both mediate the charge distribution of electron among the surface of NiCoLDH and accelerate the redox reaction of NiCoLDH with OH^- ions. Thus, the resulted PEDOT coated electrode material exhibited a higher rate capability (79% retention from 1 A g^{-1} to 50 A g^{-1}) and cycling stability (92% retention for 6,000 cycles at 10 A g^{-1}) compared to the uncoated electrode material (55% retention from 1 A g^{-1} to 50 A g^{-1}, 70% retention for 6,000 cycles at 10 A g^{-1}). Additionally, the assembled asymmetrical supercapacitor can deliver a high energy density up to 58 Wh kg^{-1} and 80% capacitance retention for 6,000 cycles at 5 A g^{-1}.

(3) Introducing boron-doped active sites into porous carbon framework for matching capacitive cathode by increasing slope capacity contribution in organic electrolyte:

Replacing aqueous electrolyte with organic one can greatly expand working voltage window of a supercapacitor, leading to potentially high energy density of metal ion capacitor. However, the low reaction dynamics of battery-type anode cannot match well with capacity-type cathode, owing to the insertion/desertion dominated process of plating region.

With the above analysis, a new and facile strategy is proposed here to fabricate boron-doped porous carbon nanosheet material (BPCN) with the aid of H_3BO_3 as boron source while zinc nitrate hexahydrate as pore-forming agent. By investigating multiple characteristic measurements, kinetic analysis and DFT calculations, the mesopore-dominated porous structure combined with ample boron-doped sites are employed as anchoring sites for sodium ions to promote pseudocapacitive capacity during the charge and discharge process. Thus, the obtained electrode delivered a high capacity of 357 mAh g^{-1} at 0.1 A g^{-1} and a superior long cycle performance can be also achieved after 1,000 cycles under 320 mAh g^{-1} at 1 A g^{-1} in half cell. In addition, the assembled

sodium ion capacitors exhibited a maximum specific capacity of 64.8 Wh kg^{-1} and a good cycling retention of 80% after 1,500 cycles at 1 A g^{-1}.

6.2. Recommendations for future work

(1) Carbon-based electrode material used in aqueous electrolyte with redox species.

Carbon-based materials with different morphologies and compositions have shown much potential on obtaining high-performance electrodes for supercapacitors using various redox electrolytes. However, the optimization of carbon configuration with additional catalytic sites to boost the capacitance from redox species is still neglected and missing. Thus, the precious/non-precious metals and their compounds can be considered to be introduced into the carbon framework, providing many opportunities to obtain high-performance supercapacitor. Additionally, the design and selection of suitable redox species is another key to boost electrochemical performance, including V^{3+}/V^{2+}, Fe^{3+}/Fe^{2+}, $S_2O_8^{2-}/SO_4^{2-}$ and Br^-/Br_3^-, etc. The combination of two kinds of redox species also exhibits potential application due to their different redox potential, resulting in overlap of redox peaks to improve the final performance.

(2) Carbon-based electrode material used in aqueous electrolyte with hybrid design of supercapacitors.

Utilizing pseudocapacitive material to substitute carbon material as positive electrode can achieve hybrid design of supercapacitors, leading to enhanced energy density by expand operation working voltage. The improvement can be considered as two aspects as follow. For the negative side, the design and synthesis of novel carbon-based material with modified surface structure and composition can enlarge adsorption sites of ions or introduce pseudocapacitive sites to improve the corresponding capacitance. For the positive side, the rate and cycling performance of electrode material are two key aspect needed to be solved. Rational selection of synthesis strategy combined with structural design can intrinsically optimize the activity and structural stability of electrode material at atomic level. Besides, the controllable and accurate interface modification can also enhance the final electrochemical performance owing to the synergy among two kinds of composition. Based on the above discussion, the

obtained hybrid supercapacitors can tackle the limitation of energy density in aqueous electrolyte while maintaining high-rate and long cycling stability characteristics.

(3) Carbon-based electrode material used in organic electrolyte for sodium ion capacitors.

Different from aqueous electrolyte, the low diffusion dynamics of ions during the energy storage process still restrain the rate and cycling performance. Thus, the structural design and composition optimization of carbon anode materials are undoubtedly the key factors to improve the overall performance of the device. On the one hand, how to organically combine the interlayer spacing, pore volume, and pore size distribution of carbon-based materials with solvation/desolvation ions to increase the conduction rate of sodium ions and electrons in the structure. On the other hand, how to increase the electrochemical activity of carbon-based electrode materials and expose more active sites to improve their energy storage performance. These issues still need to be gradually explored by future work.

References

[1] X. Luo, J. Wang, M. Dooner, J. Clarke, Overview of current development in electrical energy storage technologies and the application potential in power system operation, Applied Energy, 137, 2015, 511-536.

[2] M. Höök, X. Tang, Depletion of fossil fuels and anthropogenic climate change-a review, Energy Policy, 52, 2013, 797-809.

[3] IEA (2021), IEA Paris, https://www.iea.org/reports/oil-2021.

[4] F. Perera, Pollution from fossil-fuel combustion is the leading environmental threat to global pediatric health and equity: Solutions exist, International Journal of Environmental Research and Public Health, 15, 2018, 16.

[5] S.R. Bull, Renewable energy today and tomorrow, Proceedings of the IEEE, 89, 2001, 1216-1226.

[6] L. Yu, G.Z. Chen, Supercapatteries as high-performance electrochemical energy storage devices, Electrochemical Energy Reviews, 3, 2020, 271-285.

[7] E. Quaranta, R. Revelli, Performance characteristics, power losses and mechanical power estimation for a breastshot water wheel, Energy, 87, 2015, 315-325.

[8] M.A.G.d. Brito, L.P. Sampaio, L.G. Junior, C.A. Canesin, Research on photovoltaics: Review, trends and perspectives, XI Brazilian Power Electronics Conference, leee, 2011, 531-537.

[9] S. Jaisankar, J. Ananth, S. Thulasi, S.T. Jayasuthakar, K.N. Sheeba, A comprehensive review on solar water heaters, Renewable and Sustainable Energy Reviews, 15, 2011, 3045-3050.

[10] J. Yan, X. Liao, D. Yan, Y. Chen, Review of micro thermoelectric generator, Journal of Microelectromechanical Systems, 27, 2018, 1-18.

[11] Y. Shao, M.F. El-Kady, J. Sun, Y. Li, Q. Zhang, M. Zhu, H. Wang, B. Dunn, R.B. Kaner, Design and mechanisms of asymmetric supercapacitors, Chemical Reviews, 118, 2018, 9233-9280.

[12] Z.P. Cano, D. Banham, S. Ye, A. Hintennach, J. Lu, M. Fowler, Z. Chen, Batteries and fuel cells for emerging electric vehicle markets, Nature Energy, 3, 2018, 279-289.

[13] W. Zuo, R. Li, C. Zhou, Y. Li, J. Xia, J. Liu, Battery-supercapacitor hybrid devices: Recent progress and future prospects, Advanced Science, 4, 2017, 1600539.

[14] M. Aneke, M. Wang, Energy storage technologies and real life applications-a state of the art review, Applied Energy, 179, 2016, 350-377.

[15] F. Díaz-González, A. Sumper, O. Gomis-Bellmunt, R. Villafáfila-Robles, A review of energy storage technologies for wind power applications, Renewable and Sustainable Energy Reviews, 16, 2012, 2154-2171.

[16] E. Rivard, M. Trudeau, K. Zaghib, Hydrogen storage for mobility: A review, Materials, 12, 2019, 1973.

[17] L. Mauler, F. Duffner, W.G. Zeier, J. Leker, Battery cost forecasting: A review of methods and results with an outlook to 2050, Energy & Environmental Science, 14, 2021, 4712-4739.

[18] S. Kumar, A. Jaswal, A. Pandey, N.J.I.R.J.o.E. Sharma, Technology, Literature review of dam break studies and inundation mapping using hydraulic models and GIS, International Research Journal of Engineering and Technology, 4, 2017, 55-61.

[19] P. Simon, Y. Gogotsi, Materials for electrochemical capacitors, Nature Materials, 7, 2008, 845-854.

[20] C. Zhong, Y. Deng, W. Hu, J. Qiao, L. Zhang, J. Zhang, A review of electrolyte materials and compositions for electrochemical supercapacitors, Chemical Society Reviews, 44, 2015, 7484-7539.

[21] R.R. Salunkhe, Y.V. Kaneti, Y. Yamauchi, Metal–organic framework-derived nanoporous metal oxides toward supercapacitor applications: Progress and prospects, ACS Nano, 11, 2017, 5293-5308.

[22] Q. Meng, K. Cai, Y. Chen, L. Chen, Research progress on conducting polymer based supercapacitor electrode materials, Nano Energy, 36, 2017, 268-285.

[23] A. Borenstein, O. Hanna, R. Attias, S. Luski, T. Brousse, D. Aurbach, Carbon-based composite materials for supercapacitor electrodes: A review, Journal of Materials Chemistry A, 5, 2017, 12653-12672.

[24] W. Raza, F. Ali, N. Raza, Y. Luo, K.-H. Kim, J. Yang, S. Kumar, A. Mehmood, E.E. Kwon, Recent advancements in supercapacitor technology, Nano Energy, 52, 2018, 441-473.

[25] H.I. Becker, US Pat., 2800616, 1957.

[26] R.A. Rightmire, US Pat., 3288641, 1966.

[27] S. Trasatti, G. Buzzanca, Ruthenium dioxide: A new interesting electrode material. Solid state structure and electrochemical behaviour, Journal of Electroanalytical Chemistry and Interfacial Electrochemistry, 29, 1971, A1-A5.

[28] D.A. Evans, J.R. Miller, Hybrid electrolytic/electrochemical capacitor for electric vehicles, Proceedings of the Symposium on Electrochemical Capacitors Ii, 96, 1997, 253-257.

[29] J.W. Long, T. Brousse, D. Bélanger, Electrochemical capacitors: Fundamentals to applications, Journal of the Electrochemical Society, 162, 2015, Y3-Y3.

[30] Y. Gong, D. Li, C. Luo, Q. Fu, C. Pan, Highly porous graphitic biomass carbon as advanced electrode materials for supercapacitors, Green Chemistry, 19, 2017, 4132-4140.

[31] A. Muzaffar, M.B. Ahamed, K. Deshmukh, J. Thirumalai, A review on recent advances in hybrid supercapacitors: Design, fabrication and applications, Renewable and Sustainable Energy Reviews, 101, 2019, 123-145.

[32] B. Yao, H. Wang, Q. Zhou, M. Wu, M. Zhang, C. Li, G. Shi, Ultrahigh-conductivity polymer hydrogels with arbitrary structures, Advanced Materials, 29, 2017, 1700974.

[33] J. Li, X. Yuan, C. Lin, Y. Yang, L. Xu, X. Du, J. Xie, J. Lin, J. Sun, Achieving high pseudocapacitance of 2D titanium carbide (MXene) by cation intercalation and surface modification, Advanced Energy Materials, 7, 2017, 1602725.

[34] J. Li, Z. Liu, Q. Zhang, Y. Cheng, B. Zhao, S. Dai, H.-H. Wu, K. Zhang, D. Ding, Y. Wu, M. Liu, M.-S. Wang, Anion and cation substitution in transition-metal oxides nanosheets for high-performance hybrid supercapacitors, Nano Energy, 57, 2019, 22-33.

[35] X. Wu, Y. Xu, Y. Hu, G. Wu, H. Cheng, Q. Yu, K. Zhang, W. Chen, S. Chen, Microfluidic-spinning construction of black-phosphorus-hybrid microfibres for non-woven fabrics toward a high energy density flexible supercapacitor, Nature Communications, 9, 2018, 4573.

[36] N. Jabeen, A. Hussain, Q. Xia, S. Sun, J. Zhu, H. Xia, High-performance 2.6 V aqueous asymmetric supercapacitors based on in-situ formed $Na_{0.5}MnO_2$ nanosheet assembled nanowall arrays, Advanced Materials, 29, 2017, 1700804.

[37] L. Feng, K. Wang, X. Zhang, X. Sun, C. Li, X. Ge, Y. Ma, Flexible solid-state supercapacitors with enhanced performance from hierarchically graphene

nanocomposite electrodes and ionic liquid incorporated gel polymer electrolyte, Advanced Functional Materials, 28, 2018, 1704463.

[38] P. Pazhamalai, K. Krishnamoorthy, S. Manoharan, S.J. Kim, High energy symmetric supercapacitor based on mechanically delaminated few-layered MoS_2 sheets in organic electrolyte, Journal of Alloys and Compounds, 771, 2019, 803-809.

[39] B. Pal, S. Yang, S. Ramesh, V. Thangadurai, R. Jose, Electrolyte selection for supercapacitive devices: A critical review, Nanoscale Advances, 1, 2019, 3807-3835.

[40] C. Zhao, W. Zheng, A review for aqueous electrochemical supercapacitors, Frontiers in Energy Research, 3, 2015, 23.

[41] K. Karuppasamy, J. Theerthagiri, D. Vikraman, C.-J. Yim, S. Hussain, R. Sharma, T. Maiyalagan, J. Qin, H.-S. Kim, Ionic liquid-based electrolytes for energy storage devices: A brief review on their limits and applications, Polymers, 12, 2020, 918.

[42] K.V.G. Raghavendra, R. Vinoth, K. Zeb, C.V.V. Muralee Gopi, S. Sambasivam, M.R. Kummara, I.M. Obaidat, H.J. Kim, An intuitive review of supercapacitors with recent progress and novel device applications, Journal of Energy Storage, 31, 2020, 101652.

[43] L. Zhang, X. Hu, Z. Wang, F. Sun, D.G. Dorrell, A review of supercapacitor modeling, estimation, and applications: A control/management perspective, Renewable and Sustainable Energy Reviews, 81, 2018, 1868-1878.

[44] Poonam, K. Sharma, A. Arora, S.K. Tripathi, Review of supercapacitors: Materials and devices, Journal of Energy Storage, 21, 2019, 801-825.

[45] N. Sudhan, K. Subramani, M. Karnan, N. Ilayaraja, M. Sathish, Biomass-derived activated porous carbon from rice straw for a high-energy symmetric supercapacitor in aqueous and non-aqueous electrolytes, Energy & Fuels, 31, 2017, 977-985.

[46] M. Liu, B. Li, H. Zhou, C. Chen, Y. Liu, T. Liu, Extraordinary rate capability achieved by a 3D “skeleton/skin” carbon aerogel–polyaniline hybrid with vertically aligned pores, Chemical Communications, 53, 2017, 2810-2813.

[47] A.S. Levitt, M. Alhabeb, C.B. Hatter, A. Sarycheva, G. Dion, Y. Gogotsi, Electrospun MXene/carbon nanofibers as supercapacitor electrodes, Journal of Materials Chemistry A, 7, 2019, 269-277.

[48] Z. Yang, J. Tian, Z. Yin, C. Cui, W. Qian, F. Wei, Carbon nanotube- and graphene-based nanomaterials and applications in high-voltage supercapacitor: A review, Carbon, 141, 2019, 467-480.

[49] S. Wang, N. Liu, J. Su, L. Li, F. Long, Z. Zou, X. Jiang, Y. Gao, Highly stretchable and self-healable supercapacitor with reduced graphene oxide based fiber springs, ACS Nano, 11, 2017, 2066-2074.

[50] L.L. Zhang, X.S. Zhao, Carbon-based materials as supercapacitor electrodes, Chemical Society Reviews, 38, 2009, 2520-2531.

[51] J. Hassoun, F. Bonaccorso, M. Agostini, M. Angelucci, M.G. Betti, R. Cingolani, M. Gemmi, C. Mariani, S. Panero, V. Pellegrini, B. Scrosati, An advanced lithium-ion battery based on a graphene anode and a lithium iron phosphate cathode, Nano Letters, 14, 2014, 4901-4906.

[52] Z. Pan, Y. Jiang, P. Yang, Z. Wu, W. Tian, L. Liu, Y. Song, Q. Gu, D. Sun, L. Hu, In-situ growth of layered bimetallic ZnCo hydroxide nanosheets for high-performance all-solid-state pseudocapacitor, ACS Nano, 12, 2018, 2968-2979.

[53] V. Sudha, M.V. Sangaranarayanan, Underpotential deposition of metals: Structural and thermodynamic considerations, The Journal of Physical Chemistry B, 106, 2002, 2699-2707.

[54] E. Herrero, L.J. Buller, H.D. Abruña, Underpotential deposition at single crystal surfaces of Au, Pt, Ag and other materials, Chemical Reviews, 101, 2001, 1897-1930.

[55] M. Sajjad, M. Amin, M.S. Javed, M. Imran, W. Hu, Z. Mao, W. Lu, Recent trends in transition metal diselenides (XSe_2: X = Ni, Mn, Co) and their composites for high energy faradic supercapacitors, Journal of Energy Storage, 43, 2021, 103176.

[56] Q. Wang, S. Wang, J. Li, L. Ruan, N. Wei, L. Huang, Z. Dong, Q. Cheng, Y. Xiong, W. Zeng, A novel aqueous zinc-ion hybrid supercapacitor based on TiS_2 (de)intercalation battery-type anode, Advanced Electronic Materials, 6, 2020, 2000388.

[57] S. Liu, Y. Yin, M. Wu, K.S. Hui, K.N. Hui, C.-Y. Ouyang, S.C. Jun, Phosphorus-mediated MoS_2 nanowires as a high-performance electrode material for quasi-solid-state sodium-ion intercalation supercapacitors, Small, 15, 2019, 1803984.

[58] H. Wang, C. Zhu, D. Chao, Q. Yan, H.J. Fan, Nonaqueous hybrid lithium-ion and sodium-ion capacitors, Advanced Materials, 29, 2017, 1702093.

[59] D. Tie, S. Huang, J. Wang, J. Ma, J. Zhang, Y. Zhao, Hybrid energy storage devices: Advanced electrode materials and matching principles, Energy Storage Materials, 21, 2019, 22-40.

[60] Z. Bi, Q. Kong, Y. Cao, G. Sun, F. Su, X. Wei, X. Li, A. Ahmad, L. Xie, C.-M. Chen, Biomass-derived porous carbon materials with different dimensions for supercapacitor electrodes: A review, Journal of Materials Chemistry A, 7, 2019, 16028-16045.

[61] T. Liu, F. Zhang, Y. Song, Y. Li, Revitalizing carbon supercapacitor electrodes with hierarchical porous structures, Journal of Materials Chemistry A, 5, 2017, 17705-17733.

[62] I.I.G. Inal, S.M. Holmes, A. Banford, Z. Aktas, The performance of supercapacitor electrodes developed from chemically activated carbon produced from waste tea, Applied Surface Science, 357, 2015, 696-703.

[63] H. Yi, K. Nakabayashi, S.-H. Yoon, J. Miyawaki, Pressurized physical activation: A simple production method for activated carbon with a highly developed pore structure, Carbon, 183, 2021, 735-742.

[64] N.A. Rashidi, S. Yusup, Recent methodological trends in nitrogen–functionalized activated carbon production towards the gravimetric capacitance: A mini review, Journal of Energy Storage, 32, 2020, 101757.

[65] E. Elaiyappillai, R. Srinivasan, Y. Johnbosco, P. Devakumar, K. Murugesan, K. Kesavan, P.M. Johnson, Low cost activated carbon derived from cucumis melo fruit peel for electrochemical supercapacitor application, Applied Surface Science, 486, 2019, 527-538.

[66] F. Cheng, X. Yang, S. Zhang, W. Lu, Boosting the supercapacitor performances of activated carbon with carbon nanomaterials, Journal of Power Sources, 450, 2020, 227678.

[67] S. Zhang, X. Shi, R. Wróbel, X. Chen, E. Mijowska, Low-cost nitrogen-doped activated carbon prepared by polyethylenimine (PEI) with a convenient method for supercapacitor application, Electrochimica Acta, 294, 2019, 183-191.

[68] H. Pan, J. Li, Y. Feng, Carbon nanotubes for supercapacitor, Nanoscale Research Letters, 5, 2010, 654.

[69] P. Kanninen, N.D. Luong, L.H. Sinh, I.V. Anoshkin, A. Tsapenko, J. Seppälä, A.G. Nasibulin, T. Kallio, Transparent and flexible high-performance supercapacitors based on single-walled carbon nanotube films, Nanotechnology, 27, 2016, 235403.

[70] G. Wang, Y. Ling, F. Qian, X. Yang, X.-X. Liu, Y. Li, Enhanced capacitance in partially exfoliated multi-walled carbon nanotubes, Journal of Power Sources, 196, 2011, 5209-5214.

[71] J. Xia, F. Chen, J. Li, N. Tao, Measurement of the quantum capacitance of graphene, Nature Nanotechnology, 4, 2009, 505-509.

[72] G. Zhang, Y. Song, H. Zhang, J. Xu, H. Duan, J. Liu, Radially aligned porous carbon nanotube arrays on carbon fibers: A hierarchical 3D carbon nanostructure for high-performance capacitive energy storage, Advanced Functional Materials, 26, 2016, 3012-3020.

[73] Y. Zhang, Y.-W. Tan, H.L. Stormer, P. Kim, Experimental observation of the quantum hall effect and berry's phase in graphene, Nature, 438, 2005, 201-204.

[74] M.D. Stoller, S. Park, Y. Zhu, J. An, R.S. Ruoff, Graphene-based ultracapacitors, Nano Letters, 8, 2008, 3498-3502.

[75] K.I. Bolotin, K.J. Sikes, Z. Jiang, M. Klima, G. Fudenberg, J. Hone, P. Kim, H.L. Stormer, Ultrahigh electron mobility in suspended graphene, Solid State Communications, 146, 2008, 351-355.

[76] A.A. Balandin, S. Ghosh, W. Bao, I. Calizo, D. Teweldebrhan, F. Miao, C.N. Lau, Superior thermal conductivity of single-layer graphene, Nano Letters, 8, 2008, 902-907.

[77] C. Lee, X. Wei, W. Kysar Jeffrey, J. Hone, Measurement of the elastic properties and intrinsic strength of monolayer graphene, Science, 321, 2008, 385-388.

[78] H.J.J.o.A.P. Ledbetter, Stainless-steel elastic constants at low temperatures, Journal of Applied Physics, 52, 1981, 1587-1589.

[79] M.P. Down, S.J. Rowley-Neale, G.C. Smith, C.E. Banks, Fabrication of graphene oxide supercapacitor devices, ACS Applied Energy Materials, 1, 2018, 707-714.

[80] W. Zhang, C. Xu, C. Ma, G. Li, Y. Wang, K. Zhang, F. Li, C. Liu, H.-M. Cheng, Y. Du, N. Tang, W. Ren, Nitrogen-superdoped 3D graphene networks for high-performance supercapacitors, Advanced Materials, 29, 2017, 1701677.

[81] M. Cui, X. Meng, Overview of transition metal-based composite materials for supercapacitor electrodes, Nanoscale Advances, 2, 2020, 5516-5528.

[82] T. Wang, F. Yu, X. Wang, S. Xi, K.-J. Chen, H. Wang, Enhancing cycling stability of transition metal-based layered double hydroxides through a self-sacrificial strategy for hybrid supercapacitors, Electrochimica Acta, 334, 2020, 135586.

[83] C.-C. Hu, W.-C. Chen, Effects of substrates on the capacitive performance of $RuO_x \cdot nH_2O$ and activated carbon–RuO_x electrodes for supercapacitors, Electrochimica Acta, 49, 2004, 3469-3477.

[84] C.-C. Hu, K.-H. Chang, M.-C. Lin, Y.-T. Wu, Design and tailoring of the nanotubular arrayed architecture of hydrous RuO_2 for next generation supercapacitors, Nano Letters, 6, 2006, 2690-2695.

[85] L.Y. Chen, Y. Hou, J.L. Kang, A. Hirata, T. Fujita, M.W. Chen, Toward the theoretical capacitance of RuO_2 reinforced by highly conductive nanoporous gold, Advanced Energy Materials, 3, 2013, 851-856.

[86] Y. Yu, H. Wang, H. Zhang, Y. Tan, Y. Wang, K. Song, B. Yang, L. Yuan, X. Shen, X. Hu, Blanket-like $Co(OH)_2$/CoOOH/Co_3O_4/$Cu(OH)_2$ composites on Cu foam for hybrid supercapacitor, Electrochimica Acta, 334, 2020, 135559.

[87] X. Hu, L. Wei, R. Chen, Q. Wu, J. Li, Reviews and prospectives of Co_3O_4-based nanomaterials for supercapacitor application, ChemistrySelect, 5, 2020, 5268-5288.

[88] T. Liu, J. Liu, L. Zhang, B. Cheng, J. Yu, Construction of nickel cobalt sulfide nanosheet arrays on carbon cloth for performance-enhanced supercapacitor, Journal of Materials Science & Technology, 47, 2020, 113-121.

[89] Y. Zhang, Y. Hu, Z. Wang, T. Lin, X. Zhu, B. Luo, H. Hu, W. Xing, Z. Yan, L. Wang, Lithiation-induced vacancy engineering of Co_3O_4 with improved faradic reactivity for high-performance supercapacitor, Advanced Functional Materials, 30, 2020, 2004172.

[90] S. Rafai, C. Qiao, M. Naveed, Z. Wang, W. Younas, S. Khalid, C. Cao, Microwave-anion-exchange route to ultrathin cobalt-nickel-sulfide nanosheets for hybrid supercapacitors, Chemical Engineering Journal, 362, 2019, 576-587.

[91] T. Deng, Y. Lu, W. Zhang, M. Sui, X. Shi, D. Wang, W. Zheng, Inverted design for high-performance supercapacitor via $Co(OH)_2$-derived highly oriented MOF electrodes, Advanced Energy Materials, 8, 2018, 1702294.

[92] G.A. Snook, P. Kao, A.S. Best, Conducting-polymer-based supercapacitor devices and electrodes, Journal of Power Sources, 196, 2011, 1-12.

[93] I. Shown, A. Ganguly, L.-C. Chen, K.-H. Chen, Conducting polymer-based flexible supercapacitor, Energy Science & Engineering, 3, 2015, 2-26.

[94] T.O. Magu, A.U. Agobi, L. Hitler, P.M. Dass, A review on conducting polymers-based composites for energy storage application, Journal of Chemical Reviews, 1, 2019, 19-34.

[95] K. Zhou, Y. He, Q. Xu, Q.e. Zhang, A.a. Zhou, Z. Lu, L.-K. Yang, Y. Jiang, D. Ge, X.Y. Liu, H. Bai, A hydrogel of ultrathin pure polyaniline nanofibers: Oxidant-templating preparation and supercapacitor application, ACS Nano, 12, 2018, 5888-5894.

[96] H. Zhuo, Y. Hu, Z. Chen, L. Zhong, Cellulose carbon aerogel/PPy composites for high-performance supercapacitor, Carbohydrate Polymers, 215, 2019, 322-329.

[97] F. Béguin, V. Presser, A. Balducci, E. Frackowiak, Carbons and electrolytes for advanced supercapacitors, Advanced Materials, 26, 2014, 2219-2251.

[98] P.M. Yeletsky, M.V. Lebedeva, V.A. Yakovlev, Today's progress in the synthesis of porous carbons from biomass and their application for organic electrolyte and ionic liquid based supercapacitors, Journal of Energy Storage, 50, 2022, 104225.

[99] D.R. Joshi, N.J.J.P.R.I. Adhikari, An overview on common organic solvents and their toxicity, 28, 2019, 1-18.

[100] L. Miao, Z. Song, D. Zhu, L. Li, L. Gan, M. Liu, Ionic liquids for supercapacitive energy storage: A mini-review, Energy & Fuels, 35, 2021, 8443-8455.

[101] P.-y. Hung, H. Zhang, H. Lin, Q. Guo, K.-t. Lau, B. Jia, Specializing liquid electrolytes and carbon-based materials in EDLCs for low-temperature applications, Journal of Energy Chemistry, 68, 2022, 580-602.

[102] T. Stettner, A. Balducci, Protic ionic liquids in energy storage devices: Past, present and future perspective, Energy Storage Materials, 40, 2021, 402-414.

[103] H. Liu, H. Yu, Ionic liquids for electrochemical energy storage devices applications, Journal of Materials Science & Technology, 35, 2019, 674-686.

[104] E. Kim, J. Han, S. Ryu, Y. Choi, J. Yoo, Ionic liquid electrolytes for electrochemical energy storage devices, Materials, 14, 2021, 4000.

[105] E.J.R.M.P. Ruska, The development of the electronmicroscope and electron microscopy. Nobel lecture 1986, 59, 1987, 627-638.

[106] S.R. Spurgeon, C. Ophus, L. Jones, A. Petford-Long, S.V. Kalinin, M.J. Olszta, R.E. Dunin-Borkowski, N. Salmon, K. Hattar, W.-C.D. Yang, R. Sharma, Y. Du, A. Chiaramonti, H. Zheng, E.C. Buck, L. Kovarik, R.L. Penn, D. Li, X. Zhang, M. Murayama, M.L. Taheri, Towards data-driven next-generation transmission electron microscopy, Nature Materials, 20, 2021, 274-279.

[107] H. Seiler, Secondary electron emission in the scanning electron microscope, Journal of Applied Physics, 54, 1983, R1-R18.

[108] C.L. Jian Li, Jianhua Lin,Junliang Sun, Application of combining X-ray diffraction and electron crystallography for determination of complex inorganic crystal structure, 36, 2020, 1907052.

[109] G.J.J.o.t.A.C.S. Pickett, Modification of the Brunauer-Emmett-Teller theory of multimolecular adsorption, 67, 1945, 1958-1962.

[110] R.S.J.A.c. Nicholson, Theory and application of cyclic voltammetry for measurement of electrode reaction kinetics, 37, 1965, 1351-1355.

[111] J.C. Puippe, N. Ibl, Influence of charge and discharge of electric double layer in pulse plating, Journal of Applied Electrochemistry, 10, 1980, 775-784.

[112] B.-Y. Chang, S.-M. Park, Electrochemical impedance spectroscopy, Annual Review of Analytical Chemistry, 3, 2010, 207-229.

[113] R. de Levie, On porous electrodes in electrolyte solutions: I. Capacitance effects, Electrochimica Acta, 8, 1963, 751-780.

[114] P.L. Taberna, P. Simon, J.F. Fauvarque, Electrochemical characteristics and impedance spectroscopy studies of carbon-carbon supercapacitors, Journal of the Electrochemical Society, 150, 2003, A292.

[115] Y. Yuan, L. Jiang, X. Li, P. Zuo, X. Zhang, Y. Lian, Y. Ma, M. Liang, Y. Zhao, L. Qu, Ultrafast shaped laser induced synthesis of MXene quantum dots/graphene for transparent supercapacitors, Advanced Materials, 34, 2022, 2110013.

[116] V. Šedajová, A. Bakandritsos, P. Błoński, M. Medveď, R. Langer, D. Zaoralová, J. Ugolotti, J. Dzíbelová, P. Jakubec, V. Kupka, M. Otyepka, Nitrogen doped graphene with diamond-like bonds achieves unprecedented energy density at high power in a symmetric sustainable supercapacitor, Energy & Environmental Science, 15, 2022, 740-748.

[117] B. Li, F. Dai, Q. Xiao, L. Yang, J. Shen, C. Zhang, M. Cai, Nitrogen-doped activated carbon for a high energy hybrid supercapacitor, Energy & Environmental Science, 9, 2016, 102-106.

[118] J. Yang, C. Yu, C. Hu, M. Wang, S. Li, H. Huang, K. Bustillo, X. Han, C. Zhao, W. Guo, Z. Zeng, H. Zheng, J. Qiu, Surface-confined fabrication of ultrathin nickel cobalt-layered double hydroxide nanosheets for high-performance supercapacitors, Advanced Functional Materials, 28, 2018, 1803272.

[119] S.J. Lee, J. Theerthagiri, P. Nithyadharseni, P. Arunachalam, D. Balaji, A. Madan Kumar, J. Madhavan, V. Mittal, M.Y. Choi, Heteroatom-doped graphene-based

materials for sustainable energy applications: A review, Renewable and Sustainable Energy Reviews, 143, 2021, 110849.

[120] P. Xie, W. Yuan, X.B. Liu, Y.M. Peng, Y.H. Yin, Y.S. Li, Z.P. Wu, Advanced carbon nanomaterials for state-of-the-art flexible supercapacitors, Energy Storage Materials, 36, 2021, 56-76.

[121] B. Wang, T. Ruan, Y. Chen, F. Jin, L. Peng, Y. Zhou, D. Wang, S. Dou, Graphene-based composites for electrochemical energy storage, Energy Storage Materials, 24, 2020, 22-51.

[122] Y. Wang, L. Zhang, H. Hou, W. Xu, G. Duan, S. He, K. Liu, S. Jiang, Recent progress in carbon-based materials for supercapacitor electrodes: A review, Journal of Materials Science, 56, 2021, 173-200.

[123] S. Roldán, C. Blanco, M. Granda, R. Menéndez, R. Santamaría, Towards a further generation of high-energy carbon-based capacitors by using redox-active electrolytes, Angewandte Chemie International Edition, 50, 2011, 1699-1701.

[124] K. Sun, E. Feng, H. Peng, G. Ma, Y. Wu, H. Wang, Z. Lei, A simple and high-performance supercapacitor based on nitrogen-doped porous carbon in redox-mediated sodium molybdate electrolyte, Electrochimica Acta, 158, 2015, 361-367.

[125] X. Tang, Y.H. Lui, B. Chen, S. Hu, Functionalized carbon nanotube based hybrid electrochemical capacitors using neutral bromide redox-active electrolyte for enhancing energy density, Journal of Power Sources, 352, 2017, 118-126.

[126] K. Jayaramulu, D.P. Dubal, B. Nagar, V. Ranc, O. Tomanec, M. Petr, K.K.R. Datta, R. Zboril, P. Gómez-Romero, R.A. Fischer, Ultrathin hierarchical porous carbon nanosheets for high-performance supercapacitors and redox electrolyte energy storage, Advanced Materials, 30, 2018, 1705789.

[127] J.Y. Hwang, M. Li, M.F. El-Kady, R.B. Kaner, Next-generation activated carbon supercapacitors: A simple step in electrode processing leads to remarkable gains in energy density, Advanced Functional Materials, 27, 2017, 1605745.

[128] S. Kumar, G. Saeed, L. Zhu, K.N. Hui, N.H. Kim, J.H. Lee, 0D to 3D carbon-based networks combined with pseudocapacitive electrode material for high energy density supercapacitor: A review, Chemical Engineering Journal, 403, 2021, 126352.

[129] M. Bigdeloo, E. Kowsari, A. Ehsani, A. Chinnappan, S. Ramakrishna, R. AliAkbari, Review on innovative sustainable nanomaterials to enhance the performance of supercapacitors, Journal of Energy Storage, 37, 2021, 102474.

[130] J. Yan, C.E. Ren, K. Maleski, C.B. Hatter, B. Anasori, P. Urbankowski, A. Sarycheva, Y. Gogotsi, Flexible MXene/graphene films for ultrafast supercapacitors with outstanding volumetric capacitance, Advanced Functional Materials, 27, 2017, 1701264.

[131] Z. Jian, Z. Xing, C. Bommier, Z. Li, X. Ji, Hard carbon microspheres: Potassium-ion anode versus sodium-ion anode, Advanced Energy Materials, 6, 2016, 1501874.

[132] L. Yao, Q. Wu, P. Zhang, J. Zhang, D. Wang, Y. Li, X. Ren, H. Mi, L. Deng, Z. Zheng, Scalable 2D hierarchical porous carbon nanosheets for flexible supercapacitors with ultrahigh energy density, Advanced Materials, 30, 2018, 1706054.

[133] A. Mahmood, S. Li, Z. Ali, H. Tabassum, B. Zhu, Z. Liang, W. Meng, W. Aftab, W. Guo, H. Zhang, M. Yousaf, S. Gao, R. Zou, Y. Zhao, Ultrafast sodium/potassium-ion intercalation into hierarchically porous thin carbon shells, Advanced Materials, 31, 2019, 1805430.

[134] J. Yin, W. Zhang, N.A. Alhebshi, N. Salah, H.N. Alshareef, Synthesis strategies of porous carbon for supercapacitor applications, Small Methods, 4, 2020, 1900853.

[135] H. Li, J. Li, A. Thomas, Y. Liao, Ultra-high surface area nitrogen-doped carbon aerogels derived from a schiff-base porous organic polymer aerogel for CO_2 storage and supercapacitors, Advanced Functional Materials, 29, 2019, 1904785.

[136] X.-W. Chen, J.-F. Gao, B. Hu, K. Li, L.-B. Kong, Template-induced self-activation route for hierarchical porous carbon derived from interpenetrating polymer networks as electrode material for supercapacitors, ChemElectroChem, 6, 2019, 2648-2658.

[137] H. Byeon, B. Gu, H.-J. Kim, J.H. Lee, I. Seo, J. Kim, J.W. Yang, J.-K. Kim, Redox chemistry of nitrogen-doped CNT-encapsulated nitroxide radical polymers for high energy density and rate-capability organic batteries, Chemical Engineering Journal, 413, 2021, 127402.

[138] X. Zhang, Z. Ju, L.M. Housel, L. Wang, Y. Zhu, G. Singh, N. Sadique, K.J. Takeuchi, E.S. Takeuchi, A.C. Marschilok, G. Yu, Promoting transport kinetics in Li-ion battery with aligned porous electrode architectures, Nano Letters, 19, 2019, 8255-8261.

[139] Y. Chen, L. Shi, Q. Yuan, A. Li, S. Huang, H.Y. Yang, X. Chen, J. Zhou, H. Song, Crystallization-induced morphological tuning toward denim-like graphene nanosheets in a KCl-copolymer solution, ACS Nano, 12, 2018, 4019-4024.

[140] C. Roland, G.H. Gilmer, Kinetics of nucleation-dominated step flow, Physical Review B, 54, 1996, 2931-2936.

[141] S. Deville, Freeze-casting of porous ceramics: A review of current achievements and issues, Advanced Engineering Materials, 10, 2008, 155-169.

[142] J.P. Perdew, K. Burke, M. Ernzerhof, Generalized gradient approximation made simple, Physical Review Letters, 77, 1996, 3865-3868.

[143] G. Kresse, J. Furthmüller, J. Hafner, Theory of the crystal structures of selenium and tellurium: The effect of generalized-gradient corrections to the local-density approximation, Physical Review B, 50, 1994, 13181-13185.

[144] G. Kresse, J. Furthmüller, Efficient iterative schemes for ab initio total-energy calculations using a plane-wave basis set, Physical Review B, 54, 1996, 11169-11186.

[145] G. Kresse, J. Furthmüller, Efficiency of ab-initio total energy calculations for metals and semiconductors using a plane-wave basis set, Computational Materials Science, 6, 1996, 15-50.

[146] S. Grimme, J. Antony, S. Ehrlich, H. Krieg, A consistent and accurate ab initio parametrization of density functional dispersion correction (DFT-d) for the 94 elements H-Pu, The Journal of Chemical Physics, 132, 2010, 154104.

[147] P. Wisesa, K.A. McGill, T. Mueller, Efficient generation of generalized monkhorst-pack grids through the use of informatics, Physical Review B, 93, 2016, 155109.

[148] K.-Y. Lin, M.T. Nguyen, K. Waki, J.-C. Jiang, Boron and nitrogen co-doped graphene used as counter electrode for iodine reduction in dye-sensitized solar cells, The Journal of Physical Chemistry C, 122, 2018, 26385-26392.

[149] Y. Zheng, Y. Wang, Y. Lu, Y.-S. Hu, J. Li, A high-performance sodium-ion battery enhanced by macadamia shell derived hard carbon anode, Nano Energy, 39, 2017, 489-498.

[150] M. Wang, J. Yang, S. Liu, C. Hu, S. Li, J. Qiu, Polyethyleneimine-mediated fabrication of two-dimensional cobalt sulfide/graphene hybrid nanosheets for high-performance supercapacitors, ACS Applied Materials & Interfaces, 11, 2019, 26235-26242.

[151] Z. Liu, K. Xiao, H. Guo, X. Ning, A. Hu, Q. Tang, B. Fan, Y. Zhu, X. Chen, Nitrogen-doped worm-like graphitized hierarchical porous carbon designed for

enhancing area-normalized capacitance of electrical double layer supercapacitors, Carbon, 117, 2017, 163-173.

[152] M. Wang, J. Yang, K. Jia, S. Liu, C. Hu, J. Qiu, Boosting supercapacitor performance of graphene by coupling with nitrogen-doped hollow carbon frameworks, Chemistry-A European Journal, 26, 2020, 2897-2903.

[153] A. Gopalakrishnan, S. Badhulika, Effect of self-doped heteroatoms on the performance of biomass-derived carbon for supercapacitor applications, Journal of Power Sources, 480, 2020, 228830.

[154] E. Frackowiak, K. Fic, M. Meller, G. Lota, Electrochemistry serving people and nature: High-energy ecocapacitors based on redox-active electrolytes, ChemSusChem, 5, 2012, 1181-1185.

[155] C.K. Kim, H. Zhou, T. Kowalewski, K. Matyjaszewski, H.K. Kim, Soft-templated tellurium-doped mesoporous carbon as a Pt-free electrocatalyst for high-performance dye-sensitized solar cells, ACS Applied Materials & Interfaces, 11, 2019, 2093-2102.

[156] Q. Tang, M. Zhong, H. Liu, X. Chen, Z. Zhang, S. Chen, Integrating effect of surface modification of microporous carbon by phosphorus/oxygen as well as the redox additive of *p*-aminophenol for high-performance supercapacitors, Advanced Materials Interfaces, 7, 2020, 1901933.

[157] K.V. Sankar, R. Kalai Selvan, Improved electrochemical performances of reduced graphene oxide based supercapacitor using redox additive electrolyte, Carbon, 90, 2015, 260-273.

[158] A.-Y. Wang, M. Chaudhary, T.-W. Lin, Enhancing the stability and capacitance of vanadium oxide nanoribbons/3D-graphene binder-free electrode by using $VoSO_4$ as redox-active electrolyte, Chemical Engineering Journal, 355, 2019, 830-839.

[159] D.D. Zhai, H. Liu, M. Wang, D. Wu, X.Y. Chen, Z.J. Zhang, Integrating surface functionalization and redox additives to improve surface reactivity for high performance supercapacitors, Electrochimica Acta, 323, 2019, 134810.

[160] Z.J. Zhang, G.L. Deng, X. Huang, X. Wang, J.M. Xue, X.Y. Chen, Highly boosting the supercapacitor performance by polydopamine-induced surface modification of carbon materials and use of hydroquinone as an electrolyte additive, Electrochimica Acta, 339, 2020, 135940.

[161] T. Xiong, W.S.V. Lee, L. Chen, T.L. Tan, X. Huang, J. Xue, Indole-based conjugated macromolecules as a redox-mediated electrolyte for an ultrahigh power supercapacitor, Energy & Environmental Science, 10, 2017, 2441-2449.

[162] S. Sundriyal, V. Shrivastav, M. Sharma, S. Mishra, A. Deep, Significantly enhanced performance of rGO/TiO_2 nanosheet composite electrodes based 1.8 V symmetrical supercapacitor with use of redox additive electrolyte, Journal of Alloys and Compounds, 790, 2019, 377-387.

[163] Y.F. Nie, Q. Wang, X.Y. Chen, Z.J. Zhang, Nitrogen and oxygen functionalized hollow carbon materials: The capacitive enhancement by simply incorporating novel redox additives into H_2SO_4 electrolyte, Journal of Power Sources, 320, 2016, 140-152.

[164] L.-Q. Mai, A. Minhas-Khan, X. Tian, K.M. Hercule, Y.-L. Zhao, X. Lin, X. Xu, Synergistic interaction between redox-active electrolyte and binder-free functionalized carbon for ultrahigh supercapacitor performance, Nature Communications, 4, 2013, 2923.

[165] S.-E. Chun, B. Evanko, X. Wang, D. Vonlanthen, X. Ji, G.D. Stucky, S.W. Boettcher, Design of aqueous redox-enhanced electrochemical capacitors with high specific energies and slow self-discharge, Nature Communications, 6, 2015, 7818.

[166] Y. Hou, D. Wang, X.H. Yang, W.Q. Fang, B. Zhang, H.F. Wang, G.Z. Lu, P. Hu, H.J. Zhao, H.G. Yang, Rational screening low-cost counter electrodes for dye-sensitized solar cells, Nature Communications, 4, 2013, 1583.

[167] V.D. Nithya, A review on holey graphene electrode for supercapacitor, Journal of Energy Storage, 44, 2021, 103380.

[168] T. Guo, D. Zhou, L. Pang, S. Sun, T. Zhou, J. Su, Perspectives on working voltage of aqueous supercapacitors, Small, 18, 2022, 2106360.

[169] J. Yin, W. Zhang, N.A. Alhebshi, N. Salah, H.N. Alshareef, Electrochemical zinc ion capacitors: Fundamentals, materials, and systems, Advanced Energy Materials, 11, 2021, 2100201.

[170] Y. Xu, W. Lu, G. Xu, T.-W. Chou, Structural supercapacitor composites: A review, Composites Science and Technology, 204, 2021, 108636.

[171] Y. Wang, X. Wu, Y. Han, T. Li, Flexible supercapacitor: Overview and outlooks, Journal of Energy Storage, 42, 2021, 103053.

[172] Y. Xu, S. Xiang, H. Mao, H. Zhou, G. Wang, H. Zhang, H. Zhao, Pseudocapacitive desalination via valence engineering with spindle-like manganese oxide/carbon composites, Nano Research, 14, 2021, 4878-4884.

[173] I. Rathinamala, I.M. Babu, J.J. William, G. Muralidharan, N. Prithivikumaran, Extra-durable hybrid supercapacitor based on cobalt sulfide and carbon (mwCNT) matrix electrodes, Journal of Energy Storage, 34, 2021, 102200.

[174] J. Chang, S. Zang, W. Liang, D. Wu, Z. Lian, F. Xu, K. Jiang, Z. Gao, Enhanced faradic activity by construction of p-n junction within reduced graphene oxide@cobalt nickel sulfide@nickle cobalt layered double hydroxide composite electrode for charge storage in hybrid supercapacitor, Journal of Colloid and Interface Science, 590, 2021, 114-124.

[175] C. Hu, L. Miao, Q. Yang, X. Yu, L. Song, Y. Zheng, C. Wang, L. Li, L. Zhu, X. Cao, H. Niu, Self-assembly of CNTs on Ni foam for enhanced performance of $NiCoO_2$@CNT@NF supercapacitor electrode, Chemical Engineering Journal, 410, 2021, 128317.

[176] S. Su, L. Sun, J. Qian, X. Shi, Y. Zhang, Hollow bimetallic phosphosulfide NiCo–P/S nanoparticles in a CNT/rGO framework with interface charge redistribution for battery-type supercapacitors, ACS Applied Energy Materials, 5, 2022, 685-696.

[177] B. Chen, L. Xu, Z. Xie, W.-Y. Wong, Supercapacitor electrodes based on metal-organic compounds from the first transition metal series, EcoMat, 3, 2021, e12106.

[178] R. Liu, A. Zhou, X. Zhang, J. Mu, H. Che, Y. Wang, T.-T. Wang, Z. Zhang, Z. Kou, Fundamentals, advances and challenges of transition metal compounds-based supercapacitors, Chemical Engineering Journal, 412, 2021, 128611.

[179] T. Wang, H.C. Chen, F. Yu, X.S. Zhao, H. Wang, Boosting the cycling stability of transition metal compounds-based supercapacitors, Energy Storage Materials, 16, 2019, 545-573.

[180] M.-Y. Chung, C.-T. Lo, High-performance binder-free RuO_2/electrospun carbon fiber for supercapacitor electrodes, Electrochimica Acta, 364, 2020, 137324.

[181] G. Li, R. Li, W. Zhou, A wire-shaped supercapacitor in micrometer size based on Fe_3O_4 nanosheet arrays on fe wire, Nano-Micro Letters, 9, 2017, 46.

[182] Y. Li, Z. Xu, D. Wang, J. Zhao, H. Zhang, Snowflake-like core-shell α-MnO_2@δ-MnO_2 for high performance asymmetric supercapacitor, Electrochimica Acta, 251, 2017, 344-354.

[183] P. Sivakumar, M.G. Jung, C.J. Raj, J. Park, H.S. Park, H. Jung, Nanowire architectured porous bimetallic transition metal oxides for high performance hybrid supercapacitor applications, International Journal of Energy Research, 45, 2021, 18091-18102.

[184] P.-Y. Lee, L.-Y. Lin, Synthesizing nickel-based transition bimetallic oxide via nickel precursor-free hydrothermal synthesis for battery supercapacitor hybrid devices, Journal of Colloid and Interface Science, 538, 2019, 297-307.

[185] T. Ma, M. Zhang, H. Liu, Y. Wang, Three-dimensional sulfur-doped graphene supported cobalt-molybdenum bimetallic sulfides nanocrystal with highly interfacial storage capability for supercapacitor electrodes, Electrochimica Acta, 322, 2019, 134762.

[186] R. Liu, S. Xu, X. Shao, Y. Wen, X. Shi, L. Huang, M. Hong, J. Hu, Z. Yang, Defect-engineered NiCo-S composite as a bifunctional electrode for high-performance supercapacitor and electrocatalysis, ACS Applied Materials & Interfaces, 13, 2021, 47717-47727.

[187] Z.-H. Huang, F.-F. Sun, Z.-Y. Yuan, W. Sun, B. Jia, H. Li, H. Li, T. Ma, An electro-activated bimetallic zinc-nickel hydroxide cathode for supercapacitor with super-long 140,000 cycle durability, Nano Energy, 82, 2021, 105727.

[188] Y. Chen, W.K. Pang, H. Bai, T. Zhou, Y. Liu, S. Li, Z. Guo, Enhanced structural stability of nickel–cobalt hydroxide via intrinsic pillar effect of metaborate for high-power and long-life supercapacitor electrodes, Nano Letters, 17, 2017, 429-436.

[189] P. Xu, K. Ye, D. Cao, J. Huang, T. Liu, K. Cheng, J. Yin, G. Wang, Facile synthesis of cobalt manganese oxides nanowires on nickel foam with superior electrochemical performance, Journal of Power Sources, 268, 2014, 204-211.

[190] H. Li, Z. Li, M. Sun, Z. Wu, W. Shen, Y.Q. Fu, Zinc cobalt sulfide nanoparticles as high performance electrode material for asymmetric supercapacitor, Electrochimica Acta, 319, 2019, 716-726.

[191] Y. Chen, C. Jing, X. Fu, M. Shen, K. Li, X. Liu, H.-C. Yao, Y. Zhang, K.X. Yao, Synthesis of porous NiCoS nanosheets with Al leaching on ordered mesoporous carbon for high-performance supercapacitors, Chemical Engineering Journal, 384, 2020, 123367.

[192] Y.-X. Zhan, P. Shi, R. Zhang, X.-Q. Zhang, X. Shen, C.-B. Jin, B.-Q. Li, J.-Q. Huang, Deciphering the effect of electrical conductivity of hosts on lithium

deposition in composite lithium metal anodes, Advanced Energy Materials, 11, 2021, 2101654.

[193] L.T. Gao, Z.-S. Guo, Effects of optimized electrode surface roughness and solid electrolyte interphase on lithium dendrite growth, Energy Technology, 9, 2021, 2000968.

[194] R. Chen, H. Ling, Q. Huang, Y. Yang, X. Wang, Interface engineering on cellulose-based flexible electrode enables high mass loading wearable supercapacitor with ultrahigh capacitance and energy density, Small, 18, 2022, 2106356.

[195] M. Liang, M. Zhao, H. Wang, J. Shen, X. Song, Enhanced cycling stability of hierarchical $NiCo_2S_4$@$Ni(OH)_2$@PPy core–shell nanotube arrays for aqueous asymmetric supercapacitors, Journal of Materials Chemistry A, 6, 2018, 2482-2493.

[196] D. Shi, M. Yang, B. Zhang, Z. Ai, H. Hu, Y. Shao, J. Shen, Y. Wu, X. Hao, Bcn-assisted built-in electric field in heterostructure: An innovative path for broadening the voltage window of aqueous supercapacitor, Advanced Functional Materials, 32, 2022, 2108843.

[197] S. Wang, S. Lv, G. Wang, K. Feng, S. Xie, G. Yuan, K. Nie, M. Sha, X. Sun, L. Zhang, Construction of novel bimetallic oxyphosphide as advanced anode for potassium ion hybrid capacitor, Advanced Science, 9, 2022, 2105193.

[198] C. Li, S. Dong, R. Tang, X. Ge, Z. Zhang, C. Wang, Y. Lu, L. Yin, Heteroatomic interface engineering in MOF-derived carbon heterostructures with built-in electric-field effects for high performance Al-ion batteries, Energy & Environmental Science, 11, 2018, 3201-3211.

[199] S.-H. Yi, Y.-C. Chan, C.-L. Mo, H.-C. Lin, M.-J. Chen, Enhancement of energy storage for electrostatic supercapacitors through built-in electric field engineering, Nano Energy, 2022, 107342.

[200] C. Sun, Y.-J. Wang, H. Gu, H. Fan, G. Yang, A. Ignaszak, X. Tang, D. Liu, J. Zhang, Interfacial coupled design of epitaxial graphene@SiC schottky junction with built-in electric field for high-performance anodes of lithium ion batteries, Nano Energy, 77, 2020, 105092.

[201] Y. Wang, Y. Ding, X. Guo, G. Yu, Conductive polymers for stretchable supercapacitors, Nano Research, 12, 2019, 1978-1987.

[202] G. Rebetez, O. Bardagot, J. Affolter, J. Réhault, N. Banerji, What drives the kinetics and doping level in the electrochemical reactions of PEDOT:PSS?, Advanced Functional Materials, 32, 2022, 2105821.

[203] Y. Su, X. Feng, R. Zheng, Y. Lv, Z. Wang, Y. Zhao, L. Shi, S. Yuan, Binary network of conductive elastic polymer constraining nanosilicon for a high-performance lithium-ion battery, ACS Nano, 15, 2021, 14570-14579.

[204] U. Lang, N. Naujoks, J. Dual, Mechanical characterization of PEDOT:PSS thin films, Synthetic Metals, 159, 2009, 473-479.

[205] Y. Jia, Y. Yuan, J. Sun, L. Dang, Z. Liu, Z. Lei, Porous pedot network coated on MoS_2 nanobelts toward improving capacitive performance, ACS Sustainable Chemistry & Engineering, 8, 2020, 12696-12705.

[206] M. Heydari Gharahcheshmeh, K.K. Gleason, Device fabrication based on oxidative chemical vapor deposition (oCVD) synthesis of conducting polymers and related conjugated organic materials, Advanced Materials Interfaces, 6, 2019, 1801564.

[207] L. Krieg, F. Meierhofer, S. Gorny, S. Leis, D. Splith, Z. Zhang, H. von Wenckstern, M. Grundmann, X. Wang, J. Hartmann, C. Margenfeld, I. Manglano Clavero, A. Avramescu, T. Schimpke, D. Scholz, H.-J. Lugauer, M. Strassburg, J. Jungclaus, S. Bornemann, H. Spende, A. Waag, K.K. Gleason, T. Voss, Toward three-dimensional hybrid inorganic/organic optoelectronics based on GAN/oCVD-PEDOT structures, Nature Communications, 11, 2020, 5092.

[208] M. Wang, X. Wang, P. Moni, A. Liu, D.H. Kim, W.J. Jo, H. Sojoudi, K.K. Gleason, CVD polymers for devices and device fabrication, Advanced Materials, 29, 2017, 1604606.

[209] X. Wang, X. Zhang, L. Sun, D. Lee, S. Lee, M. Wang, J. Zhao, Y. Shao-Horn, M. Dincă, T. Palacios, K. Gleason Karen, High electrical conductivity and carrier mobility in oCVD PEDOT thin films by engineered crystallization and acid treatment, Science Advances, 4, 2018, eaat5780.

[210] G.-L. Xu, Q. Liu, K.K.S. Lau, Y. Liu, X. Liu, H. Gao, X. Zhou, M. Zhuang, Y. Ren, J. Li, M. Shao, M. Ouyang, F. Pan, Z. Chen, K. Amine, G. Chen, Building ultraconformal protective layers on both secondary and primary particles of layered lithium transition metal oxide cathodes, Nature Energy, 4, 2019, 484-494.

[211] K. Xiang, J. Guo, J. Xu, T. Qu, Y. Zhang, S. Chen, P. Hao, M. Li, M. Xie, X. Guo, W. Ding, Surface sulfurization of NiCo-layered double hydroxide nanosheets

enable superior and durable oxygen evolution electrocatalysis, ACS Applied Energy Materials, 1, 2018, 4040-4049.

[212] R. Chen, M. Yu, R.P. Sahu, I.K. Puri, I. Zhitomirsky, The development of pseudocapacitor electrodes and devices with high active mass loading, Advanced Energy Materials, 10, 2020, 1903848.

[213] R.J. Gilliam, J.W. Graydon, D.W. Kirk, S.J. Thorpe, A review of specific conductivities of potassium hydroxide solutions for various concentrations and temperatures, International Journal of Hydrogen Energy, 32, 2007, 359-364.

[214] A.V. Volkov, K. Wijeratne, E. Mitraka, U. Ail, D. Zhao, K. Tybrandt, J.W. Andreasen, M. Berggren, X. Crispin, I.V. Zozoulenko, Understanding the capacitance of PEDOT:PSS, Advanced Functional Materials, 27, 2017, 1700329.

[215] M. Modarresi, J.F. Franco-Gonzalez, I. Zozoulenko, Morphology and ion diffusion in PEDOT:TOS. A coarse grained molecular dynamics simulation, Physical Chemistry Chemical Physics, 20, 2018, 17188-17198.

[216] G. Kresse, J. Hafner, Ab initio molecular-dynamics simulation of the liquid-metal-amorphous-semiconductor transition in germanium, Physical Review B, 49, 1994, 14251-14269.

[217] P. Fuentealba, E. Chamorro, J.C. Santos, Understanding and using the electron localization function, Theoretical and computational chemistry, 19, 2007, 57-85.

[218] H. Liang, J. Lin, H. Jia, S. Chen, J. Qi, J. Cao, T. Lin, W. Fei, J. Feng, Hierarchical NiCo-LDH/NiCoP@NiMn-LDH hybrid electrodes on carbon cloth for excellent supercapacitors, Journal of Materials Chemistry A, 6, 2018, 15040-15046.

[219] M. Horikawa, T. Fujiki, T. Shirosaki, N. Ryu, H. Sakurai, S. Nagaoka, H. Ihara, The development of a highly conductive PEDOT system by doping with partially crystalline sulfated cellulose and its electric conductivity, Journal of Materials Chemistry C, 3, 2015, 8881-8887.

[220] M. Wang, J. Yang, S. Liu, C. Hu, J. Qiu, Dual hybrid effect endowing nickel–cobalt sulfides with enhanced cycling stability for asymmetrical supercapacitors, ACS Applied Energy Materials, 3, 2020, 6977-6984.

[221] C. Luo, E. Hu, J. Gaskell Karen, X. Fan, T. Gao, C. Cui, S. Ghose, X.-Q. Yang, C. Wang, A chemically stabilized sulfur cathode for lean electrolyte lithium sulfur batteries, Proceedings of the National Academy of Sciences, 117, 2020, 14712-14720.

[222] H. Chen, L. Hu, M. Chen, Y. Yan, L. Wu, Nickel–cobalt layered double hydroxide nanosheets for high-performance supercapacitor electrode materials, Advanced Functional Materials, 24, 2014, 934-942.

[223] H. Liu, J. Zhu, Z. Li, Z. Shi, J. Zhu, H. Mei, Fe_2O_3/N doped Rgo anode hybridized with NiCo LDH/$Co(OH)_2$ cathode for battery-like supercapacitor, Chemical Engineering Journal, 403, 2021, 126325.

[224] M. Gao, Y. Li, J. Yang, Y. Liu, Y. Liu, X. Zhang, S. Wu, K. Cai, Nickel-cobalt (O_{xy})hydroxide battery-type supercapacitor electrode with high mass loading, Chemical Engineering Journal, 429, 2022, 132423.

[225] M.S. Vidhya, R. Yuvakkumar, G. Ravi, B. Saravanakumar, D. Velauthapillai, Asymmetric polyhedron structured $NiSe_2$@$MoSe_2$ device for use as a supercapacitor, Nanoscale Advances, 3, 2021, 4207-4215.

[226] W.G. Pell, B.E. Conway, Analysis of power limitations at porous supercapacitor electrodes under cyclic voltammetry modulation and DC charge, Journal of Power Sources, 96, 2001, 57-67.

[227] R.J. Klingler, J.K. Kochi, Electron-transfer kinetics from cyclic voltammetry. Quantitative description of electrochemical reversibility, The Journal of Physical Chemistry, 85, 1981, 1731-1741.

[228] T. Wang, S. Zhang, X. Yan, M. Lyu, L. Wang, J. Bell, H. Wang, 2-methylimidazole-derived Ni–Co layered double hydroxide nanosheets as high rate capability and high energy density storage material in hybrid supercapacitors, ACS Applied Materials & Interfaces, 9, 2017, 15510-15524.

[229] X. Wang, C. Jing, W. Zhang, X. Wang, X. Liu, B. Dong, Y. Zhang, One-step phosphorization synthesis of CoP@NiCoP nanowire/nanosheet composites hybrid arrays on Ni foam for high-performance supercapacitors, Applied Surface Science, 532, 2020, 147437.

[230] X. Gao, L. Yin, L. Zhang, Y. Zhao, B. Zhang, Decoration of NiCoP nanowires with interlayer-expanded few-layer $MoSe_2$ nanosheets: A novel electrode material for asymmetric supercapacitors, Chemical Engineering Journal, 395, 2020, 125058.

[231] Y. Liu, X. Cao, L. Cui, Y. Zhong, R. Zheng, D. Wei, C. Barrow, J.M. Razal, W. Yang, J. Liu, Zn-Ni-Co trimetallic carbonate hydroxide nanothorns branched on $Cu(OH)_2$ nanorods array based on Cu foam for high-performance asymmetric supercapacitors, Journal of Power Sources, 437, 2019, 226897.

[232] X. Tang, Y.H. Lui, B. Zhang, S. Hu, Venus flytrap-like hierarchical NiCoMn–O@$NiMoO_4$@C nanosheet arrays as free-standing core-shell electrode material for hybrid supercapacitor with high electrochemical performance, Journal of Power Sources, 477, 2020, 228977.

[233] Y. Shao, Y. Zhao, H. Li, C. Xu, Three-dimensional hierarchical $Ni_xCo_{1-x}O/Ni_yCo_{2-y}P$@C hybrids on nickel foam for excellent supercapacitors, ACS Applied Materials & Interfaces, 8, 2016, 35368-35376.

[234] Z. Xu, C. Du, H. Yang, J. Huang, X. Zhang, J. Chen, NiCoP@CoS tree-like core-shell nanoarrays on nickel foam as battery-type electrodes for supercapacitors, Chemical Engineering Journal, 421, 2021, 127871.

[235] J. Ding, W. Hu, E. Paek, D. Mitlin, Review of hybrid ion capacitors: From aqueous to lithium to sodium, Chemical Reviews, 118, 2018, 6457-6498.

[236] P. Cai, K. Zou, X. Deng, B. Wang, M. Zheng, L. Li, H. Hou, G. Zou, X. Ji, Comprehensive understanding of sodium-ion capacitors: Definition, mechanisms, configurations, materials, key technologies, and future developments, Advanced Energy Materials, 11, 2021, 2003804.

[237] F. Li, Z. Zhou, Micro/nanostructured materials for sodium ion batteries and capacitors, Small, 14, 2018, 1702961.

[238] J. Wang, P. Nie, B. Ding, S. Dong, X. Hao, H. Dou, X. Zhang, Biomass derived carbon for energy storage devices, Journal of Materials Chemistry A, 5, 2017, 2411-2428.

[239] F. Bu, M.M. Zagho, Y. Ibrahim, B. Ma, A. Elzatahry, D. Zhao, Porous MXenes: Synthesis, structures, and applications, Nano Today, 30, 2020, 100803.

[240] Z. Xu, M. Wu, Z. Chen, C. Chen, J. Yang, T. Feng, E. Paek, D. Mitlin, Direct structure–performance comparison of all-carbon potassium and sodium ion capacitors, Advanced Science, 6, 2019, 1802272.

[241] S. Chen, J. Wang, L. Fan, R. Ma, E. Zhang, Q. Liu, B. Lu, An ultrafast rechargeable hybrid sodium-based dual-ion capacitor based on hard carbon cathodes, Advanced Energy Materials, 8, 2018, 1800140.

[242] H. Huang, D. Kundu, R. Yan, E. Tervoort, X. Chen, L. Pan, M. Oschatz, M. Antonietti, M. Niederberger, Fast na-ion intercalation in zinc vanadate for high-performance Na-ion hybrid capacitor, Advanced Energy Materials, 8, 2018, 1802800.

[243] Y. Wu, R.R. Gaddam, C. Zhang, H. Lu, C. Wang, D. Golberg, X.S. Zhao, Stabilising cobalt sulphide nanocapsules with nitrogen-doped carbon for high-performance sodium-ion storage, Nano-Micro Letters, 12, 2020, 48.

[244] S.-W. Kim, D.-H. Seo, X. Ma, G. Ceder, K. Kang, Electrode materials for rechargeable sodium-ion batteries: Potential alternatives to current lithium-ion batteries, Advanced Energy Materials, 2, 2012, 710-721.

[245] M. Wahid, D. Puthusseri, Y. Gawli, N. Sharma, S. Ogale, Hard carbons for sodium-ion battery anodes: Synthetic strategies, material properties, and storage mechanisms, ChemSusChem, 11, 2018, 506-526.

[246] L. Xiao, H. Lu, Y. Fang, M.L. Sushko, Y. Cao, X. Ai, H. Yang, J. Liu, Low-defect and low-porosity hard carbon with high coulombic efficiency and high capacity for practical sodium ion battery anode, Advanced Energy Materials, 8, 2018, 1703238.

[247] I. Escher, G. A. Ferrero, M. Goktas, P. Adelhelm, In-situ (operando) electrochemical dilatometry as a method to distinguish charge storage mechanisms and metal plating processes for sodium and lithium ions in hard carbon battery electrodes, Advanced Materials Interfaces, 9, 2022, 2100596.

[248] X. Li, L. Zhao, P. Li, Q. Zhang, M.-S. Wang, In-situ electron microscopy observation of electrochemical sodium plating and stripping dynamics on carbon nanofiber current collectors, Nano Energy, 42, 2017, 122-128.

[249] L. Zhang, X. Zhu, G. Wang, G. Xu, M. Wu, H.-K. Liu, S.-X. Dou, C. Wu, Bi nanoparticles embedded in 2D carbon nanosheets as an interfacial layer for advanced sodium metal anodes, Small, 17, 2021, 2007578.

[250] C. Bommier, X. Ji, P.A. Greaney, Electrochemical properties and theoretical capacity for sodium storage in hard carbon: Insights from first principles calculations, Chemistry of Materials, 31, 2019, 658-677.

[251] H. Hou, C.E. Banks, M. Jing, Y. Zhang, X. Ji, Carbon quantum dots and their derivative 3D porous carbon frameworks for sodium-ion batteries with ultralong cycle life, Advanced Materials, 27, 2015, 7861-7866.

[252] Q. Zhang, Y. Zeng, C. Ling, L. Wang, Z. Wang, T.-E. Fan, H. Wang, J. Xiao, X. Li, B. Qu, Boosting fast sodium ion storage by synergistic effect of heterointerface engineering and nitrogen doping porous carbon nanofibers, Small, 18, 2022, 2107514.

[253] X. Miao, D. Sun, X. Zhou, Z. Lei, Designed formation of nitrogen and sulfur dual-doped hierarchically porous carbon for long-life lithium and sodium ion batteries, Chemical Engineering Journal, 364, 2019, 208-216.

[254] Y. Tao, Z.-Y. Sui, B.-H. Han, Advanced porous graphene materials: From in-plane pore generation to energy storage applications, Journal of Materials Chemistry A, 8, 2020, 6125-6143.

[255] W. Chen, M. Wan, Q. Liu, X. Xiong, F. Yu, Y. Huang, Heteroatom-doped carbon materials: Synthesis, mechanism, and application for sodium-ion batteries, Small Methods, 3, 2019, 1800323.

[256] Y. Yuan, Z. Chen, H. Yu, X. Zhang, T. Liu, M. Xia, R. Zheng, M. Shui, J. Shu, Heteroatom-doped carbon-based materials for lithium and sodium ion batteries, Energy Storage Materials, 32, 2020, 65-90.

[257] H.-J. Liang, Z.-Y. Gu, X.-X. Zhao, J.-Z. Guo, J.-L. Yang, W.-H. Li, B. Li, Z.-M. Liu, W.-L. Li, X.-L. Wu, Ether-based electrolyte chemistry towards high-voltage and long-life Na-ion full batteries, Angewandte Chemie International Edition, 60, 2021, 26837-26846.

[258] H. Wang, Y. Shao, S. Mei, Y. Lu, M. Zhang, J.-k. Sun, K. Matyjaszewski, M. Antonietti, J. Yuan, Polymer-derived heteroatom-doped porous carbon materials, Chemical Reviews, 120, 2020, 9363-9419.

[259] X. Zhu, C. Hu, R. Amal, L. Dai, X. Lu, Heteroatom-doped carbon catalysts for zinc–air batteries: Progress, mechanism, and opportunities, Energy & Environmental Science, 13, 2020, 4536-4563.

[260] C. Chen, Y. Huang, Z. Meng, M. Lu, Z. Xu, P. Liu, T. Li, N/O/P-rich three-dimensional carbon network for fast sodium storage, Carbon, 170, 2020, 225-235.

[261] W. Xu, C. Lv, Y. Zou, J. Ren, X. She, Y. Zhu, Y. Zhang, S. Chen, X. Yang, T. Zhan, J. Sun, D. Yang, Mechanistic insight into high-efficiency sodium storage based on N/O/P-functionalized ultrathin carbon nanosheet, Journal of Power Sources, 442, 2019, 227184.

[262] B. Yin, S. Liang, D. Yu, B. Cheng, I.L. Egun, J. Lin, X. Xie, H. Shao, H. He, A. Pan, Increasing accessible subsurface to improving rate capability and cycling stability of sodium-ion batteries, Advanced Materials, 33, 2021, 2100808.

[263] J. Yan, H. Li, K. Wang, Q. Jin, C. Lai, R. Wang, S. Cao, J. Han, Z. Zhang, J. Su, K. Jiang, Ultrahigh phosphorus doping of carbon for high-rate sodium ion batteries anode, Advanced Energy Materials, 11, 2021, 2003911.

[264] Y. Li, M. Chen, B. Liu, Y. Zhang, X. Liang, X. Xia, Heteroatom doping: An effective way to boost sodium ion storage, Advanced Energy Materials, 10, 2020, 2000927.

[265] A.K. Thakur, K. Kurtyka, M. Majumder, X. Yang, H.Q. Ta, A. Bachmatiuk, L. Liu, B. Trzebicka, M.H. Rummeli, Recent advances in boron- and nitrogen-doped carbon-based materials and their various applications, Advanced Materials Interfaces, 9, 2022, 2101964.

[266] W. Abdelwahed, G. Degobert, S. Stainmesse, H. Fessi, Freeze-drying of nanoparticles: Formulation, process and storage considerations, Advanced Drug Delivery Reviews, 58, 2006, 1688-1713.

[267] W. Yang, W. Yang, L. Kong, A. Song, X. Qin, Synthesis of three-dimensional hierarchical porous carbon for high-performance supercapacitors, Ionics, 24, 2018, 3133-3141.

[268] N. Kucuk, K. Bulcar, T. Dogan, J. Garcia Guinea, Z.G. Portakal, Y. Karabulut, M. Ayvacikli, A. Canimoglu, M. Topaksu, N. Can, Doping Sm^{3+} into ZnB_2O_4 phosphors and their structural and cathodoluminescence properties, Journal of Alloys and Compounds, 748, 2018, 245-251.

[269] X.-Y. Liu, M. Huang, H.-L. Ma, Z.-Q. Zhang, J.-M. Gao, Y.-L. Zhu, X.-J. Han, X.-Y. Guo, Preparation of a carbon-based solid acid catalyst by sulfonating activated carbon in a chemical reduction process, Molecules, 15, 2010, 7188-7196.

[270] H. Liu, T. Xu, C. Cai, K. Liu, W. Liu, M. Zhang, H. Du, C. Si, K. Zhang, Multifunctional superelastic, superhydrophilic, and ultralight nanocellulose-based composite carbon aerogels for compressive supercapacitor and strain sensor, Advanced Functional Materials, 32, 2022, 2113082.

[271] N. Mubarak, F. Rehman, M. Ihsan-Ul-Haq, M. Xu, Y. Li, Y. Zhao, Z. Luo, B. Huang, J.-K. Kim, Highly sodiophilic, defect-rich, lignin-derived skeletal carbon nanofiber host for sodium metal batteries, Advanced Energy Materials, 12, 2022, 2103904.

[272] S. Wang, Y. Chen, Y. Jie, S. Lang, J. Song, Z. Lei, S. Wang, X. Ren, D. Wang, X. Li, R. Cao, G. Zhang, S. Jiao, Stable sodium metal batteries via manipulation of electrolyte solvation structure, Small Methods, 4, 2020, 1900856.

[273] F. Ambroz, T.J. Macdonald, V. Martis, I.P. Parkin, Evaluation of the BET theory for the characterization of MESO and microporous MOFs, Small Methods, 2, 2018, 1800173.

[274] C.-T. Hsieh, H. Teng, Influence of mesopore volume and adsorbate size on adsorption capacities of activated carbons in aqueous solutions, Carbon, 38, 2000, 863-869.

[275] Y. Li, F. Wu, Y. Li, M. Liu, X. Feng, Y. Bai, C. Wu, Ether-based electrolytes for sodium ion batteries, Chemical Society Reviews, 51, 2022, 4484-4536.

[276] I. Elizabeth, B.P. Singh, S. Trikha, S. Gopukumar, Bio-derived hierarchically macro-meso-micro porous carbon anode for lithium/sodium ion batteries, Journal of Power Sources, 329, 2016, 412-421.

[277] H. Hou, L. Shao, Y. Zhang, G. Zou, J. Chen, X. Ji, Large-area carbon nanosheets doped with phosphorus: A high-performance anode material for sodium-ion batteries, Advanced Science, 4, 2017, 1600243.

[278] R. Fei, H. Wang, Q. Wang, R. Qiu, S. Tang, R. Wang, B. He, Y. Gong, H.J. Fan, In situ hard-template synthesis of hollow bowl-like carbon: A potential versatile platform for sodium and zinc ion capacitors, Advanced Energy Materials, 10, 2020, 2002741.

[279] C. Wang, J. Yan, T. Li, Z. Lv, X. Hou, Y. Tang, H. Zhang, Q. Zheng, X. Li, A coral-like FeP@NC anode with increasing cycle capacity for sodium-ion and lithium-ion batteries induced by particle refinement, Angewandte Chemie International Edition, 60, 2021, 25013-25019.

[280] K. Xu, Y. Li, J. Xiong, X. Ou, W. Su, G. Zhong, C. Yang, Activated amorphous carbon with high-porosity derived from camellia pollen grains as anode materials for lithium/sodium ion batteries, 6, 2018, 366.

[281] J. Ruan, F. Mo, Z. Chen, M. Liu, S. Zheng, R. Wu, F. Fang, Y. Song, D. Sun, Rational construction of nitrogen-doped hierarchical dual-carbon for advanced potassium-ion hybrid capacitors, Advanced Energy Materials, 10, 2020, 1904045.

[282] H. Huang, R. Xu, Y. Feng, S. Zeng, Y. Jiang, H. Wang, W. Luo, Y. Yu, Sodium/potassium-ion batteries: Boosting the rate capability and cycle life by combining morphology, defect and structure engineering, Advanced Materials, 32, 2020, 1904320.

[283] A. Chojnacka, X. Pan, P. Jeżowski, F. Béguin, High performance hybrid sodium-ion capacitor with tin phosphide used as battery-type negative electrode, Energy Storage Materials, 22, 2019, 200-206.

[284] Q. Zhao, D. Yang, A.K. Whittaker, X.S. Zhao, A hybrid sodium-ion capacitor with polyimide as anode and polyimide-derived carbon as cathode, Journal of Power Sources, 396, 2018, 12-18.

[285] Z. Chen, W. Li, J. Yang, J. Liao, C. Chen, Y. Song, S.A. Ali Shah, Z. Xu, M. Wu, Excellent electrochemical performance of potassium ion capacitor achieved by a high nitrogen doped activated carbon, Journal of the Electrochemical Society, 167, 2020, 050506.

[286] C. Yang, M. Zhang, N. Kong, J. Lan, Y. Yu, X. Yang, Self-supported carbon nanofiber films with high-level nitrogen and phosphorus co-doping for advanced lithium-ion and sodium-ion capacitors, ACS Sustainable Chemistry & Engineering, 7, 2019, 9291-9300.

[287] K. Lu, B. Song, X. Gao, H. Dai, J. Zhang, H. Ma, High-energy cobalt hexacyanoferrate and carbon micro-spheres aqueous sodium-ion capacitors, Journal of Power Sources, 303, 2016, 347-353.